Technische Universität München
Physik Department E16

Optical and Electrical Characterization of InGaAsN used for 1.3 µm lasers

Gheorghe Dumitras

Vollständiger Abdruck der von der Fakultät für Physik der Technischen Universität München zur Erlangung des akademischen Grades eines Doktors der Naturwissenschaften genehmigten Dissertation.

Vorsitzender:	Univ.-Prof. Dr. M. Kleber
Prüfer der Dissertation:	
	1. Univ.-Prof. F. Koch, Ph.D.
	2. Univ.-Prof. Dr. M.-Chr. Amann

Die Dissertation wurde am 15.07.2003 bei der Technischen Universität München eingereicht und durch die Fakultät für Physik am 31.07.2003 angenommen.

I think I can safely say that nobody understands
Quantum Mechanics.
Nobody knows how it can be like that.

Richard P. Feynman

Părinților mei

angefertigt August 1999 - April 2003

am Physik Department E16 (Prof. F. Koch, Ph.D.)

Technische Universität München

Garching bei München, Deutschland

Table of Content

Chapter 1
Introduction

The motivation of this work is the achievement of laser emission at 1.3 μm from InGaAsN quantum well (QW) lasers. More specifically, the objective was to reach 1.3 μm laser emission from Vertical Cavity Surface Emitting Lasers (VCSEL). This work was done in parallel with the development of Molecular Beam Epitaxy (MBE), GaAs-based technology at Infineon Technologies AG in order to reach this objective, it is an important part of the related research activity, and has as purpose the electro-optical characterization of MBE-grown (In)GaAsN material.

For the transmission of information, electromagnetic-radiation propagation through a medium is used. With the development of the telecommunication infrastructure, the need for high data transmission rates has increased. To reach higher data transmission rates, the frequency of the electromagnetic radiation must correspondingly increase. As a consequence, the propagation medium has evolved from cable and radio-channels to optical fiber. Nowadays, data transmission rates of tens of Gbit/sec through optical fibers are usual. For data transmission through optical fibers, two parameters are important: the light attenuation and dispersion. The first parameter influences the distance over which communication is possible, the second parameter influences directly the data transmission rate. Light transmission through optical *glass* fibers - which are cheap - is possible around three wavelengths, where the light attenuation is small: 850 nm, 1.3 μm and 1.55 μm. Concerning the light dispersion (the variation of the speed of light with the wavelength, which influences the broadening in time of a light pulse), it has a minimum around 1.3 μm; to reach indeed high transmission rates, the spectrum of the light must be as narrow as possible, which is possible only by using lasers. The VCSEL laser design has the advantage of an easier integration, which opens the possibility of having laser *arrays* integrated on a single chip. From a commercial point of view, the available GaAs technology for opto-electronic devices should be used in order to obtain cost reduction.

The laser technology has also developed in time. At the beginning a bulk homo-junction was used. Now, quantum well lasers are normally used, which have far superior characteristics. There is also an important research activity to develop the quantum-dot (QD) lasers, which theoretically have even better characteristics than QW-lasers.

During the period of time in which this work took place, the realization of InGaAsN QW-based 1.3 μm edge emitting and Vertical Cavity Surface Emission Laser (VCSEL) was achieved at Infineon Technologies AG. Current threshold of 2.2 mA (corresponding to 3 kA/cm^2) and output power of 1 mW at 1306 nm was achieved, at room temperature[1]. This work is concerned mostly with the study of laser material, i.e. InGaAsN quantum wells emitting around 1.3 μm.

At the beginning of this chapter, it is firstly explained what advantages the InGaAsN semiconductor alloy brings for 1.3 µm lasers. Then general considerations about the MBE and details about the growth of the (In)GaAsN are presented. It follows the discussion of important theoretical and technological issues about (In)GaAsN material. Finally, the structure of the work is introduced.

1.1. Why nitrogen?

Heterostructures based on the quaternary InGaAsN alloy with low N concentrations (up to 4%) came recently[2] into consideration due to the negative band gap variation, i.e. the reduction of the band gap with addition of nitrogen. There is both a commercial and fundamental interest in the N-containing III-V semiconductor alloys GaAsN and InGaAsN. The commercial interest resides in the prospects of using the InGaAsN material in opto-electronic devices (1.3 µm infrared lasers for telecommunication applications) by using the available GaAs technology. Up to now, the quaternary material InGaAsP was used for 1.3 µm lasers. It is expected that the InGaAsN material brings advantages over the InGaAsP, due to more favorable band offsets and consequently better laser operation characteristics[3]. Essential for the use of any material in opto-electronic devices are two conditions: (a) the usefulness of their opto-electronic properties, and (b) the availability and simplicity of a technology. In the case of InGaAsN material, the technology is up to now still not fully mature. But once the technological problems have been solved, InGaAsN offers a few advantages over other materials (see Fig. 1.1) for quantum well lasers:

- GaAs/InGaAsN/GaAs quantum wells (QWs) are of type I, with favorable band offsets for the near IR semiconductor lasers;

- the band-gap can in principle be reduced beyond 1.5 µm, because both the addition of In and N reduce the band gap *and* the strain induced by In and N has a different sign (band gap engineering): thus strain compensation can be achieved;

- the possibility of obtaining 1.3 µm quantum well VCSELs grown on GaAs substrates, and so using the available GaAs technology.

In Fig. 1.1 the band gap as function of lattice constant is represented for a few common semiconductor alloys. Sakai *et al.* first predicted this evolution of the band gap of GaAsN[4]. One can see that: (a) the band gap of the GaAsN alloy reduces strongly for small N content and can become even zero, and (b) the InGaAsN material can be grown, for suitable N and In content, to have a band gap smaller than 1 eV (corresponding to 1.3 µm laser emission) *and* lattice-matched to GaAs. This evolution of the GaAsN band gap with the N-content was theoretically however not fully confirmed: for a random GaAsN alloy, the band gap is always positive[5]. On the contrary, for lattice matched InGaAsN the band gap can reach the value zero, according to calculations[16].

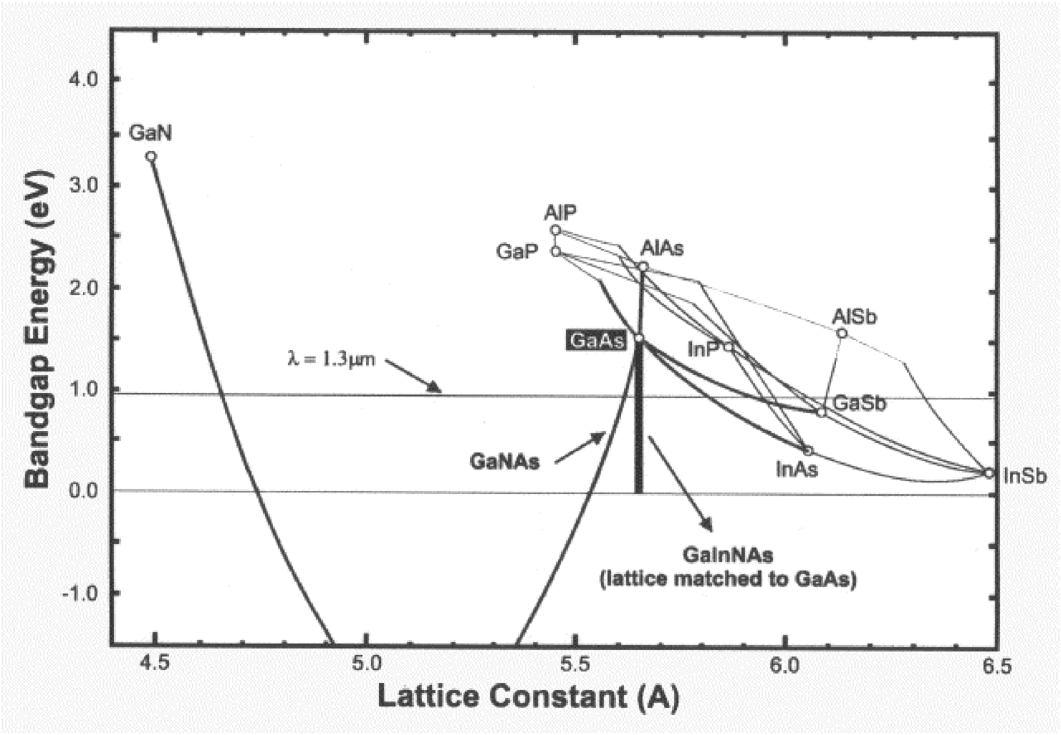

Fig. 1.1: Band gap vs. lattice constant representation of common ternary III-V alloys (from reference [3]).

One essential feature of a semiconductor quantum well (QW) laser is the threshold current, the minimum current value at which the stimulated emission regime of the laser sets in. This has an exponential increase with the temperature, given by the empirical relation[6]:

$$J_{th} = J_{th0} \cdot e^{\frac{T}{T_0}} \qquad (1.1)$$

J_{th} at room temperature is a direct measure of the laser quality: the smaller it is, the better the laser quality. Ideally, the characteristic temperature T_0 must be large and J_{th0} small. J_{th0} depends on the active-zone (QW) material quality as well as on laser design (quality of mirrors, carrier collection efficiency, contact quality, and so on)[3]. T_0 depends strongly on the band offsets between the quantum well and barrier materials[3]. It is usually smaller for narrow band gap materials, due to increased Auger non-radiative recombination in such materials. The increase in threshold current with temperature can be understood as follows:

- there is one intrinsic component, accounting for the increasing spread in the energy of carriers in the conduction and valence bands;
- the other increase in the threshold current with temperature is due to the loss of injected carriers: either by non-radiative recombination (Auger, important in small

band gap materials) or by carrier leakage from the active region. Using materials with larger band offsets or with an ideal band offset ratio can reduce this last term.

1.2. Molecular Beam Epitaxy growth of (In)GaAsN

Molecular beam epitaxy (MBE) is a common method to grow InGaAsN and GaAsN alloys. The MBE machine works under ultra high vacuum (UHV) conditions. The principle of MBE is shortly described: the substrate is "irradiated" with molecular beams of the alloy constituents, obtained by heating very pure chemical elements in special containers, called effusion cells. The substrate is heated (at a temperature called growth temperature) and rotated (a few times per minute) in a high vacuum (10^{-6} mbar during growth) during the growth process. The growth chamber walls are cooled down to liquid nitrogen temperature (77 K) and act like a trap for the "lost" atoms, atoms that do not stick to the substrate. The fluxes for each element can be varied by varying the corresponding cell temperature and/or by valves attached to the cells. Each cell has a shutter that can stop the corresponding element from reaching the substrate. A very important parameter of the growth process is the growth temperature as seen further. A MBE machine contains also in-situ control equipment (Reflection High-Energy Electron Diffraction), sample-manipulating facilities, flux measurement devices and so on. A description of the MBE system can be found in reference [7].

The thermodynamics and kinetics of the growth process is a complex one and is still not fully understood for ternary and quaternary semiconductor alloys. Up to now the growth process cannot be fully computer-simulated due to its complexity, which increases with increasing growth temperature: only small parts of the growth mechanism have been understood. The growth process takes place in conditions far from equilibrium: the molecular or atomic elements coming from the cells and hitting the growing surface undergo random walk, diffusion and desorption, before finding a place in the crystal lattice; the atoms which are not incorporated in the lattice (due to desorption) are finally caught by the cryo-shield around the growth chamber. The growth process depends on the growth temperature, the fluxes of each element, and on the previous growth history by means of the surface morphology.

In the rest of this paragraph, the peculiarities of the MBE growth of (In)GaAsN are discussed. To grow (In)GaAsN, the molecular nitrogen (N_2) must first be dissociated to atomic nitrogen. To dissociate the molecules, the molecular nitrogen is heated to reach a plasma temperature. The N-cell used in our system is a RF-coupled plasma source. The RF power can be varied between 200 and 500 W. The gas inlet is pressure-controlled.

The probability for an atom which falls on the growing surface to be integrated in the crystal lattice is called *sticking coefficient*. For nitrogen the sticking coefficient is about 1 at temperatures below 520°C and decreases at temperatures over 520°C[10]. The growth temperature of the GaAsN is between 420 and 520°C. At (quantum well) compositions necessary for emission at 1.3 µm, the InGaAsN material is predicted to be intrinsically unstable during growth due to the interaction between the constituents of the alloy (InGaAsN has a large miscibility gap[8]). Consequently, the growth temperature for InGaAsN must be around 420°C; otherwise the alloy grows nonhomogeneously (three-dimensional growth, phase separation, spinoidal decomposition of the alloy)[8, 9]. This has the following consequences:

- the MBE machine must be very clean (high-purity alloy constituents) in order to obtain high-quality samples, because at low growth temperatures impurities are more easily incorporated in the grown material;

- the crystal quality of the material grown at such a low temperature may be inferior. This can and must be recovered through thermal annealing: the samples are typically heated at about 720°C for 10 - 30 minutes in order to recover the crystal quality. The influence of the annealing process on the InGaAsN samples is discussed in detail in Chapters 3 and 5;

More details about the MBE growth of (In)GaAsN can be found in reference [10] and in Chapter 2, where the structure of the sample is discussed.

In conclusion, as a result of growth conditions and InGaAsN material instability, the quality of the as-grown material is not optimal. These technological problems often obscure the physics in the studied samples.

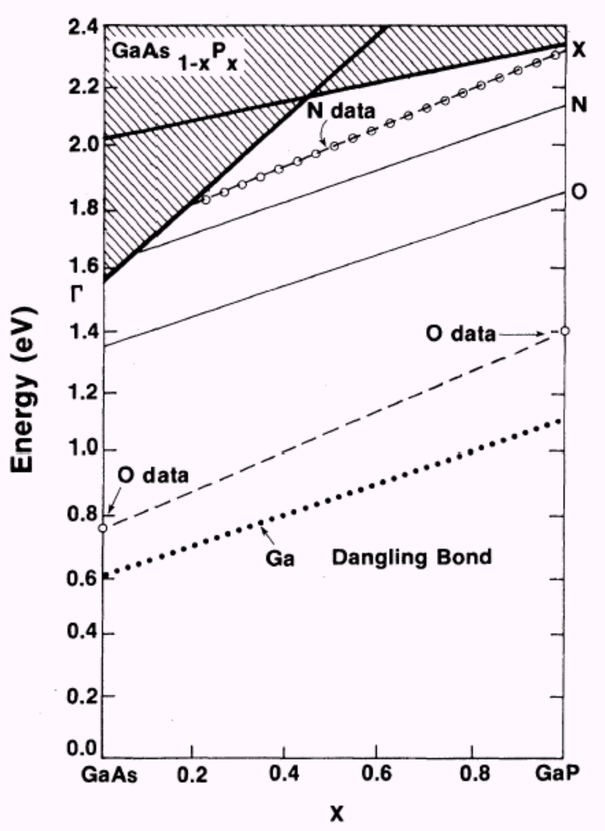

Fig. 1.2: The energy position relative to the valence band maximum of N-levels as impurity in $GaAs_{1-x}P_x$ alloy (from reference [11]). For GaAs the N-levels lie inside the conduction band.

1.3. The doping-alloy transition. The band structure of the GaAsN and InGaAsN alloys

To have a first understanding about the properties of N incorporated in GaAs, it is perhaps best to start with a very low N concentration (doping limit) and to increase it gradually up to usual N-alloy concentrations. The case of N as an impurity has been discussed over 20 years ago in a paper by Hjalmarson[11] (see Fig. 1.2).

As can be seen from Fig. 1.2 (the shaded area corresponds to the conduction band), the N impurity level in GaAs lies *inside the conduction band*. For $x > 0.2$, in the case of GaP and GaAs$_{1-x}$P$_x$, the N levels are inside the band gap. They are quite insensitive to pressure or temperature change, like the atomic levels. The same is valid also for the N in the InGaAs alloy: the N levels are also inside the conduction band. The N-energy levels in the GaAs have the property of being much less sensitive to hydrostatic pressure than the energy minimum of the conduction-band. That is, by applying hydrostatic pressure on the sample, the conduction band electronic levels move upwards and leave the N impurity levels exposed inside the band gap (at a pressure of about 2,2 GPa)[12].

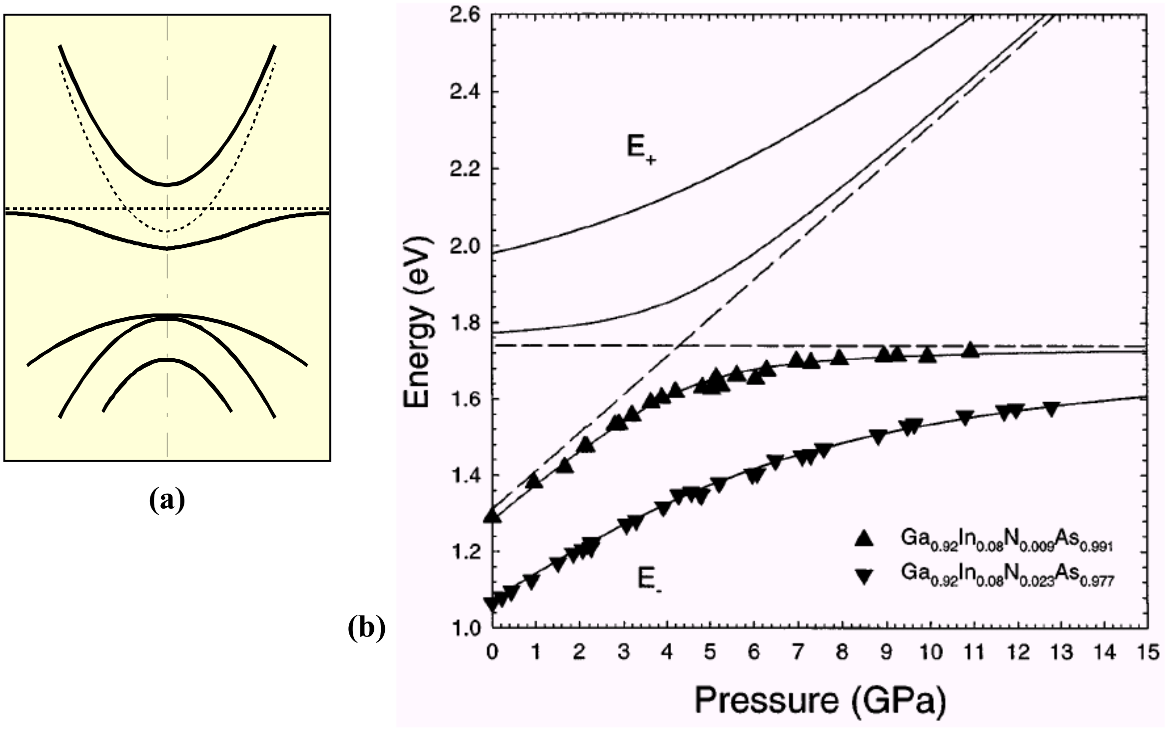

Fig. 1.3: The empirical band-anticrossing model for the InGaAsN alloy: **(a)** a simplified, intuitive picture of the model is depicted, **(b)** experimental evidence based on measurement of the conduction band minimum dependence on hydrostatic pressure (from reference [13]).

What happens when the N concentration increases? There are two models, which describe this situation. One is phenomenological, the other is based on pseudo-potential calculations. Both of them predict a strong red shift of the band gap of GaAsN and InGaAsN alloys together with an increase in the electron effective mass.

The first model, called *band anticrossing model* (see Fig. 1.3) is due to Shan *et al.*[13]. Based on experimental evidence [pressure-dependent electro-reflectance experiments, see Fig. 1.3 (b)], a strong interaction between the conduction band and the N-states (located inside the conduction band) is assumed, leading to a “repulsion” of the conduction band edge and a red shift of the band gap:

$$E_{\pm} = \frac{E_N + E_M \pm \sqrt{(E_N - E_M)^2 + 4V_{MN}^2}}{2} \tag{1.2}$$

where E_N and E_M are the energies of the InGaAs matrix conduction band edge and of the N level relative to the top of the valence band. The V_{MN} is the coupling parameter between the E_N and E_M energy levels and increases with increasing N composition[13] (for $In_{0.08}Ga_{0.92}As_{1-x}N_x$ it changes from $V_{MN} = 0.12$ eV for $x = 0.009$ to 0.4 eV for $x = 0.023$). This model is empirical; the experimental evidence of this model is based on photoreflectance measurements, where the E_+ and E_- bands can be seen directly. The interaction between the conduction band and the N-states leads to a hybridization of the E_+ and E_- states [see Fig. 1.3 (a)].

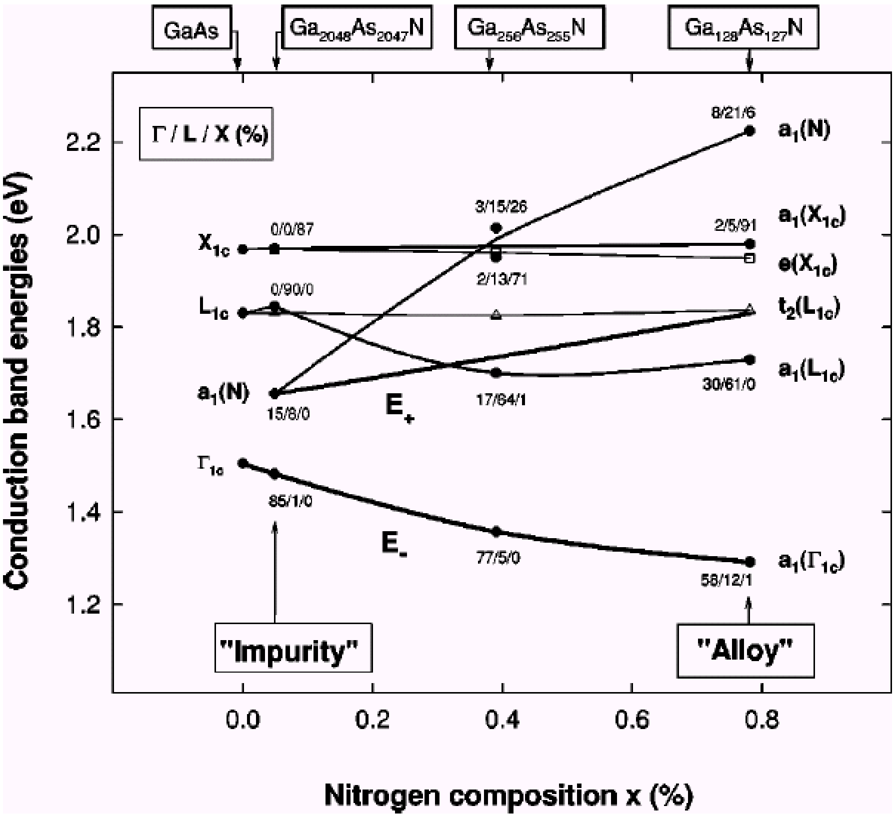

Fig. 1.4: The electronic structure of GaAsN alloy based on calculations using a plane-wave pseudopotential method and large supercells (from reference [14]).

The second model[14] makes predictions about the electronic structure of N-containing GaAsN and InGaAsN alloys based on calculations using the (plane wave) pseudo-potential method and large supercells (see Fig. 1.4). In Fig. 1.4 the E_+ and E_- electronic states are also depicted. In this model, E_- is the bottom of the conduction band. It is a mixture of Γ, X and L conduction bands and due to this fact it is a *localized* state (around the Ga-atoms nearest to nitrogen). This kind of localization must be understood differently from the localization of the gap-states represented in Fig. 1.5. Far away from nitrogen, the E_--states have extended character (E_- represents the minimum of the conduction band). Because the amount of the Γ state decreases with increasing N content, this model predicts a reduction of the matrix element for optical transitions between the valence and conduction bands. The E_+ appears when an averaging over the supercells (in this supercells the N atoms are randomly distributed) used in calculations is made. It is a mixture between the localized $a_1(N)$-state and the perturbed (by the presence of nitrogen) $a_1(L_{1c})$-states. This theoretical model predicts a delocalization of the E_+ states with increasing N content (for low N concentrations, in the N-impurity limit, these states are localized). Here a_1 is the symmetry of the N impurity state as described in the reference [11].

The second model predicts N-related states in the band gap of the GaAsN[15, 16] (see Fig. 1.5) and band tail states in the InGaAsN[17] material. In GaAsN, these N-related states are due to N cluster and chains and have energy much below the conduction band minimum (up to 500 meV). For InGaAsN (reference [17]), band tail states (extended over circa 100 meV) and different band gaps for 2% N, depending on whether the alloy is random or ordered (that is, more In-N bonds are present than in the random case), are predicted.

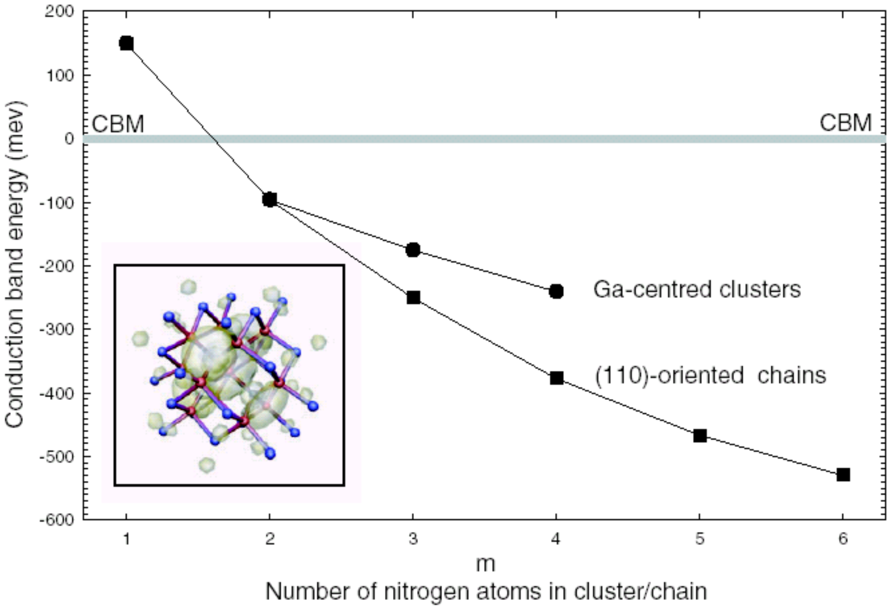

Fig. 1.5: N-related electronic states in the band gap of GaAs based on pseudopotential calculations. These states are due to N-cluster and chains. In the inset: wavefunction isosurface of cluster state, which shows strong nitrogen localization (from reference [16]).

The influence of N on the conduction/valence band extremum. Band offsets.

The band-anticrossing model predicts a strong influence of N on the conduction band (a decrease in the energy of conduction band minimum). The influence on the valence band is indirect (weak) and not clear. Calculations based on pseudopotential method indicate[5] that in GaAsN the nitrogen lowers the energy of the conduction band minimum and raises the energy of conduction band maximum. This suggests a type I band alignment for GaAs/GaAsN/GaAs QWs. However, the band offsets of QW-structures are additionally influenced by strain. Experimentally, it was proved that the GaAs/InGaAsN/GaAs is a type I QW-structure[54]. For GaAs/GaAsN/GaAs QW-structures, it is still debated if the band alignment is of type I or II[58].

1.4. Bowing parameter of the (In)GaAsN alloy

The band gap of a semiconductor alloy, a mixture of two semiconductor materials A and B with fractions x and $(1-x)$, has a dependence on the composition well approximated by a parabola:

$$E_g^{A_xB_{1-x}} = xE_g^A + (1-x)E_g^B - bx(1-x) \qquad (1.3)$$

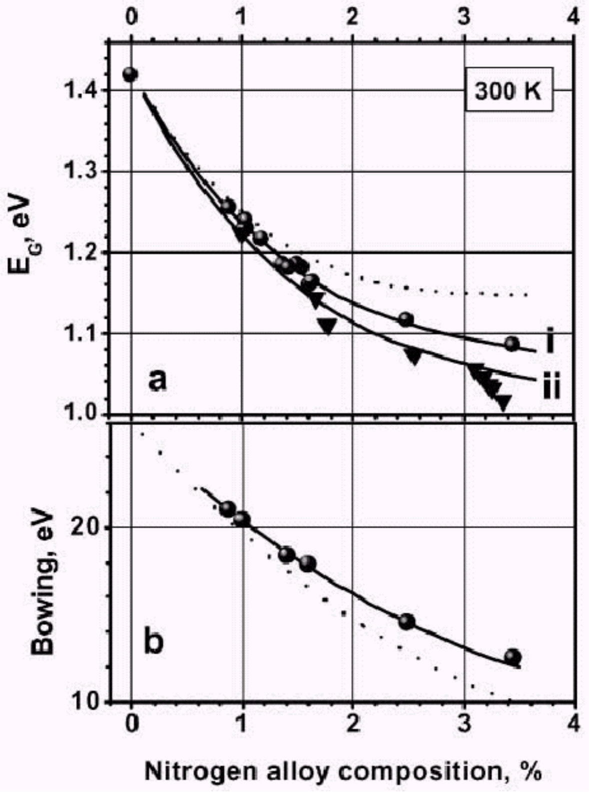

Fig. 1.6: (a) Band gap energy for tensile-strained GaAsN alloy grown on GaAs [circles, curve (i)]; dotted line: unstrained GaAsN) and InGaAsN strain-compensated alloy (triangles) versus N-content at 300 K [curve (ii) presents the band gap energy of quaternary InGaAsN alloy lattice-matched to GaAs]; **(b)** Bowing parameter of band gap energy of GaAsN for tensile-strained dilute alloys (dotted line: unstrained GaAsN alloy) (from reference [10]).

where E_g^A and E_g^B are the band gaps of the semiconductor materials A and B (which can be also alloys) and b the so-called bowing coefficient. The great majority of the semiconductor alloys have a small bowing coefficient, that is, the band gap of the composite material can be (with good precision) linearly interpolated from the band gaps of the constituents A and B (which can be also alloys). There is a category of semiconductors alloys, which has a large bowing coefficient. The InGaAs alloy has a small bowing coefficient [seen as an alloy (A=)GaAs - (B=)InAs], InGaAsN and GaAsN alloys have a large[10, 18], N-composition dependent bowing coefficient (more than 20 eV for low N-content, see Fig. 1.6). Calculations indicate that the large bowing coefficient in the (In)GaAsN alloy is mainly due to two effects: *charge exchange* between As- and N-atoms (proportional to the atomic orbital differences between As- and N-atoms) and *structural relaxation* (proportional to the As-N atomic size differences)[19].

It is this large bowing coefficient, which allows the strong reduction of the band gap for low N composition and the use of InGaAsN for 1.3 µm lasers.

1.5. Carrier localization and potential fluctuations

Any ternary and quaternary semiconductor alloy has potential fluctuations of conduction/valence bands, due to the random distribution of the group III and V elements on respective lattice sites. The potential fluctuations lead to the effect of carrier localization. This random distribution of group III and V atoms has negative influence on the optical quality of the samples: it causes inhomogeneous broadening of the photoluminescence (PL). This effect may be accentuated in quantum wells due to strain and has negative impact on laser characteristics.

For the particular case of InGaAsN quantum wells, the localization effects may be accentuated by the instability of the InGaAsN material during growth. It is one of the challenges of the technology to control the homogeneity of InGaAsN quantum wells in order to obtain small inhomogeneous broadening of the photoluminescence.

1.6. Thermal Annealing

As a consequence of the inferior quality of the as-grown (In)GaAsN material, thermal annealing of the samples is necessary. The annealing temperature is usually between 700 and 720°C. Lower temperatures have a small effect on samples: under 650°C the effect is very low. Higher temperatures destroy the samples, because of the high rate of GaAs evaporation. Regarding the annealing time, it is between 10 and 30 minutes. The changes caused in the samples by annealing are most important in the first few minutes. Some authors have studied also the so-called rapid thermal annealing (RTA), where the annealing time is between seconds and tens of seconds[20]. RTA has roughly the same effect on samples like the normal annealing.

Concerning the microscopic origin of the blue shift after thermal annealing, there are three opinions in the international scientific community. Transmission electron microscopy studies[21], [22], presented in §3.4, indicate that after thermal annealing the samples become more homogeneous and that profiles of the In and N concentration in quantum well change after thermal annealing. These structural changes can explain the blue shift. Klar *et al.*[23, 24] offers another explanation for the blue shift by the movements of the nitrogen from the Ga-rich sites to In-rich sites after thermal annealing, without changing the overall alloy composition. Spruytte *et al.*[25] observe also modifications of Ga-N bond after thermal annealing and a high concentration of interstitial N-atoms that disappears after thermal annealing. Finally, Grenouillet *et al.*[20] conclude a N-reorganization *inside* (and not diffusion outside) the GaAsN material during thermal annealing.

1.7. Structure of this work

In the next chapter (Chapter 2) the *materials and experimental methods* (experimental setups) used in this work are described.

In the following three chapters (3 to 5), the results of this work are presented:

- optical properties of MBE-grown InGaAsN quantum wells (Chapter 3):
    - optical absorption;
    - general photoluminescence properties of InGaAsN quantum well samples;
    - influence of growth parameters, thermal annealing, and QW-parameters (In- and N-composition, thickness) on the photoluminescence properties;
    - models which explain the photoluminescence properties in InGaAsN quantum wells and the effect of thermal annealing;
    - influence of carrier-localization effects on the PL-properties of InGaAsN QW-samples;
    - time-resolved photoluminescence in QW-samples grown under different conditions: derivation of radiative and non-radiative recombination times;
- band offsets measurement in quantum wells (Chapter 4):
    - a novel method is introduced, developed by the author of this work, and which allows band offsets measurements in QW-structures, for both type I and II band alignment;
    - results for type I and type II QW-structures are presented (for InGaAs, InGaAsN, GaAsSb and GaAsN quantum wells grown on GaAs substrates);
    - the influence of nitrogen on both the valence and conduction bands of InGaAsN QW-structures is determined;
- transport properties in InGaAsN MBE-grown samples (Chapter 5):

- photocurrent measurements in InGaAsN QW-samples are carried out in order to obtain information about the in-plane transport and carrier localization in InGaAsN quantum wells;
- cyclotron resonance experiments performed in InGaAsN samples, in order to determine the effective electron and hole masses.

At the end of the work, a summary of the results is presented.

The photoluminescence quality of InGaAsN QWs influences directly the laser characteristics. In §3.2, the general properties of the photoluminescence in InGaAsN QWs are discussed. Experiments are carried out in order to confirm experimentally the sample structure presented in Chapter 2. In §3.1 and §3.3, optical absorption and photoluminescence measurements are performed in order to find out how different parameters (thickness, barriers, In- and N-compositions) influence the optical quality of quantum wells. In §3.4, a model which explains the photoluminescence mechanism and the effect of thermal annealing in InGaAsN quantum wells is proposed. The model is experimentally supported by Transmission Electron Microscopy (TEM) studies.

The thermal annealing has an important influence on the structural and optical properties of (In)GaAsN samples. The photoluminescence intensity in as-grown samples is not good enough at room temperature and thermal annealing must be performed. An improvement usually follows after thermal annealing. Consequently, the effect of annealing on the optical properties of InGaAsN quantum wells represents an important part of the studies performed in Chapter 3.

The InGaAsN QWs show in-plane spatial potential fluctuations of the conduction/ valence band (see Chapters 3), depending on the growth conditions. In some samples, an important part of these potential fluctuations are due to inhomogeneity in material composition and/or QW-thickness. This can be seen directly in transmission electron microscopy (TEM) images and indirectly in the photoluminescence properties of these samples. The potential fluctuations lead to *carrier localization effects*; these effects are very important in InGaAsN quantum wells. The influence of the carrier localization on the photoluminescence of InGaAsN QW-samples is studied in §3.5 and §3.6.

The band offsets of GaAs/InGaAsN/GaAs quantum wells have a strong influence on laser characteristics, as discussed in above in this chapter. This fact justifies the studies performed in Chapter 4, besides the fundamental importance of knowing the influence of nitrogen on the conduction/valence band extrema.

In Chapter 5, the measurement of *electron and hole effective masses in InGaAsN* is attempted by performing cyclotron resonance experiments.

Chapter 2
Materials and Experimental Methods

In this chapter, the structure of the studied samples and the experimental methods used in this work are presented. The structure of the studied samples depends also on the particular method used. Additional information about the structure of the sample is supplied, when needed, in the next chapters. If there are aspects of some methods, which are too complex to be explained in detail here, then suitable references from the literature are given.

If not otherwise mentioned, the experiments were performed at Infineon Technologies AG.

2.1. Sample structure

To explain the general structure of the samples, which is represented in Fig. 2.2, some details about the growth of InGaAsN QW-samples are discussed before.

In Fig. 2.1, the evolution in time of the relevant growth parameters during the growth of a typical, single QW-sample is depicted. T represents the (substrate) growth temperature, P is the pressure in the growth chamber, and N is concentration of nitrogen in the sample. Before starting the growth process, the surface of the substrate (which is oxidized) must be prepared. This takes place by heating the substrate at 650°C; during this process the As-shutter is open, to compensate for the As-desorption.

As explained in Introduction, the growth temperature of the InGaAsN is low, around 420°C. The growth temperature of the AlGaAs and of GaAs is 600°C. It takes around 5 minutes to change the temperature between 420 to 600°C and to stabilize it. The temperature is lowered 2 minutes after the N-plasma ignition.

During the growth of GaAs, the pressure in the growth chamber is around 10^{-6} mbar, mostly due to As-pressure. During the growth of the AlAs/GaAs barriers, the pressure varies slightly due to a lower pumping efficiency of the Al element. When the plasma is ignited, there is a sudden increase of the pressure. It takes about 4 minutes for the stabilization of the N-plasma. During this time the RF-power is reduced from 500 to 200 W. In the same time the pressure of the N_2-gas fed into the N-plasma cell is reduced. There is also a sudden increase of the pressure when the RF-power is switched off. This is due to the different pumping efficiency for N and N_2.

From the N curve in Fig. 2.1, one can see that not only the quantum well contains nitrogen, but also the barriers around it. This is due to the fact that the shutter of the N-cell cannot completely prevent the N-atom from coming out of the cell. The AlGaAs

(AlAs/GaAs) barriers must not contain nitrogen, otherwise their quality is poor. Due to this fact, the ignition of the plasma must take place after the growth of the first AlGaAs barrier, and the cell must be switched off before the second AlGaAs barrier is grown. During the plasma ignition, about 0.5% nitrogen is incorporated in the sample; this leads to the formation of a parasitic quantum well, which is clearly seen in the photoluminescence spectra. During the growth at low temperature (420°C), about 0.2% of nitrogen is incorporated in the barriers. This leads to the structure of the sample presented in Fig. 2.2. By the switching off of the plasma, there is no incorporation of nitrogen in the sample due to the small sticking coefficient of the N_2 molecules.

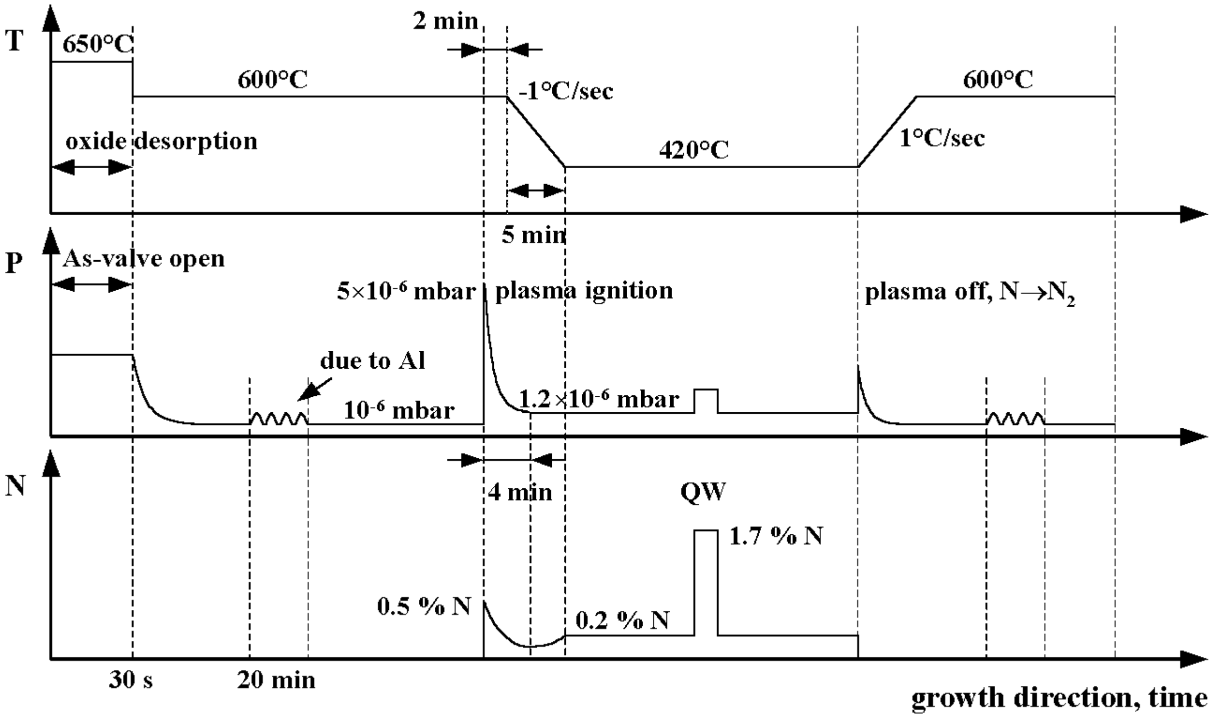

Fig. 2.1: The evolution of the growth parameters during MBE growth of a single InGaAsN QW-sample. *T* is the growth temperature, *P* is the pressure in the growth chamber, and *N* is the nitrogen content in the (In)GaAsN QW-sample. For reasons of clarity, the *x*-axis is not linear. The geometrical structure of the sample is depicted in Fig. 2.2.

The typical structure of the samples is presented in Fig. 2.2. All the samples studied in this work are grown on GaAs substrates. The samples used in Chapter 4 are grown on n-doped substrates; otherwise semi-insulating substrates are used. The grown region contains:

- a GaAs buffer layer;

- two AlGaAs confinement layers (which may also be grown as a superlattice GaAs/AlAs, with periodicity of roughly 2 nm). This is helpful when studying the photoluminescence of the samples: the AlGaAs barriers prevent the photo-excited carriers from recombination in the substrate (which has a lower optical quality) or at the surface (in GaAs the surface recombination is very important). The AlGaAs barriers have a negative influence when making contacts to the sample (Chapter 5) or when studying photovoltage (Chapter 4). Whenever the sample structure differs from the one depicted in Fig. 2.2, this will be mentioned;

- (In)GaAs(N) barriers, of thickness depending from sample to sample. When multiple QWs are grown, the barrier between the different QWs is 20 - 30 nm. As explained before (see Fig. 2.1), when (In)GaAsN QWs are grown, the barriers around the QWs contain nitrogen. Additionally, when the N-plasma ignition takes place, a GaAsN QW is formed (see Fig. 2.1 and Chapter 3). The barriers do not contain nitrogen when InGaAs QWs are grown.

- the QWs. The InGaAsN QWs used for optical emission around 1.3 µm are strained. Thickness and composition vary from sample to sample. The thickness of the QWs is between 4 and 10 nm. The composition for 1.3 µm emission is around 1.7% nitrogen and 25 - 40% indium;

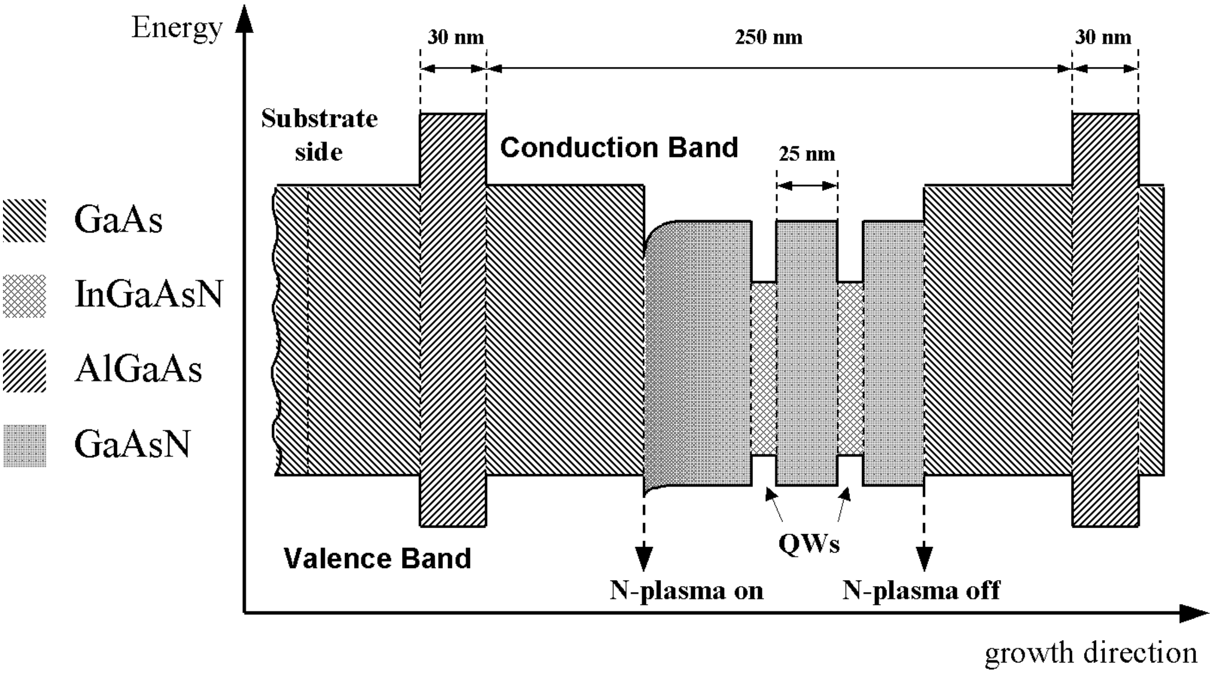

Fig. 2.2: The general structure of the samples. The dimensions given are typical; they vary from sample to sample.

In this work it is often referred to (In)GaAsN *QW*- and *bulk*-samples. The QW-samples contain thin layers (4 - 10 nm) of, e.g. InGaAsN material. The bulk-samples contain thick layers of the material (hundreds of nm). The QW-samples cannot be grown too thick, because usually they have a high In-content and are strained (the lattice constants of the QW- and barrier-materials are different). If the quantum wells are grown too thick, dislocations and defects may appear in the QW-material and consequently the samples have poor optical properties. If the lattice constant of the QW-material is larger than the lattice constant of the barriers, the QW is compressive strained (InGaAs QWs grown on GaAs); if the opposite is true, the QW is tensile strained (GaAsN QWs grown on GaAs). The quantization of electron and/or hole energy levels in QW-samples is very accentuated (there are only a few of them) and must always be taken into consideration. On the contrary, in the bulk samples the quantized electron and/or hole energy levels are numerous; here the quantization of energy levels is not important. The bulk samples must be grown, due to their large thickness, lattice-matched to the barrier material.

2.2. Photothermal deflection spectroscopy (PDS)

The experimental setup is presented[26] in Fig. 2.3 and was built by the author of this work.

Description of the setup

The heart of the system is a special transparent liquid (perfluorohexane), which has a very pronounced dependence of the refraction index on temperature. The sample stays inside the liquid during the measurement. Chopped monochromatic light (*pump beam*) is projected on the sample, which is partly absorbed and consequently heats the sample. The image of the projected light, which passes through the monochromator, is a strip of about 5 mm length and 1 mm thickness. The light intensity should be as high as possible for a good sensitivity (a 400 W halogen lamp was used). A well-collimated (50 µm thickness) He-Ne laser beam (*probe beam*) runs very close and parallel to the sample. The probe beam is deflected in the liquid, which has a gradient in the refraction index as a consequence of the heat produced in the sample by the absorption of the pumping beam. The deflection of the laser beam (and the absorption in the sample) is measured by a position-sensitive detector. The light transmitted through the sample is as well measured, by a pyroelectric detector.

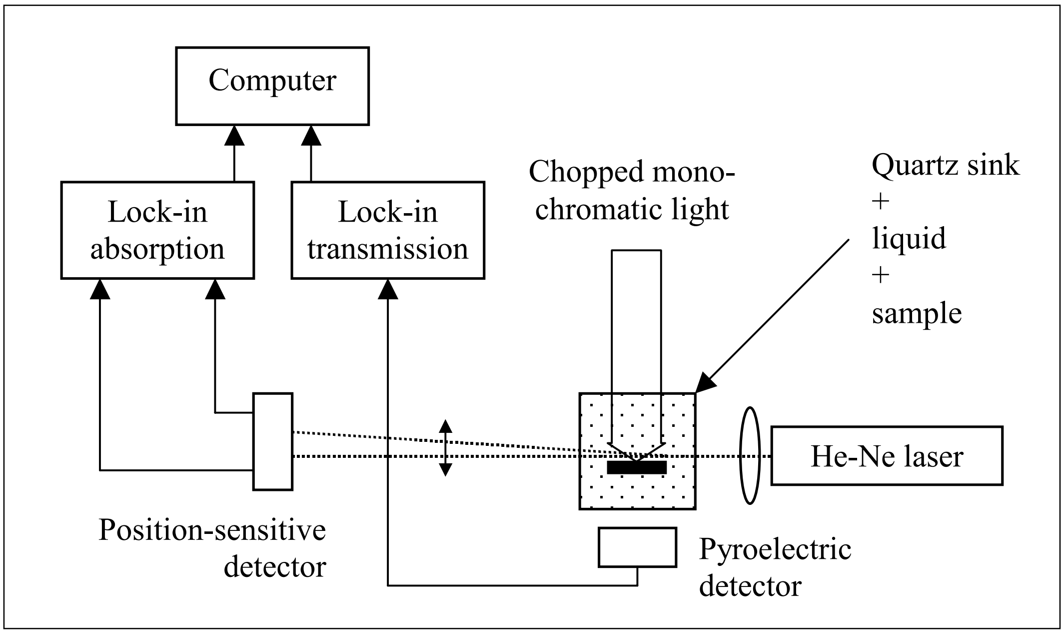

Fig. 2.3: Schematics of the PDS experimental setup. The laser beam is deflected in the liquid due to the heat produced by absorption of the chopped monochromatic light in the sample.

How the method works

The samples were measured in the transverse PDS geometry (depicted in Fig. 2.3). The theory of the PDS is relatively complex and can be found in the original work (1981) by Jackson *et al.*[26]. Here only the basics of the method are described.

By optical absorption in the sample, highly damped (the liquid has a poor thermal conductivity) thermal waves are generated in the liquid and which vary in time with the frequency of the chopped pump beam. In order to increase the sensitivity of the method, the liquid around the sample must have a strong dependence of the refraction index on temperature. The deflection of the probe beam depends on the temperature *gradient* along its way through the liquid. The deflection of the probe beam is proportional to the amplitude of the thermal wave at the position of the beam. This means that the probe beam has to be within a distance of a few thermal lengths (tens of µm, see further) from the sample, to reach a high sensitivity of the measurements.

The thermal waves decay exponentially, with a constant called *thermal length*, given by the following relation:

$$l_{th} = \sqrt{\frac{\kappa}{\rho \cdot C \cdot \omega}} \tag{2.1}$$

where κ, ρ and C are the thermal conductivity, density and thermal capacity of the medium, respectively, and ω is the frequency of the chopped pump beam. For GaAs, the thermal length is ≈0.74 mm. This is the length over which the thermal waves are damped in GaAs. To maximize the temperature variation produced in the sample by optical absorption (and the sensitivity of the method), the samples were thinned down to ≈50 µm. The thermal length in the liquid used is ≈10 µm and so the alignment of the probe beam is critical, in order to reach a high sensitivity of measurements. Due to this fact it follows one of the weak points of the method: the high sensitivity to external mechanical vibrations, as a source of noise. A second weak point is that only room temperature measurements can be performed (at low temperatures, the liquid freezes). This method has a major advantage: the good sensitivity[26] ($\alpha d \approx 10^{-4}$). It is possible (see Chapter 3), to measure the absorption of a single QW.

Sample preparation

The samples were grown on 500 - 600 µm thick GaAs substrate. The samples were thinned down to 50 µm by two processes:

- the samples were mechanically polished down to about 100 µm. The back surface of the sample is rough and this would cause strong light scattering. That is why the next step is necessary;

- the samples were chemically etched down to about 70 µm. An etching solution flows *parallel* to the polished surface of the sample. By chemical etching the roughness of the sample-surface caused by the mechanical polish process is much reduced. This is important, in order to reduce the scattering of the transmitted light, which is not taken into consideration by the normalization of the measurements (see further). After chemical etching, the back surface of the sample is shiny but nor mirror-like. This has the advantage of preventing the formation of light standing waves in the sample: indeed, the transmitted signal does not show any oscillations.

Normalization procedure

The transmitted light is used to normalize the absorption spectrum with the spectral function of the whole system.

The light that enters the sample is absorbed, scattered or transmitted through the sample. There are two effects that are not taken into consideration in the normalization procedure, but whose effect on the precision of the measurements is strongly reduced by the sample preparation process. The first is the light scattering on the back surface of the sample. By chemical etching the light scattering is reduced as much as possible. However, not this scattered light is important in itself, but its dependence on light wavelength, because the transmitted signal is normalized to unity. The second effect is the standing waves, which can appear in the samples. This effect eliminated by the sample preparation because the back surface is not mirror like. Even if such standing waves appear in the region of the quantum well, their effect is eliminated by the averaging that takes place due to the fact that the probe beam runs parallel to the surface of the sample, on a long distance (few mm).

The normalization procedure takes place in the following steps:

1) the electrical signals collected from the two detectors are normalized to one (i.e. they are divided by the maximum value over the spectral range) and are compared. They will be called A (absorption) and T (transmission). The explanation of this normalization is clear for A. The transmission T is normalized to one, because it should represent the transmission *inside* the sample (between two planes inside the sample, very close and parallel to the front and back surfaces of the sample). As the detector cannot be placed *inside* the sample, the detector is placed as indicated in Fig. 2.3, but the transmission will be normalized to unity. This introduces small errors due to the spectral dependence of the light transmission through the liquid and container (quartz sink);

2) the crossing point of the two curves is calculated: if the sources of errors mentioned above are neglected, the y -value of the crossing point should be 0.5. Actually this value is ≈0.4;

3) by neglecting the light reflection on the back surface of the sample, which is important only for $\alpha d << 1$ ($T = e^{-\alpha d}$, $A \approx 1 - T$), the αd value is calculated with the relation:

$$\alpha d \approx \ln(1 + \frac{A}{T}) \tag{2.2}$$

4) At the photon energy of the crossing point, the value $\ln(1+\frac{A}{T})=\ln 2\approx 0.69$ is assigned, which corresponds to the condition $A=T=0.5$;

Certainly, errors are introduced in the measurements by neglecting the different effects mentioned above. The method is certainly not *exact* for the measurement of absolute values of αd. Another effect, which is neglected, is the reflection of the light on the back surface of the sample. This reflection is important only under the band gap of the substrate, where the absorption in the sample is small, $\alpha d << 1$. The refraction index of GaAs (at 300 K) varies between 3.32 at 0.7 eV and 3.55 at 1.43 eV (near the GaAs fundamental band gap). The refraction coefficient of the liquid is about 1.25. For small incidence angles on the back surface of the sample, the reflection coefficient varies between 0.21 and 0.23. This reflection was however not taken into consideration, because the smoothness of the back surface of samples was not studied. It is different for different samples and additionally the reflected light depends on the photon energy. From experience (more than 100 spectra of identical and different samples were measured), the absolute precision of the PDS-method (for the case of this experimental setup) is estimated to be +100/-50%. The reliability of the method is improved when samples prepared under identical conditions are compared, as it is the case in Chapter 3.

The PDS experiments were performed at the Technical University of Munich, in the Physics Department E16.

2.3. Photoluminescence, continuos excitation and time resolved

The experimental setup of continuos excitation photoluminescence (PL) is commonly known. As excitation, light from two lasers (He-Ne (632 nm) laser and Ar-ion (514 nm) laser) is used. To detect the PL, Ge-detector operating at 77 K was used. A closed-cycle cryostat was used to vary the temperature of the sample between 14 and 300 K. The He-Ne laser has a maximum light power of 10 mW, the Ar-ion laser of maximum 1 W. By adding gray filters the light can be attenuated by factors of 2, 5, 10, 20, 50, 100, 200... The light from the lasers can be focused on a spot of diameter of minimum 40 µm on the sample.

The spectral sensitivity of the Ge-detector is between 800 and 1700 nm. In this range the spectral sensitivity of the system (the spectrometer, the detector) varies over roughly 2 orders of magnitude, with a maximum around 1300 nm. That’s why the spectra have to be normalized on this spectral sensitivity of the system. A program was written in LabView™ to take a PL spectrum, which does this normalization automatically.

The time-resolved PL measurements were done using laser pulses and a streak camera. The essentials of the used experimental setup are shown in Fig. 2.4. Short (Ti-sapphire) laser pulses (80 fs) with a repetition rate of 80 MHz are used to excite the sample. The photoluminescence is passed through a spectrometer and projected on a near-IR sensitive photocathode. With every light pulse, the lasers gives a synchronization signal that starts the deflection of the electrons beam generated in photocathode by the photoluminescence of the sample. As seen in Fig. 2.4, a streak camera plots the time-resolved PL as a function of time in the form of an image (y-axis is time, x-axis is the PL emission wavelength). The time resolution of the system, which was used, is around 10 ps. The whole y-axis covers about 1 ns, the spectral window (the x-axis) covered is around 250 nm wide. The image is taken by a CCD-camera connected to a computer.

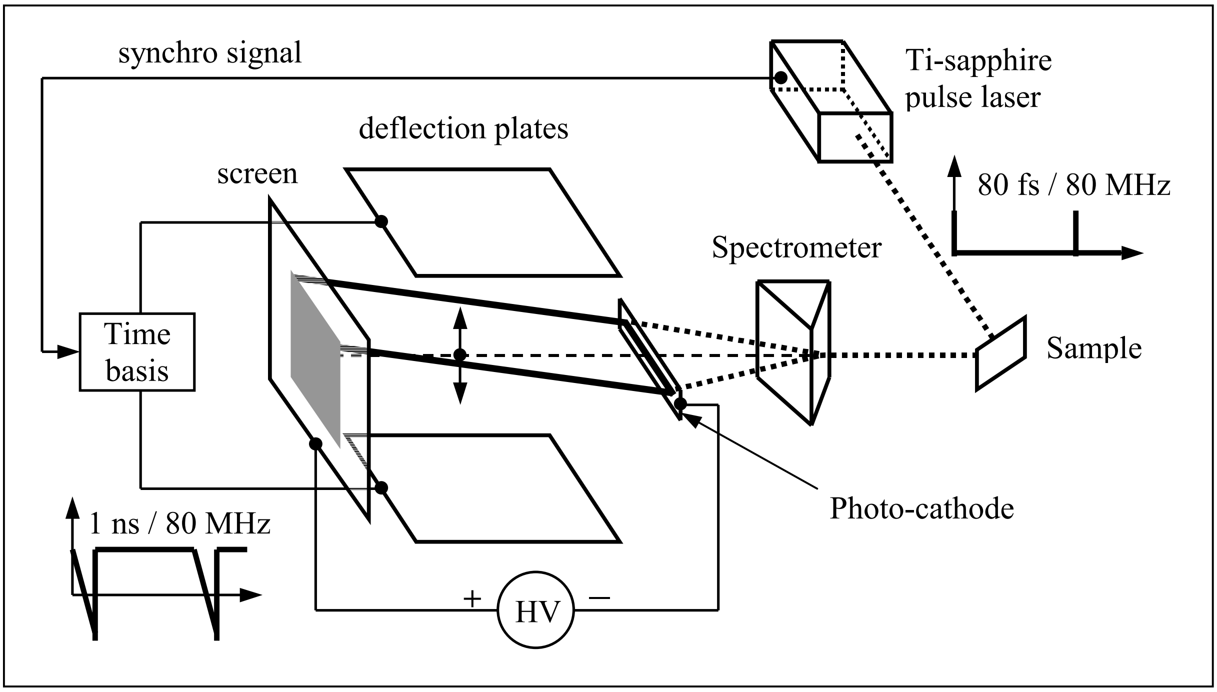

Fig. 2.4: Time-resolved photoluminescence setup (streak camera). The image from the screen is transmitted through a CCD-camera to a computer. To simplify the figure, the lens-systems used to collimate the optical/electronic beams are not represented in the figure.

The time-resolved measurements were performed at the Philipps University of Marburg.

2.4. Surface Photovoltage

The Surface Photovoltage (SPV) setup is presented in Fig. 2.5. It was the idea of the author of this work to perform this measurement in order to measure the band offsets in QW-structures. The author also built the measurement setup. In this experiment, small variations in the photovoltage, which are generated near the surface, are measured. The theoretical principles of the method are discussed fully in Chapter 4.

The sample is sandwiched between the metallic cryostat sample holder and a transparent electrode (ITO - Indium Tin Oxide, on glass) and is illuminated with monochromatic light (from a laser or from a white lamp light passed through a monochromator). The light is chopped with a frequency of a few tens of Hz (10 - 80 Hz) causing periodical variations in the photovoltage generated in the sample. The coupling between the transparent electrode and the sample is capacitive (called also soft contact) and the buffer collects only variations in photovoltage. The buffer is necessary because the capacitive contact must work on high impedance (a few GΩ), which the buffer has at the input. The output of the buffer is connected to the lock-in amplifier or to the oscilloscope.

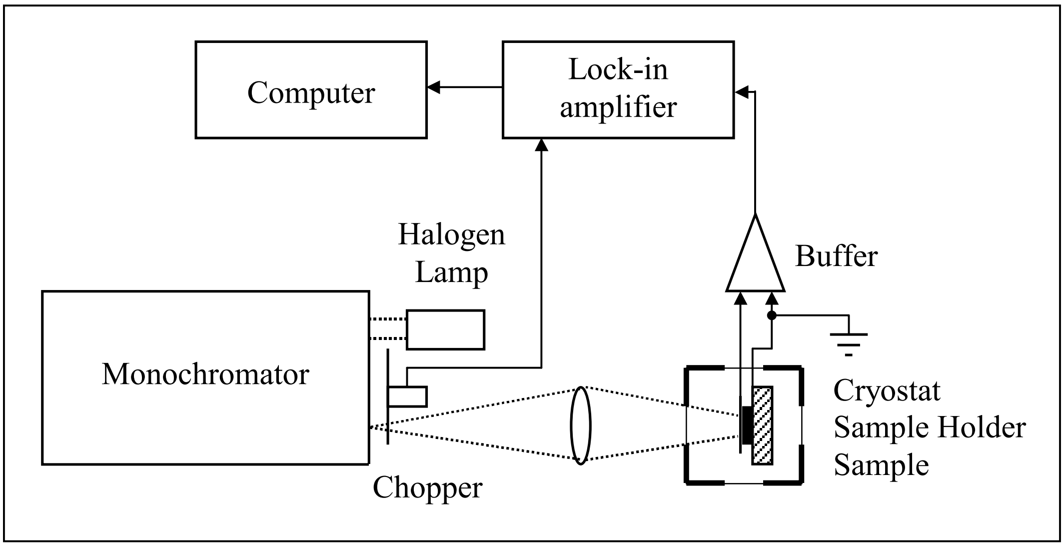

Fig. 2.5: Surface Photovoltage measurement setup. Further details are given in Chapter 4.

Because the whole transversal photovoltage generated in the sample is collected, including that generated in the substrate, it is necessary that the samples be grown on doped substrate. The aim of these measurements is to study optical transitions in quantum well (QW)-samples. The quantum wells are grown in a non-doped region, where a built-in electric field exists. When chopped light is applied on the sample, variations of the photovoltage are generated only in the non-doped region (where the quantum wells are) and not in the doped substrates. Thus it is guaranteed that only the region containing the quantum wells contribute to the surface photovoltage spectrum, and not the substrate.

The method is very sensitive (can measure optical transitions inside a single QW) and is simple; no ohmic contacts to the sample are required.

2.5. Transport measurements: photocurrent and cyclotron resonance

In order to perform photocurrent experiments, two In-contacts were alloyed on the sample. The shape of the samples is rectangular. The schematics of photocurrent experiments are shown in Fig. 2.7 (a).

During photocurrent measurements, the sample is placed in the cryostat and is illuminated with monochromatic light. An electrical voltage of a few volts is applied on the sample. The current is then recorded as a function of photon energy.

The principle of cyclotron resonance method is based on the measurement of optical transitions between discrete energy levels, which appear as a consequence of an applied magnetic field. The method of cyclotron resonance is very useful to determine the effective mass of electrons and holes in semiconductors. In this work, the cyclotron resonance is measured in QW or thin layers, that is, for a 2D electron gas. It is known that for a 2D electron gas the density of states is step like and given by[27]:

$$N_s(E) = \frac{m}{\pi \hbar^2} \vartheta(E - E_s) \tag{2.3}$$

where E_s is the bottom of the 2D electron gas sub-band, $\vartheta(E)$ is the unity step function, and m is the electron (effective) mass. When a magnetic field B is applied, the density of states is split into discrete energy levels:

$$N_s(E,B) = \frac{2eB}{h} \sum_{n=0}^{\infty} \delta[E - E_s - (n + \frac{1}{2})\hbar\omega_c] \tag{2.4}$$

The density of states for the cases with and without magnetic field is depicted in Fig. 2.6.

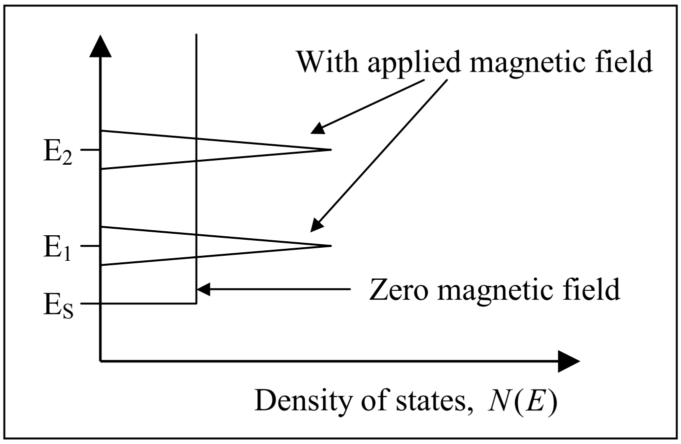

Fig. 2.6: Density of states in a QW with and without magnetic field.

The energy levels E_1, E_2, ... are called Landau levels. It is the optical transition between consecutive Landau levels, which is quantum-mechanically allowed, *which is called cyclotron resonance*. It can be seen in optical transmission of absorption experiments. However, to be able to measure the effective mass of electrons and holes in semiconductors, a condition must be satisfied:

$$\omega_c \tau > 1 \tag{2.5}$$

where $\omega_c = \frac{eB}{m}$ is the cyclotron frequency, and τ represents the mean scattering time of the electrons (holes). In this case a clear resonance is seen. The broadening caused by scattering does not obscure the resonance, or equivalently, the electron is able to complete at least a few orbits before losing its momentum due to scattering.

To measure the cyclotron resonance, time-resolved microwave absorption experiments were used in this work.

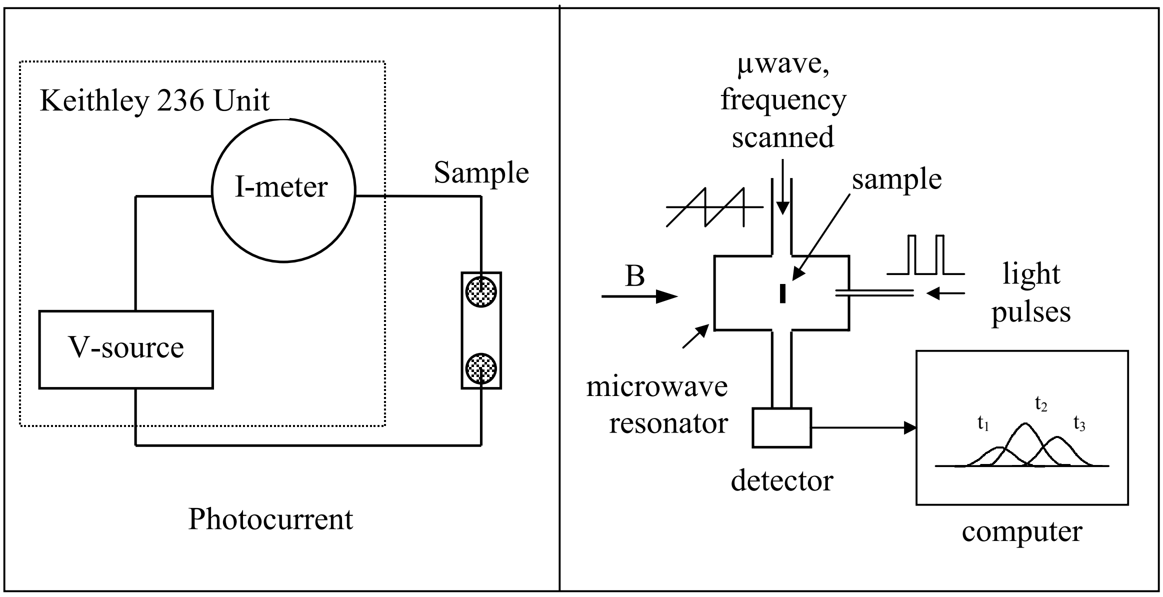

Fig. 2.7: Photocurrent and cyclotron resonance measurement setups. The microwave resonator has a cylindrical geometry with its axis parallel to the applied magnetic field.

The measurement setup is presented schematically in Fig. 2.7 (b). The sample is placed inside a microwave-cavity with a high Q-factor (≈10 000). If the sample is not illuminated, the Q-factor of the cavity is high. If the sample is illuminated, because electron-hole pairs are generated, the Q-factor of the cavity decreases. The sample with the cavity is placed inside a cryostat; a magnetic field is applied perpendicular on the surface of the sample, which is about 70 μm thick. The experimental setup offers the possibility of measuring the time-dependence of the Q-factor and resonance frequency of the cavity, after a light pulse has been applied on the sample. From the time evolution of the Q-factor and resonance frequency, the time-dependence of the complex conductivity (conductance and dielectric constant) can be measured (time resolution: 100 ns).

The microwaves cyclotron resonance experiments were performed at the Technical University of Munich, in the Physics Department E16.

Chapter 3
Optical properties

The purpose of this chapter is to study the influence of quantum well parameters (composition, thickness), growth temperature, and thermal annealing on the optical properties of InGaAsN quantum wells. The experimental methods used are: optical absorption, continuous and time resolved photoluminescence. The results of the experiments performed in this chapter were used as a feedback for the optimization of the molecular beam epitaxy (MBE) growth.

The motivation of this chapter is: (a) the optimization of the quantum well parameters and growth temperature and (b) to understand the photoluminescence mechanism (properties) in InGaAsN quantum wells.

A coarse tuning of the quantum well parameters and is made by performing absorption experiments. The influence of the barrier material is also studied. A finer tuning, for emission around 1.3 μm, followed by performing photoluminescence measurements. The effect of thermal annealing on the samples was studied by absorption, photoluminescence, and Transmission Electron Microscopy (TEM). From these experiments, models of the photoluminescence mechanism in InGaAsN quantum wells are proposed. The influence of growth temperature is studied in relation with carrier localization effects, which are important in InGaAsN quantum wells. Time resolved photoluminescence experiments enable to understand why the photoluminescence intensity decreases with increasing degree of carrier localization.

3.1. Optical absorption studies in InGaAsN samples

The optical absorption of the samples was studied by PDS (Photothermal Deflection Spectroscopy) method at 300 K. The samples were thinned down to about 70 μm as described in Chapter 2.

Taking the example of Fig. 3.1, the typical structure of the spectrum is explained. Around 1.4 eV, there is a strong increase in absorption, due to the GaAs fundamental band gap. Taking the dotted lines as example, there is also a strong increase in absorption around 0.95 eV, due to the effective (i.e. fundamental band gap energy plus the electron and hole quantization energies) band gap of the quantum well(s). Above 0.95 eV, there is some structure in the spectrum: in Fig. 3.1 (b) the arrows indicate probably transitions between different quantized states in the quantum well.

There are three sources of optical absorption in the samples: the quantum well(s), the barriers (which contain nitrogen, as described in Chapter 2), and the substrate. Because the same type of substrate was used when different samples are compared, the changes in optical absorption after thermal annealing (see Fig. 3.1) can come only from structural changes in the quantum well and/or GaAsN barriers. If the density of the band gap states in the QW is reduced after thermal annealing, an essential reduction in the absorption is expected for photon energies *smaller* than the band gap; on the contrary, *above* the band gap, no change in absorption is expected.

For the correct interpretation of the optical absorption results, the effect of thermal annealing on GaAsN as seen in photoluminescence experiments is shortly discussed. In GaAsN one can see an important improvement of the photoluminescence intensity (about 20 times at room temperature). The blue shift of the photoluminescence peak is insignificant. The as-grown (In)GaAsN samples show often a low-energy photoluminescence at low temperature, which is generally reduced after thermal annealing.

3.1.1. Effect of thermal annealing on optical absorption of InGaAsN quantum wells

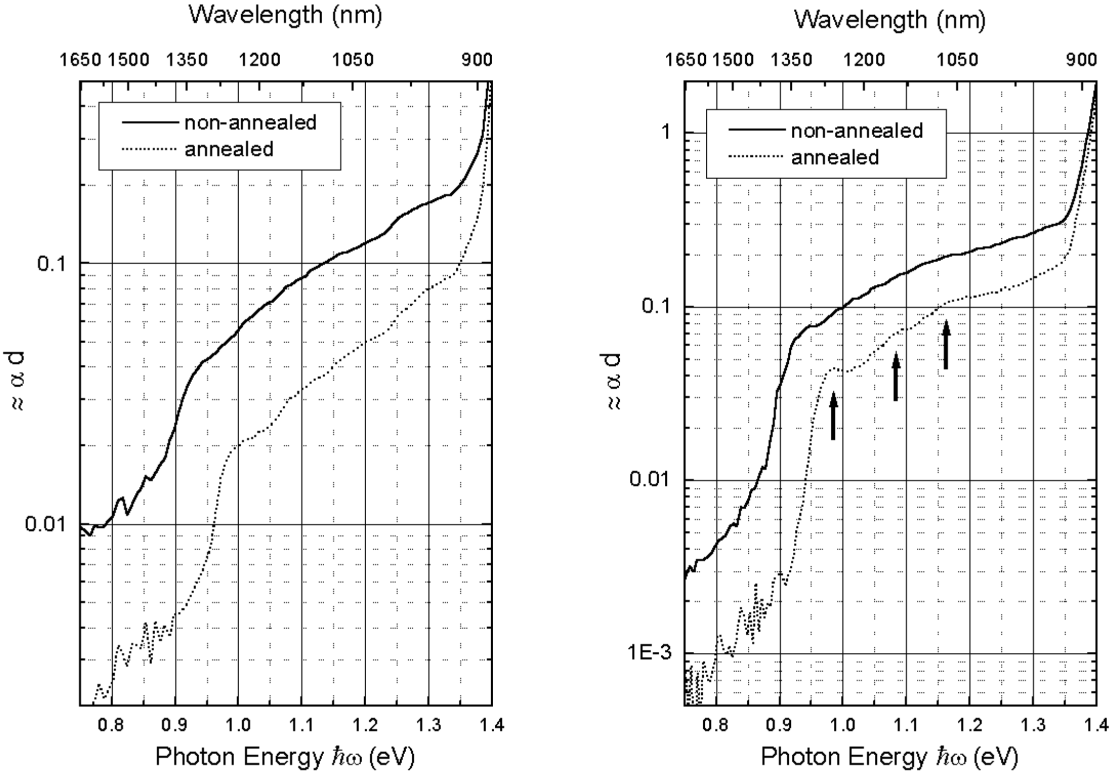

(a) **(b)**

Fig. 3.1: Absorption of **(a)** single and **(b)** five QW samples, before and after thermal annealing. The QW-thickness is 6 nm, the composition: 1.7% N and 35% In. The arrows indicate a structure, which appears in the absorption spectra after thermal annealing, probably coming from optical transitions between quantized states in the quantum wells.

To see the effect of thermal annealing on optical absorption, two different samples are studied in Fig. 3.1: single and multiple QW samples. The second sample contains five QWs. The QW thickness is for both samples 6 nm, the QW-compositions similar: 35% In and 1.7% N. The thermal annealing was performed at 720°C for 15 minutes. Note that on the y-scale an approximate value for αd is plotted in logarithmic scale.

Discussion of results

Regarding the QW-quality, one can see from Fig. 3.1 that after thermal annealing:

- the absorption edge corresponding to the effective band gap of the QW becomes steeper. The sharpness of the absorption edge can be defined by the following quantity, which remains invariant when the spectra are multiplied by a constant:

$$S = \frac{d(\ln \alpha d)}{d(\hbar\omega)} \tag{3.1}$$

- there is structure in the absorption of quantum wells, as indicated by the arrows in Fig. 3.1 (b);

Both these two facts indicate a better quality of the QWs after thermal annealing.

The optical absorption is reduced after thermal annealing for photon energies below the band gap of GaAs (the curves are shifted on y-axis) by about a factor two. As explained above this reduction cannot come alone from the effect of annealing on the quantum wells. The reduction of optical absorption can have two sources:

- the reduction of the sub-band gap absorption of the substrate. This fact is supported by the deep level spectroscopy experiments (not shown here) which show that the deep-level defects-profile of the substrate is strongly changed after thermal annealing: the density of charge traps is reduced;

- the reduction of the sub-band gap absorption of the GaAsN barriers around the QW(s). It is known, as explained at the beginning of this section, that the thermal annealing has a strong effect on the photoluminescence properties of GaAsN.

These two sources of absorption make it difficult to estimate of the αd value of the quantum wells. This value is very different for the two annealed samples shown in Fig. 3.1: 0.02 and 0.009, respectively. One reason for the different, much higher value for the single-QW sample can be the different structure of this sample as compared to the general structure shown in Fig. 2.2. This sample has a single QW grown very close (≈10 nm) to the surface and a different structure of the barriers.

Conclusions

The effects of thermal annealing on the optical absorption of InGaAsN QW-samples, as seen from Fig. 3.1, are:

- the reduction of the absorption coefficient by about a factor of two under the band gap of the GaAs substrate. The reason can be the improvement in quality of GaAsN barriers and/or substrate. This can be correlated with the strong increase in the photoluminescence intensity (see §3.3) of these samples, which suggests that, after thermal annealing, the quality of the GaAsN barriers is improved. The defects present in the GaAsN barriers influence negatively the photoluminescence quality of the samples and contribute to the optical absorption;

- ♦ the blue shift of the band gap, by about 60 meV. This is a well-known effect of thermal annealing in the InGaAsN material;

- ♦ a better optical quality of the quantum wells. This can be seen from the sharper QW-absorption edge, from the structure that appears in the samples after thermal annealing [indicated by the arrows in Fig. 3.1.(b)], and from the excitonic-transition enhancement in absorption spectra (even at room temperature!). No excitonic transition is visible in the non-annealed samples

3.1.2. Influence of barrier material and quantum well thickness on optical absorption of InGaAsN quantum wells

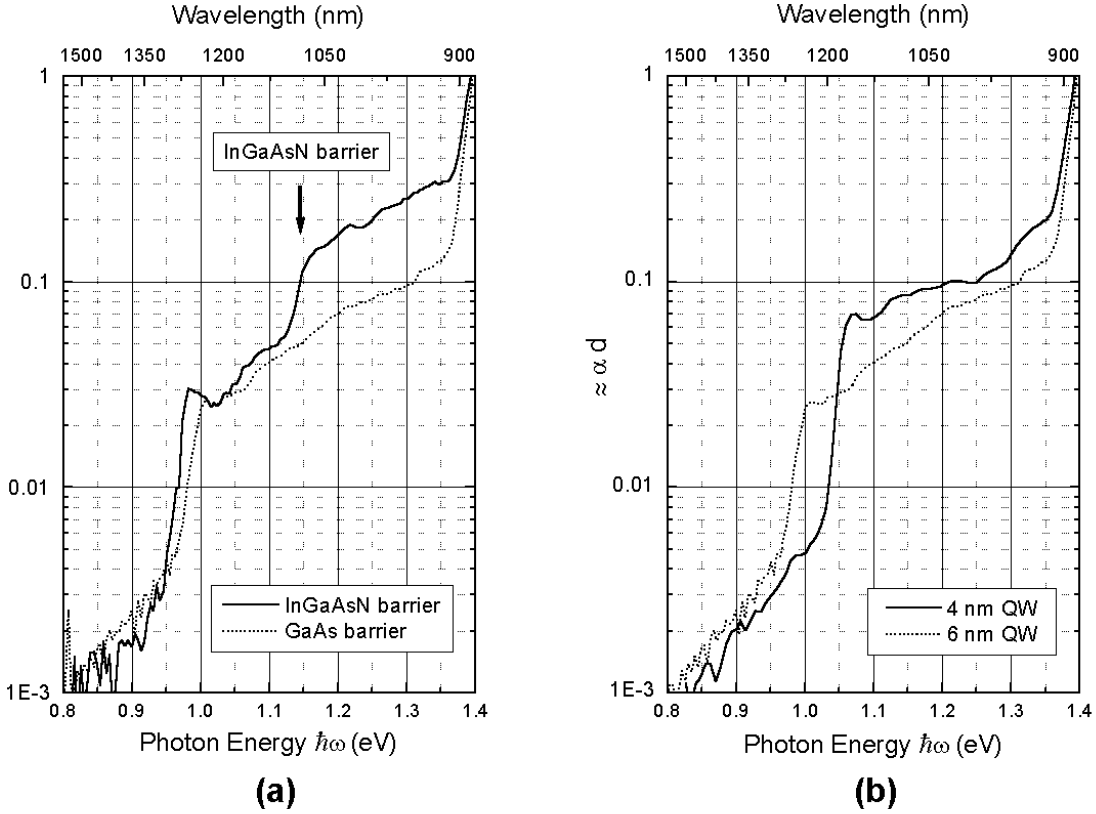

Fig. 3.2: Absorption of similar, annealed QW-samples having **(a)** different barrier material and **(b)** different QW-thickness. The InGaAsN barrier is lattice-matched to GaAs. The sample having 4 nm QW-thickness contains 1.9% N, all the other samples 1.5%. The In-content is 35% for all samples.

To see the influence of the barrier material on the QW quality, similar samples with different barrier materials were studied. The influence of the QW thickness on the optical absorption is studied. The QW thickness *is* an important parameter, because the QWs are strained and because InGaAsN has a strong tendency to 3D-growth.

The results are shown in Fig. 3.2. All the samples were annealed for 15 min at 720°C. In Fig. 3.2 (a) the sample with InGaAsN barriers has 3 QWs of 6 nm thickness, the one with GaAs barriers has 6 QWs of 6 nm thickness. The composition of the InGaAsN-barrier is 2.1% N and 4.8% In (the barriers are grown almost lattice-matched to GaAs, so that the strain in the QWs is approximately the same for the two samples). In Fig. 3.2 (b) the results for two samples with 8 and 6 QWs of thickness 4 and 6 nm (the total thickness of InGaAsN was kept almost constant) are shown.

Influence of the barrier material

From Fig. 3.2 (a), one can see that the QW-quality of the sample having InGaAsN barriers is better than the one having GaAs barriers:

- there is a clear excitonic enhancement in the sample having InGaAsN barriers;
- the QW-absorption edge (Eq. 3.1) in sharper for the sample having InGaAsN barriers. This is probably due to the fact that the N-diffusion from the QW is prevented (see Section 3.4) in the case of N-containing barriers;

Laser data confirm these results: lasers having InGaAsN barriers have lower threshold current densities than the ones with GaAs barriers.

Influence of the QW-thickness

From Fig. 3.2 (b), one can see that the 4 nm - QWs have a higher quality (even if the N-content is higher) than the 6 nm - QWs (excitonic enhancement and sharper QW-absorption edge). However, due to the small QW-thickness, the absorption edge is blue-shifted by circa 50 meV. By using 4 nm-thick quantum wells and N-content up to 2%, it is impossible to reach emission at 1.3 µm.

3.1.3. Influence of In- and N-content on optical absorption of InGaAsN quantum wells

To see the influence of the N- and In- content on the optical absorption of the InGaAsN QWs, series with varying N and In content were studied. The results are represented in Fig. 3.3. All the samples were annealed for 15 min at 720°C.

The N-series of samples

Fig. 3.3 (a) shows clearly, by using the same criteria for QW-quality like before (excitonic enhancement and sharpness of the QW-absorption edge), that the quality of the quantum wells decreases by increasing the N-content. In order to obtain high-quality samples, N compositions between 1.5 and 1.7% must be used.

The In-series of samples

From Fig. 3.3 (b) one can see that the quality of the quantum wells decreases by increasing the In-content between 10 and 30%. The GaAsN sample has a blunter absorption edge than the sample with 30% In. This can have two causes:

- the GaAsN quantum well is of type I (like the other three samples), but the quality of this sample is the lowest;

- ♦ the GaAsN quantum well is of type II. In this case it is expected, as discussed in Chapter 4, that the absorption edge is blunter than in the case of a type I quantum well;

To reach 1.3 µm emission from InGaAsN QWs having 1.5 - 1.7% N and a thickness of 6 - 7 nm, the In-content must be above 30%.

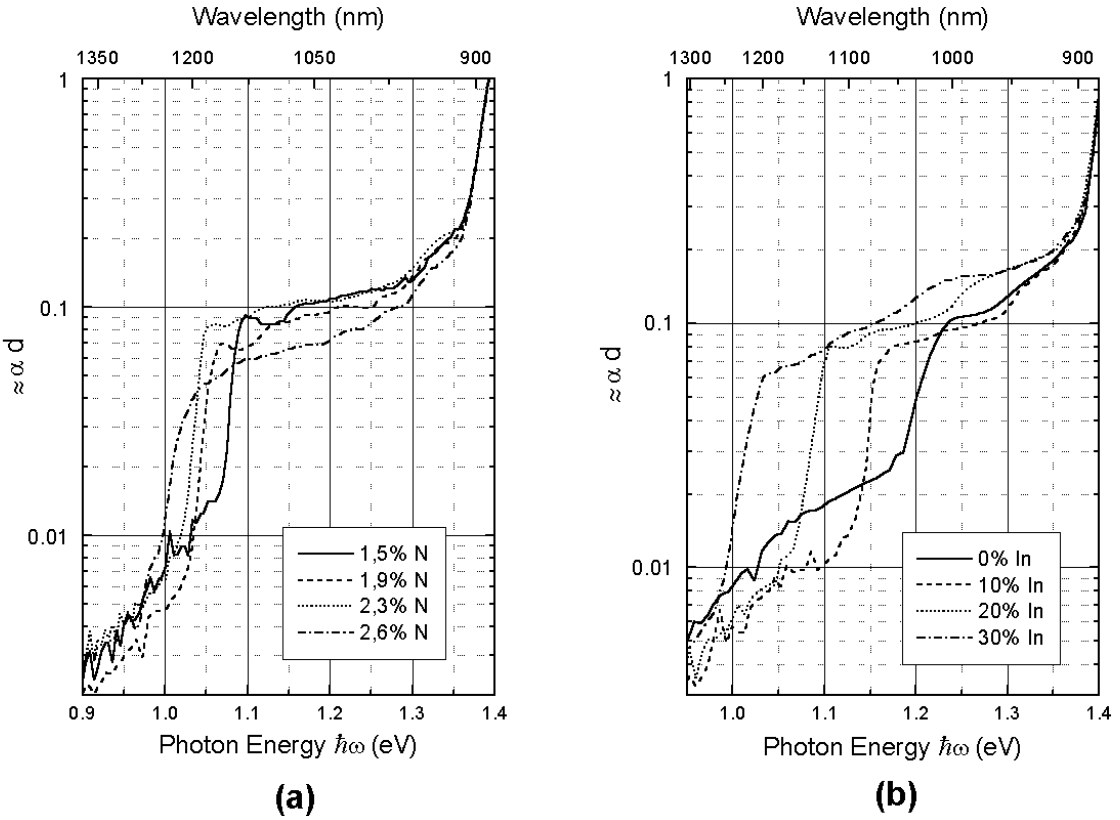

Fig. 3.3: Absorption of similar, annealed InGaAsN QW-samples having **(a)** different N composition (8 QWs of 4 nm thickness, 35% In) and **(b)** different In composition (5 QWs of 6 nm thickness, 1.5% N).

3.1.4. Summary

Due to the dispersion of different parameters of the samples (size, thickness, smoothness of the back-surface) and due to the influence of the substrate and barrier, no absolute measurements of the absorption coefficient in quantum wells were possible. By taking criteria of the QW-quality, which are independent of the absolute precision of the measurements (sharpness of the QW-absorption edge, structure in the absorption spectrum), a comparison of the quality of different quantum wells is nevertheless possible.

The results of these absorption measurement were used to find the most promising range in the wide field of QW-parameters (thickness, composition, barrier material)[10]. Based on absorption measurements, the QW thickness and composition, barrier material, and annealing parameters were optimized. For emission around 1.3 µm, the optimum thickness was found to be 6 - 7 nm, for N-compositions 1.5 - 1.7% and In-composition 32 - 36%. Quantum wells having InGaAsN barriers show a higher quality than the ones having GaAs barriers. The optimum annealing parameters are 700 - 720°C for 10 - 15 min: samples annealed for 2 hours do not show better quality than the ones annealed for 15 minutes.

3.2. Properties of photoluminescence in InGaAsN quantum well samples grown by molecular beam epitaxy

In this section the typical features of the photoluminescence in InGaAsN QW-samples are discussed. In the rest of the chapter, the attention is concentrated on the photoluminescence from the InGaAsN quantum wells.

3.2.1. The photoluminescence spectrum of InGaAsN quantum well samples

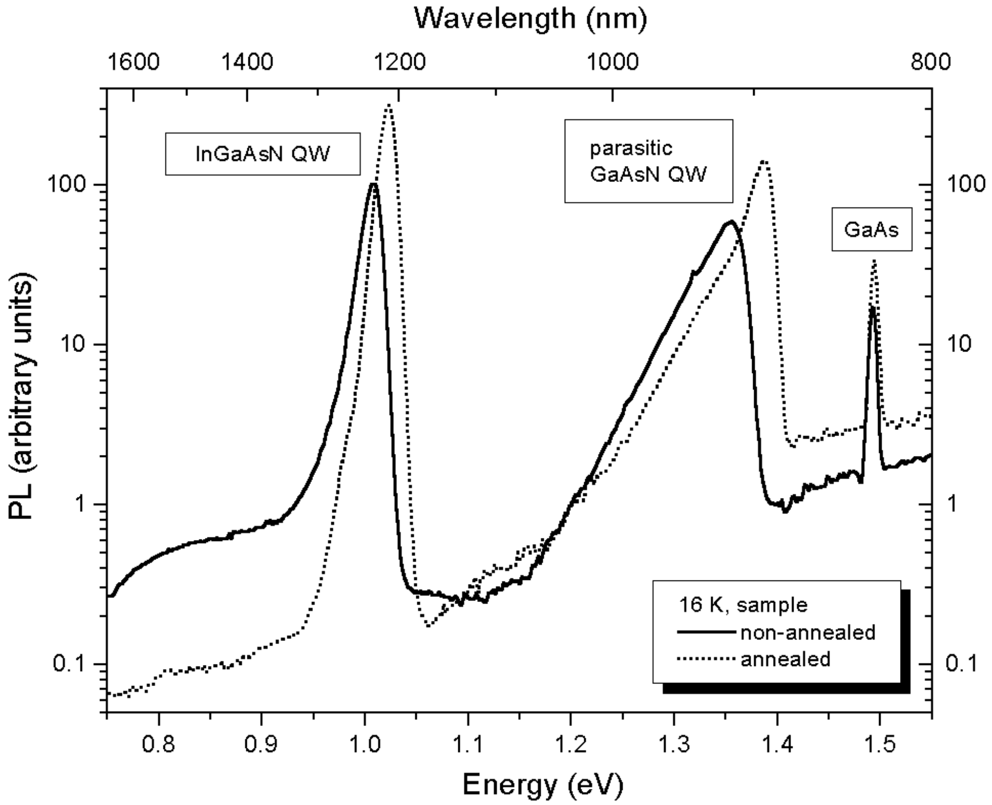

Fig. 3.4: The typical PL spectrum of an InGaAsN QW-sample. One can see photoluminescence coming from the QWs and barriers. The marked peak is unexpected. On the picture, the as-grown and thermally annealed samples are shown.

In Fig. 3.4, the photoluminescence spectrum of a typical InGaAsN QW-sample is shown. Three peaks are visible in the spectrum (starting from low to high energies):

- the photoluminescence from the quantum well. This photoluminescence will be discussed in detail in the other sections of this chapter;

- a strong photoluminescence peak centered around 1.35 - 1.4 eV, seen only in N-containing samples. The origin of this peak was not initially known. It disappears at temperatures above 100 K. At low temperatures, its strength (i.e. the integrated PL) is comparable with the strength of the InGaAsN QW-peak. The energy-position of the peak is blue-shifted after thermal annealing, like in the case of the InGaAsN QW-peak, which suggests that this peak comes from a N-containing region of the sample; its strength suggests also that it comes from a quantum well (compare with the much weaker photoluminescence from the barriers);

- the photoluminescence from the GaAs-barriers. This peak is narrow and weak, compared with the PL-peak coming from the InGaAsN quantum wells. This suggests that the photo-excited electron-hole pairs, which are generated in the barriers, are captured in the quantum wells in a time relatively short compared to the photoluminescence lifetime. Indeed, it is known that this time is in the range of tens of ps[70];

The origin of the parasitic peak is demonstrated next.

3.2.2 The z-dependence of the N-composition in MBE-grown samples

The actual spatial distribution of the nitrogen composition along the grown region plays an important role for the optical sample quality, due to the following reasons:

- it is known that the GaAsN material has a low PL-efficiency at room temperature (the cause in unclear). Inclusion of nitrogen in barriers could negatively influence the optical properties of the sample (lasers);

- uncontrolled inhomogeneity in the N-distribution of the grown region could introduce unwanted quantum wells and reduce the PL-efficiency of the InGaAsN quantum wells;

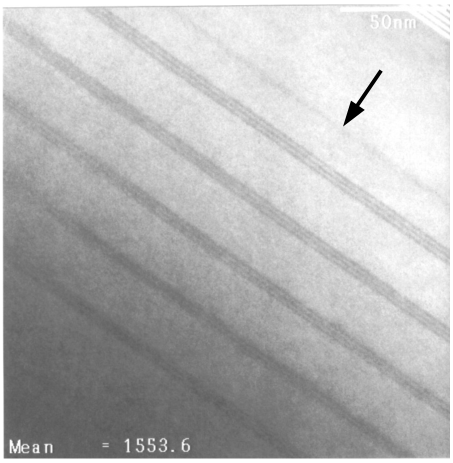

Fig. 3.5: TEM image of a sample, containing five 6.2 nm-thick GaAsN-QWs. The arrow indicates the direction of growth as well as a structure similar to a quantum well, with a thickness of 2 - 3 nm. Its spatial position coincides with the N-plasma ignition [C. Vanuffel, LETI Grenoble, unpublished].

Unfortunately, both of these phenomena appear during the growth process of N-containing QW-structures. The barriers contain nitrogen, as explained in Chapter 2 (Fig. 2.1 and 2.2). Transmission Electron Microscopy (TEM) images show a parasitic quantum well formed before the growth of the InGaAsN quantum wells, as indicated by the arrow in Fig. 3.5. The spatial position of this peak coincides with the moment of N-source plasma ignition.

The presence of this quantum well seen in TEM images suggest that the parasitic PL-peak from Fig. 3.4 comes exactly from this quantum well. To study if this is indeed the case, a test sample was grown, in which about 50 nm barrier-material was grown between the plasma ignition moment and the (single) InGaAsN quantum well. The sample also contains AlGaAs barriers, as indicated in Fig. 2.2. This sample was etched down in steps and the photoluminescence was measured. The results are presented in Fig. 3.6.

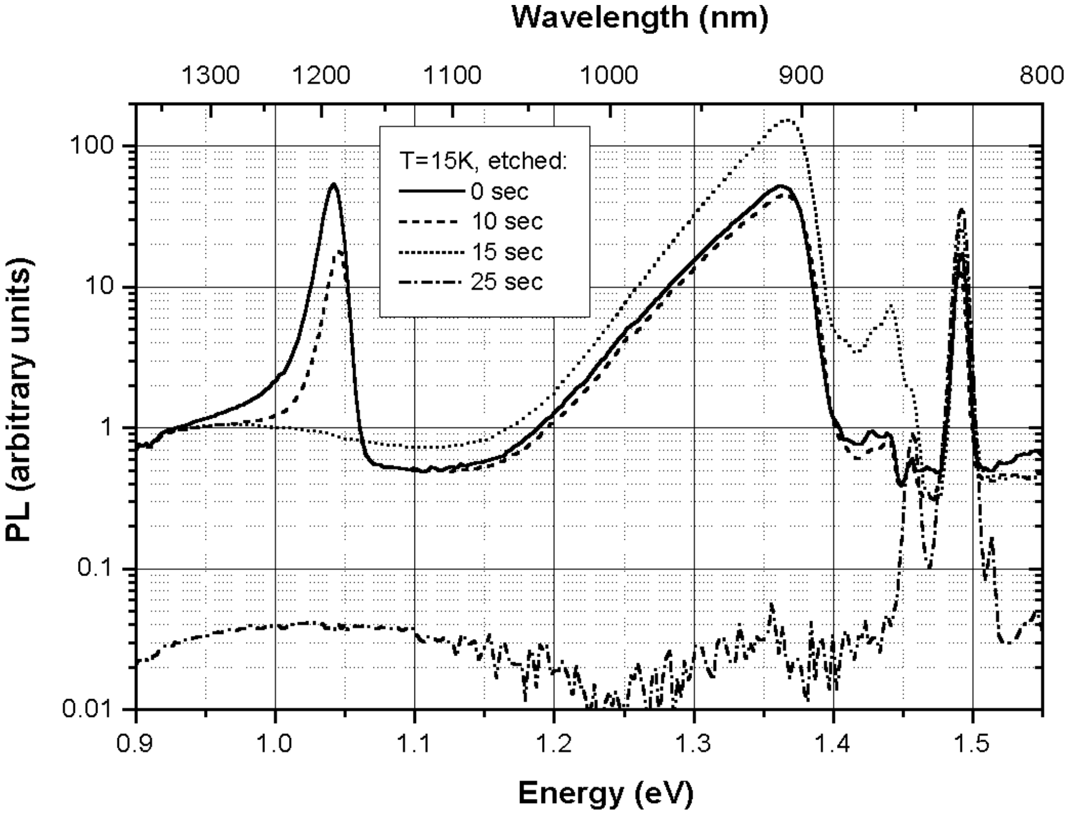

Fig. 3.6: PL experiment, which demonstrates that the unexpected peak seen in Fig. 3.4 comes from the parasitic QW indicated in Fig. 3.5, produced by the N-plasma ignition process.

The curve “0 sec” in Fig. 3.6 is taken for the non-etched sample, the other curves are measured after etching the samples for the indicated time. After:

- 10 seconds, the InGaAsN-QW is not etched yet. The AlGaAs barrier from the surface-side was etched and the InGaAsN-QW lies near the surface: this is the reason why the PL-intensity from the InGaAsN-QW decreases by about a factor of three;

- 15 seconds, the InGaAsN-QW has been etched off. One can see a much stronger parasitic PL-peak: that is, by eliminating the InGaAsN-QW, the intensity of the parasitic PL-peak becomes stronger. The reverse is also expected to be true, i.e. the presence parasitic PL-peak reduces the intensity of the photoluminescence from the InGaAsN-QW. There is another PL-peak around 1.44 eV, which probably comes from the N-containing GaAs barriers not yet etched;

- 25 seconds, the whole N-containing region was etched off. The parasitic PL-peak has disappeared. The PL-background up to 1.4 eV decreases in intensity by a factor of 20, which indicates that there is an important sub-band gap photoluminescence coming probably from the N-containing GaAs barriers;

Based on this discussion, it is concluded that the parasitic PL-peak is associated with a quantum well formed when the N-plasma ignition takes place. After this discussion, the structure of the sample depicted in Fig. 2.2 was demonstrated.

3.2.3. General properties of the photoluminescence in InGaAsN quantum wells

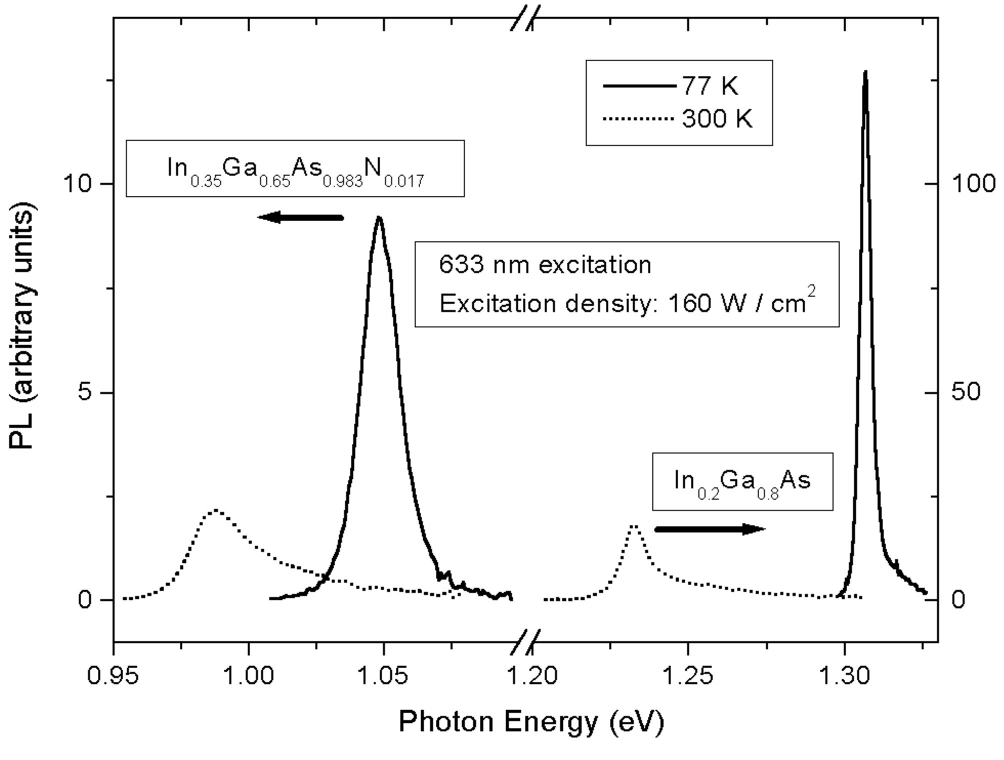

Fig. 3.7: Photoluminescence spectra of InGaAsN and InGaAs single-QW high-quality samples, taken at 77 and 300 K.

In this paragraph, the essential features of the PL properties in InGaAsN-QWs are discussed. For comparison, samples without N (InGaAs QWs) are used. Typical PL spectra of InGaAs and InGaAsN QW-samples, taken at 300 and 77 K, are shown in Fig. 3.7. The samples measured were taken from the same wafers from which high-quality lasers were prepared (low threshold current). The PL full width at half maximum (FWHM), the PL-peak energy position, the PL-peak maximum and the integrated PL of these state-of-the-art samples are shown in Table 3.1.

Table. 3.1. Some of the PL-spectra parameters of the samples shown in Fig. 3.7.

	77 K				300 K			
	FWHM (meV)	Peak at (meV)	PL max.	PL integrated	FWHM (meV)	Peak at (meV)	PL max.	PL integrated
InGaAs	**4**	1307	127	**0.7**	**10**	1233	18	**0.38**
InGaAsN	**17**	1048	9	**0.19**	**30**	987	2	**0.09**

The homogeneous broadening of the PL-peak is *estimated* at 77 K, under the assumption of excitonic photoluminescence. This assumption is justified: in Chapter 4, photovoltage spectra of the same samples are shown, which prove an important excitonic contribution in the absorption, at 77 K (especially for the InGaAs-sample). From the energy-time uncertainty relation, $\Delta E \approx \frac{\hbar}{\tau}$, where τ is the excitonic lifetime. Taking for τ a value of 100 ps (see the last section of this chapter), a value of about 10 μeV results for the homogeneous broadening in energy. This value is much smaller than the FWHM-value of the PL-peak for the InGaAs quantum well, at 77 K (4 meV). This comparison shows that most of the broadening of the PL-peak has inhomogeneous origin, both for the InGaAs and InGaAsN quantum wells.

From Table 3.1, one can see that the FWHM of PL-peak is much larger[28] (four times) for the InGaAsN QW than for the InGaAs QW. This shows that the inhomogeneous broadening has a higher value in the InGaAsN quantum well. The integrated PL of the InGaAsN sample is one fourth as compared to the InGaAs sample, an indication for a lower optical quality of InGaAsN QWs. Due to the higher value of the PL-peak FWHM in InGaAsN QW-samples, the PL-peak maximum is much smaller for InGaAsN as compared to InGaAs QW-samples.

Note that due to the presence of nitrogen and the higher In-content, the PL-peak position from the InGaAsN-QW is strongly red-shifted as compared to InGaAs-QW. From 77 K to 300 K, the PL-peak position shifts 74.1 and 61.3 meV for the InGaAs and InGaAsN sample, respectively. This value is around 100 meV for GaAs. As seen further, this shift is a measure for the degree of in-plane QW-potential fluctuations (see sections 3.3 and 3.4).

All the values given in Table 3.1 depend on the excitation density. For this particular case, the integrated PL decreases by a factor of two between 77 and 300 K. This factor, which depends strongly on the excitation density (decreases with increasing excitation density), is higher for InGaAsN QW-samples of lower quality. The fact that for the case of the samples studied in Fig. 3.7 this ratio is about two, for a low excitation density, confirms the high-quality of these samples. The PL-properties of these two samples can be compared with test samples studied in the next section, and which have a lower quality (they were grown at the beginning of this work).

3.2.4. The low-energy tail in the photoluminescence of InGaAsN quantum wells

Depending on the growth conditions and QW-parameters, some InGaAsN QW-samples show an important low-energy (under the effective band gap of the quantum well) photoluminescence. An example is shown in Fig. 3.8.

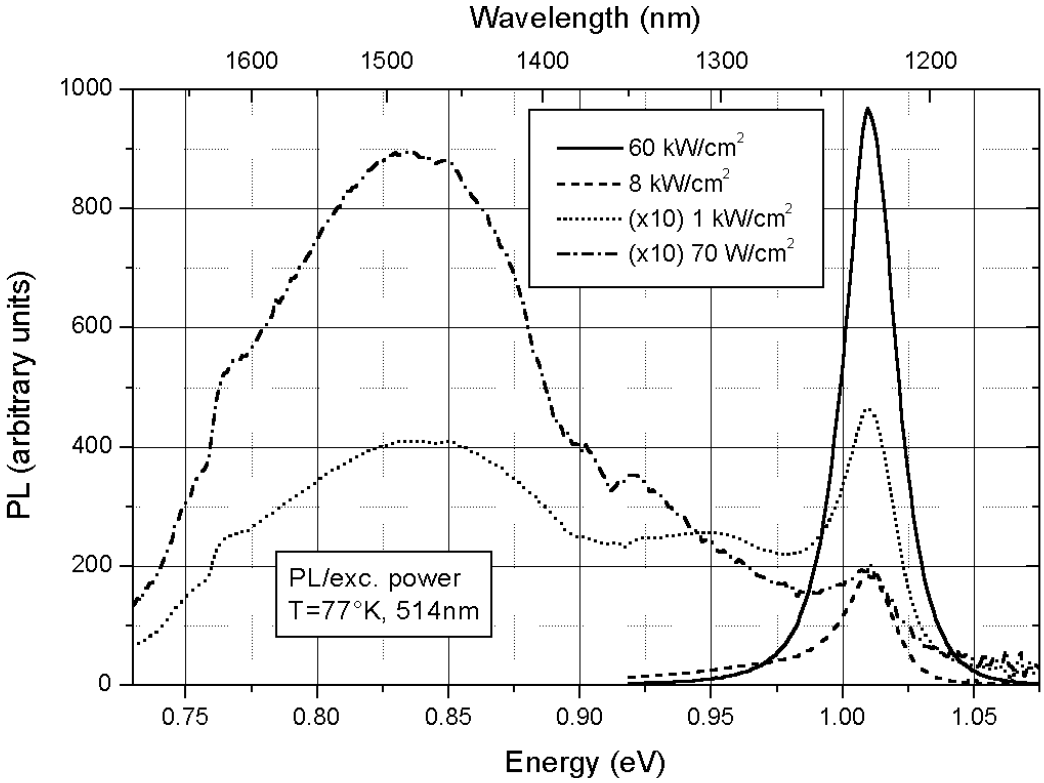

Fig. 3.8: The low-energy tail in the PL-spectrum of an InGaAsN QW-sample, which can be seen clearly at low excitation densities and only at low temperatures (under 100 K). This sample has five $In_{0.35}Ga_{0.65}As_{0.983}N_{0.017}$ quantum wells of 10 nm thickness.

In the following section, the influence of different QW-parameters and thermal annealing on the low-energy PL-tail is studied.

3.3. Influence of quantum well parameters, thermal annealing and growth temperature on photoluminescence properties of InGaAsN quantum wells

The motivation of the photoluminescence (PL) studies carried out in this paragraph is to optimize the QW-parameters (N and In content, QW-thickness) and growth temperature, in order to obtain an optimum for the PL-quality (high intensity, small inhomogeneous broadening of the PL-peak). The influence of the thermal annealing on the PL-properties of the samples is studied as well. Based on the PL-studies performed in this section, a model for the PL-mechanism in InGaAsN QWs is proposed in the next section (§3.4), which includes the observed effects of the thermal annealing. This model is supported by TEM-studies.

In this section two series of three samples, with different N- and In-content, are studied. The first series (the N-series) contains 3 QWs of 6.2 nm thickness, with a N-content of 1.1, 1.7, and 2.3% and an In-content of 35%. The second series (In-series) has 5 QWs of 7 nm thickness, with an In-content of 30, 35, and 40% and a N-content of 1.7%. Additionally, in order to see the influence of the QW-thickness on the PL-properties, the In-series contains also a sample having 10 nm QW-thickness and 1.7% N-, 35% In-content. The PL was measured at 77 and 300 K, for excitation densities (514 nm) between 100 and 50 kW/cm^2. All samples were annealed at 720°C for 10 minutes and measured at low (77 K) and room temperature (300 K).

3.3.1. Influence of quantum well parameters and thermal annealing on the low-energy tail of the photoluminescence

The purpose of the measurements performed in this subsection is to see, how the low-energy PL (discussed in §3.2.4) is related to the quality of the photoluminescence in InGaAsN quantum wells.

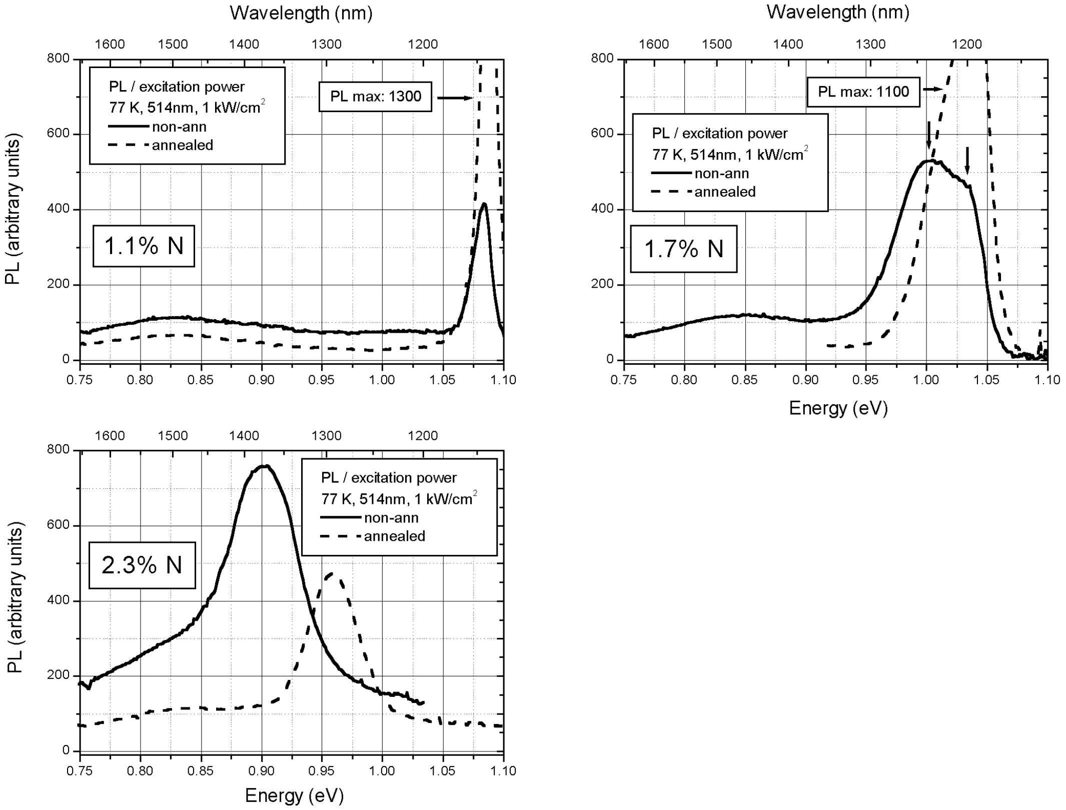

Fig. 3.9: The low-energy PL tail for the samples in the N-series. The QWs contain 35% In.

The low-energy PL tail for the N-series and In-series are shown in Fig. 3.9 and 3.10, respectively. There is generally a reduction of the low-energy PL tail after thermal annealing. The measurements were performed for low excitation densities.

The N-series of samples

For the N-series of samples (Fig. 3.9), there is a clear correlation between the N-content, low-energy PL, and the intensity of the PL-peak. With increasing N-content, the low-energy PL increases and the intensity of the PL-peak decreases.

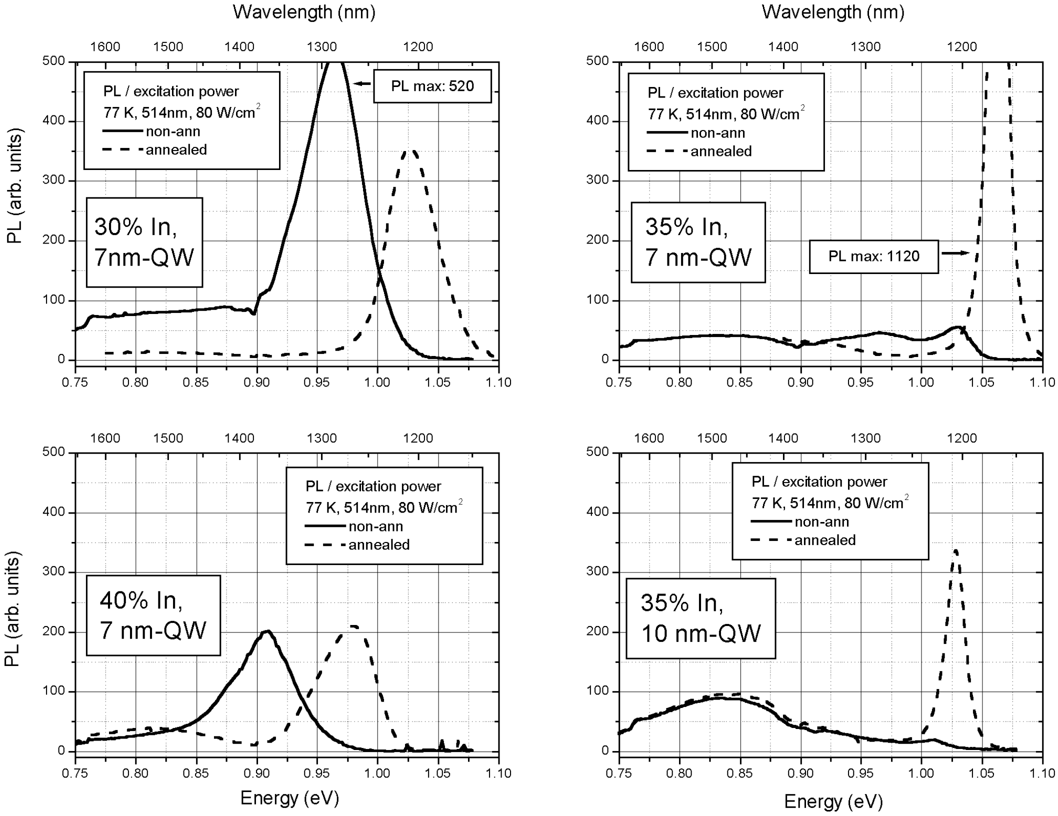

Fig. 3.10: The low-energy PL tail for the samples in the In-series (7 and 10 nm QW-thickness). The N-content is 1.7%.

The In-series of samples

For the In-series of samples (Fig. 3.10) with the same thickness, there is no clear correlation between the In-content, low-energy PL, and the intensity of the PL-peak. For the non-annealed samples, the low-energy PL decreases with increasing In-content. After thermal annealing, this tendency is reversed: the sample having 35% In has the best PL-quality (narrow peak, high intensity) but in the same time the low-energy PL has the same intensity as in the sample with 40% In.

Influence of the QW-thickness

Comparing the two samples on the right hand-side in Fig. 3.10, which have quantum wells of thickness 7 and 10 nm, one can see that the sample which has thick QWs has a high intensity of the low-energy PL and which is not reduced after thermal annealing. This sample has also lower PL-quality, which suggests that the critical thickness might have been reached for these quantum wells.

Note that the samples in Fig. 3.9 and 3.10, which contain 1.7% N and 35% In and have thin (6 and 7 nm) QWs, show a double-peak structure in the PL spectra before thermal annealing. This double-peak structure disappears after thermal annealing.

With the exception of the 10 nm QW-sample, one can see that a high low-energy PL occurs when the composition *ratio* N/In (in percent) is larger than about 1.7/35. In this case the PL-spectra have an abnormal feature: the main PL-peak is larger before than after thermal annealing, for this (low) excitation density;

Conclusions

The PL-spectra in the Fig. 3.9 and 3.10 show that the low-energy PL depends on N- and In-compositions as well as on QW-thickness. A too high N/In composition ratio and a too large QW thickness lead to an increase in the intensity of the low-energy tail and a simultaneous decrease of the PL-intensity. There is not a clear correlation between the low-energy PL-tail and the PL-quality of the sample: the sample in Fig. 3.10 which has 35% In and 1.7% N shows a low-energy PL-tail even after thermal annealing, but it has at the same time the best PL-quality. However, with increasing N-content of the QWs, the low-energy PL-tail increases in intensity.

3.3.2. Influence of the quantum well N-content and In-content on the photoluminescence properties. Influence of thermal annealing

In Appendix C, Table 1, different parameters of the PL spectra are indicated. The excitation power was chosen at intermediate values, around 70 mW (1 mW of excitation power corresponds to 80 W/cm^2 excitation density): not too low in order to have a good PL signal and not too high in order to avoid PL saturation. Some of the data from the table is plotted in Fig. 3.11 (from left to right): the maximum value of the PL-peak, the PL-peak energy position and FWHM, the PL-shift with excitation power (between 100 W/cm^2 and 50 kW/cm^2), the blue shift of the PL-peak after thermal annealing, and the temperature-shift of the PL-peak between 77 and 300 K.

The meaning of the different PL-parameters plotted in Fig. 3.11

a) *the PL-peak maximum intensity:* it is a direct measure of the PL-quality;

b) *the PL-energy position* includes two important information: (a) the band gap energy as a function of N- and In-content and (b) a possible decrease of the PL emission energy due to disorder (emission from carriers localized in potential minima);

c) *PL-peak FWHM-value* and *PL-shift with excitation power:* gives a direct measure of the inhomogeneity of the quantum wells. In some cases, the PL-shift with excitation power has a negative value: this is due either to the heating of the sample (and the consequent reduction of the band gap) or to many-body effects (reduction of the PL-emission energy due to Coulomb interaction between the photoexcited electrons and holes). The FWHM-value of the PL-peak is always reduced after thermal annealing, which indicates a better homogeneity of the quantum wells;

d) *PL-blue shift after thermal annealing:* gives a measure of the structural changes which take place in the quantum wells after thermal annealing;

e) *Temperature-shift of the PL-peak between 77 and 300 K:* if the samples were homogeneous, the PL-peak shift with the temperature would be given by the Varshni law, which expresses the reduction of the band gap with increasing temperature. For the InGaAsN QW with PL emission around 1 eV, the reduction of the band gap between 77 and 300 K is around 70 meV. As the experiments show (see Fig. 3.11), for some of the InGaAsN QW-samples the temperature-shift has a much smaller value. The model presented in the next section explains this anomaly, which is again a measure of the inhomogeneity of the quantum wells.

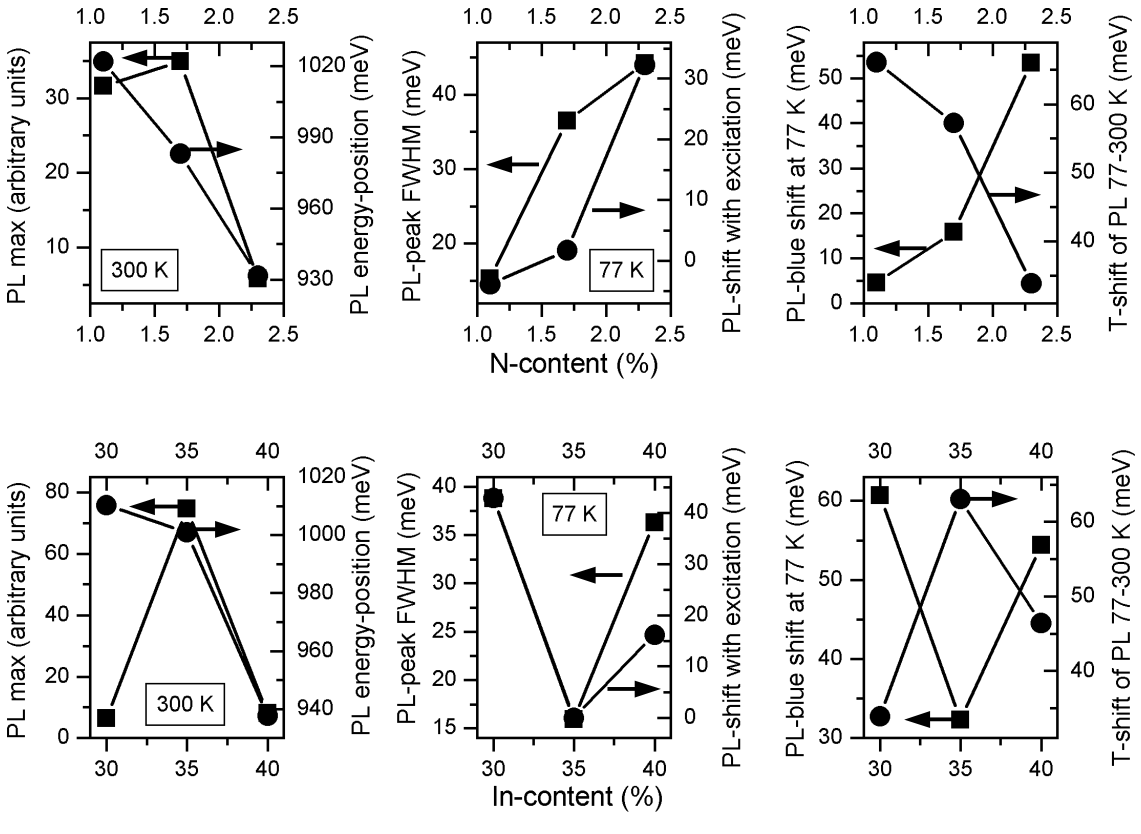

Fig. 3.11: Different PL-parameters of samples with different N and In content. Six parameters are plotted for each series of samples, in arbitrary units or meV. In the upper (lower) part of the figure, the N-(In-)series of samples are plotted. All the samples are annealed. For each plot, the left (right) *y*-axis corresponds to squares (circles). The N-series of samples has three QWs of 6 nm thickness, with 35% In. The In-series of samples has 5 QWs of 7 nm thickness, with 1.7% N. The PL-shift with excitation power is measured between low (100 W/cm^2) and high (50 kW/cm^2) excitation densities.

The N-series of samples

With the exception of the PL-peak maximum intensity, the parameters plotted in Fig. 3.11 have a monotonous variation with the N-content of the samples. Based on the discussion about the meaning of different PL-parameters, this means that: (a) there is an optimum of the PL-intensity for a N-content of 1.7%, (b) the homogeneity of the samples decreases with increasing N-content, and (c) the changes which take place in the samples after thermal annealing increase with increasing N-content.

In the same time (see line 6 of Table 1 in Appendix C), the ratio between the integrated-PL measured at 77 and 300 K increases with increasing N-content. This shows that the importance of non-radiative recombination at high temperatures increases with increasing N-content.

The In-series of samples

With the exception of the PL-peak energy-position, the plotted parameters have extreme values for 35% In. Based on the discussion about the meaning of different PL-parameters, this means that: (a) there is an optimum of the PL-intensity for an In-content of 35%, (b) the homogeneity of the samples has a maximum value for an In-content of 35%, and (c) the changes which take place in the samples after thermal annealing are minimal for the quantum wells which contain 35% In.

Conclusions

For the In-series of sample, the results are very clear: there is an optimum in the PL-quality and in the homogeneity of the quantum wells for 35% In-content.

For the N-series of samples, the homogeneity of the samples decreases with increasing N-content. The PL-intensity at room temperature has a maximum for 1.7% N-content. The importance of non-radiative recombination at high temperatures increases with increasing N-content.

3.3.3. Influence of quantum well thickness on the photoluminescence of InGaAsN quantum wells

By comparing the PL-data for the samples from the In-series, which have 7 and 10 nm QW-thickness (see Table 1 in Appendix C) and the same (1.7% N and 35% In) QW-composition, the following conclusions can be drawn:

- *the PL-peak maximum and the integrated PL* is much lower (3 - 4 times less) for the 10 nm-QWs as compared to 7 nm-QWs;
- before annealing, *the FWHM*-value *of the PL-peak* is less for the 10 nm QWs. This suggests that the QW-interface roughness has an important contribution to the inhomogeneous broadening in as-grown samples. However, after annealing the situation changes;
- *the blue shift after annealing* for the 10 nm QWs is half of that for the 7 nm QWs. This indicates that, for the same QW-composition, the annealing has more effect on the 7 nm-QWs as compared to the 10 nm-QWs;
- *the PL-shift with temperature* between 77 and 300 K and is roughly the same for 7 and 10 nm QWs. This indicates the same degree of in-plane potential fluctuations for the two values of the QW-thickness (see the model in §3.4);

The lower PL-intensity and the strong low-energy tail in the spectra of the 10 nm QW sample suggest that the critical (strain-conditioned) thickness has been exceeded.

3.3.4. Influence of growth temperature on the photoluminescence of InGaAsN quantum wells

The growth temperature of InGaAsN quantum wells has a direct effect on the degree of carrier localization, due to the instability of the InGaAsN alloy during growth. The effect of carrier localization on the PL-properties of InGaAsN QW-samples is discussed in detail in Section 3.5.

3.4. Model for the photoluminescence mechanism in InGaAsN quantum wells. The effect of thermal annealing

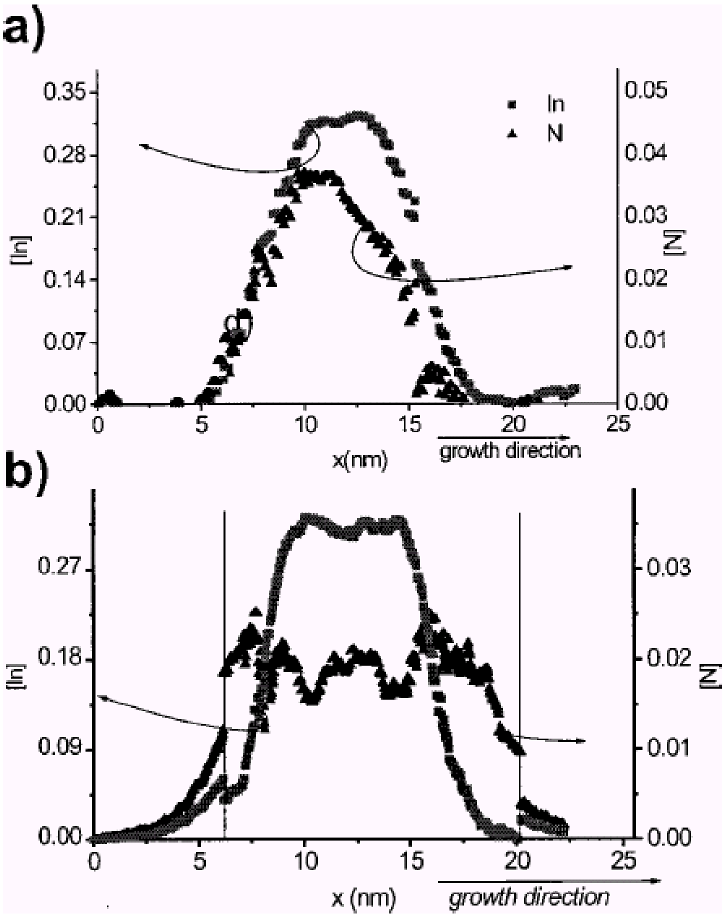

Fig. 3.12: The In- and N-profiles in the direction of growth before **(a)** and after thermal annealing **(b)** (from reference [22]). The profiles change after thermal annealing. The out-diffusion of the nitrogen from the QW explains the blue shift of the PL-peak after annealing.

In this section a model is proposed, which explains many of the PL-properties of InGaAsN quantum wells observed in the previous section. TEM-images support this model and bring further information about the changes that take place after thermal annealing in InGaAsN quantum wells.

3.4.1. The effect of thermal annealing on quantum well potential

TEM studies were performed in order to find what influence the thermal annealing has on the structural properties of InGaAsN QWs. In Fig. 3.12, such studies indicate a change in the N- and In-profiles across the quantum well after thermal annealing. The N- and In-profiles are calculated from the simultaneous measurement of: (a) the tetragonal lattice distortion of the unit cell from high-resolution micrographs and (b) the intensity of the chemically sensitive (002) reflection from dark field images[21]. The In-profile becomes better defined; the N-profile becomes more extended, i.e. the nitrogen diffuses out of the quantum well. The diffusion of nitrogen out of the quantum wells explains (at least a part of the) the blue shift of the PL-peak after thermal annealing. However, such a model cannot explain other PL-properties of InGaAsN QWs, for example the small shift of the PL-peak between 77 and 300 K.

3.4.2. In-plane quantum well potential fluctuations

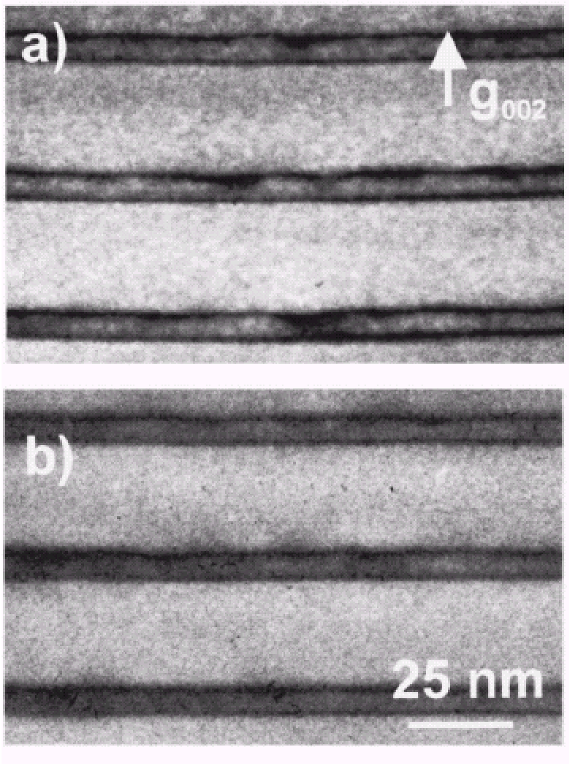

Fig. 3.13: Dark-field TEM-images before **(a)** and after thermal annealing **(b)**, which show contrast-fluctuations on a length-scale of 20 nm (from reference [22]). The homogenization of the contrast in the annealed quantum wells indicates a homogenization of In-concentration.

TEM studies, shown in Fig. 3.13 demonstrate that changes take place during the annealing process not only across, but also along the QWs. Dark-field TEM-images show a homogenization of the contrast after thermal annealing, which indicates a homogenization of the In-concentration in the plane of the QW.

A calculation from the TEM-images of the In-concentration along the QW-plane is presented in Fig. 3.14. Strong fluctuations of the In-concentration, on a length scale of 20 nm, are present before thermal annealing; they are reduced after thermal annealing.

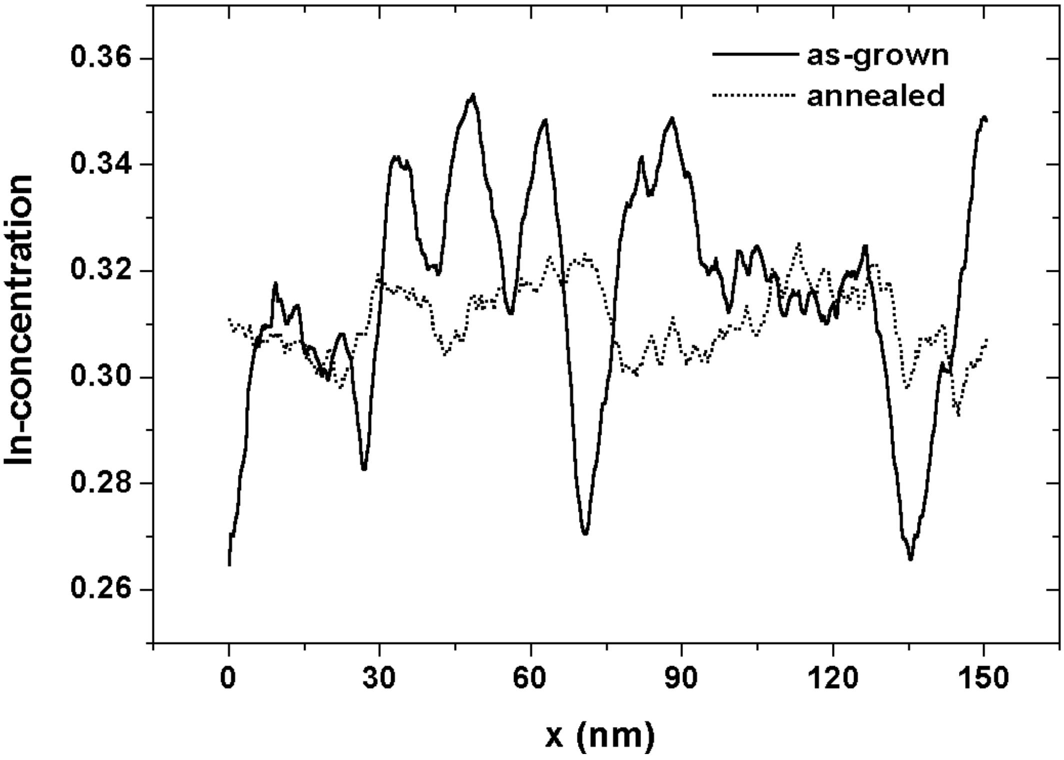

Fig. 3.14: The in-plane In-concentration, before and after annealing, as extracted from TEM images.

The potential fluctuations in the plane of the quantum well, which are reduced after thermal annealing, account for many of the PL-properties observed in the previous section. As indicated in Fig. 3.15, such a model can explain: (a) the blue shift after thermal annealing, (b) a smaller temperature-shift of the PL-peak as expected from the reduction of the band gap, and (c) the reduction of the FWHM of the PL-peak after thermal annealing (by reduction of inhomogeneous broadening). The small temperature-shift of the PL-peak in samples with strong potential fluctuations is explained by the compensation of the band gap reduction with increasing temperature through the thermal redistribution of the carriers in the potential fluctuations (localized states have a small density of states): the weight-center of the electron (hole) energy-distribution moves fast to higher (lower) energies as the temperature increases.

It is not obvious from the Fig. 3.15 why the PL-intensity is small in some samples. But let's remember the conclusion of §3.3.2: the N-series of samples show increasing rates of non-radiative recombination with increasing N-content (it appears that the nitrogen itself introduces non-radiative channels), while in the In-series of samples a small value of the PL-intensity is associated with a low homogeneity of the quantum wells. This fact suggest that strong potential fluctuations and the consequent carrier localization, besides the non-radiative channels introduced by the presence of nitrogen, might be the cause of low PL-intensity in inhomogeneous quantum wells. The effect of carrier localization on the PL-properties of InGaAsN quantum wells is studied in detail in the next section.

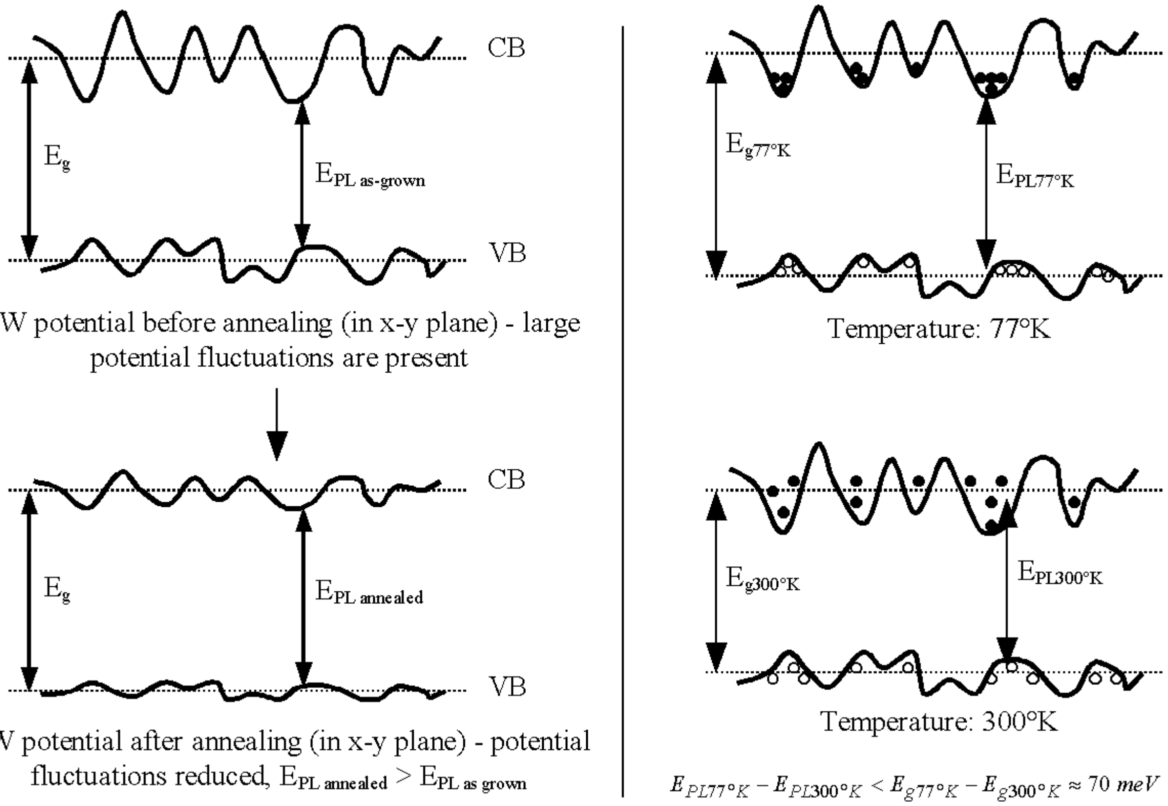

Fig. 3.15: A simple model, which explains the PL-properties of InGaAsN quantum wells. The model explains the blue shift of the PL-peak after thermal annealing by the homogenization of in-plane potential fluctuations. The small temperature-shift of the PL-peak is explained as well by in-plane potential fluctuations in the quantum well.

3.5. Carrier localization effects in InGaAsN quantum wells

As mentioned at the end of the last section, it was experimentally observed that low homogeneity of InGaAsN QWs is associated with low PL-intensity. This relation is studied in detail in this and the next sections. In inhomogenous samples, the carriers are localized in potential minima, so that the sample inhomogeneity is associated with carrier localization.

Usually in semiconductors, the variation of the variation of the band gap follows the empirical Varshni law[29]. It was experimentally observed, that the PL-peak temperature-dependence of the InGaAsN quantum wells show the so-called S-shape. Grenouillet[30] *et al.* and Pinault[31] *et al.* discuss the S-shape, and explain it by carrier localization at low temperatures. The S-shape does not appear for the case of InGaAs quantum wells, and is less pronounced in GaAsN quantum wells.

The temperature dependence for one of the samples studied further in this chapter is shown in Fig. 3.16; the experimental temperature-dependence of the PL-peak is fitted in Fig. 3.16 with the Varshni law in the high temperature range. In the experimental curve, one can see a sudden change (by about 30 meV), in the temperature-dependence of the PL-peak around 80 K. *This sudden change in the PL-peak energy is interpreted in the following as a measure of the localization energy of carriers in QW, and will be denoted as "localization energy".*

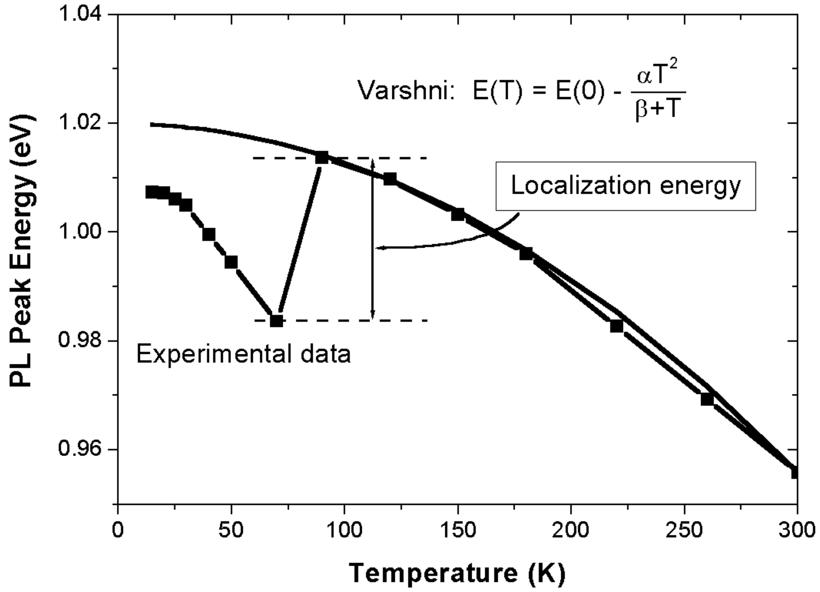

Fig. 3.16: The S-shape in the dependence with temperature of the PL-peak position in InGaAsN quantum wells. The continuous line gives the theoretical variation of the band-gap with the temperature (Varshni law).

In this section, the relation between the growth temperature and the degree of carrier localization is studied first. Then the influence of thermal annealing on the degree of carrier localization is discussed. In an effort of finding out the cause of low PL-intensity in inhomogeneous samples, this is followed by a discussion about the temperature-dependence of the integrated PL-intensity. Finally, an explanation of how the carrier localization influences the PL-intensity is given.

3.5.1. The correlation between the sample growth temperature and the degree of carrier localization

To see the influence of the growth temperature - which is one of the most important growth-process parameters - on the PL emission, a series of six samples were grown at different temperatures: 415, 423, 432, 446, 453 and 467°C. The parameters of these samples have been optimized for PL-emission around 1.3 µm: all of them contain 26% In and 1.8% N (intentional compositions), the thickness of the quantum wells is 9.2 nm. In more detail: besides the single 9.2 nm QW ($In_{0.26}Ga_{0.74}As_{0.982}N_{0.018}$) the samples contain two 200 nm-thick GaAs barriers and two optical confinement layers consisting of 6 periods of 2.5 nm-GaAs/2.5 nm-AlAs. The structure was grown at 600°C except the QW, which was grown at lower temperatures, between 415 and 467°C. All samples contain one QW. The thermal annealing was performed at 720°C for 30 minutes.

In Fig. 3.17 the temperature dependence is plotted for five samples grown at different temperatures. The S-shape is present for all samples except the last one, becomes more accentuated and moves at higher temperature as the growth temperature is increased. The 453°C-grown sample probably shows the S-shape at temperatures higher than 300 K, but there is a similar, smaller structure around 100 K in the temperature dependence. The sudden change of the PL-peak position associated with the S-shape, and interpreted as the localization energy of the carriers, is small (6 meV) for the 415°C-grown sample and much larger (≈30 meV) for the 432°C-grown sample.

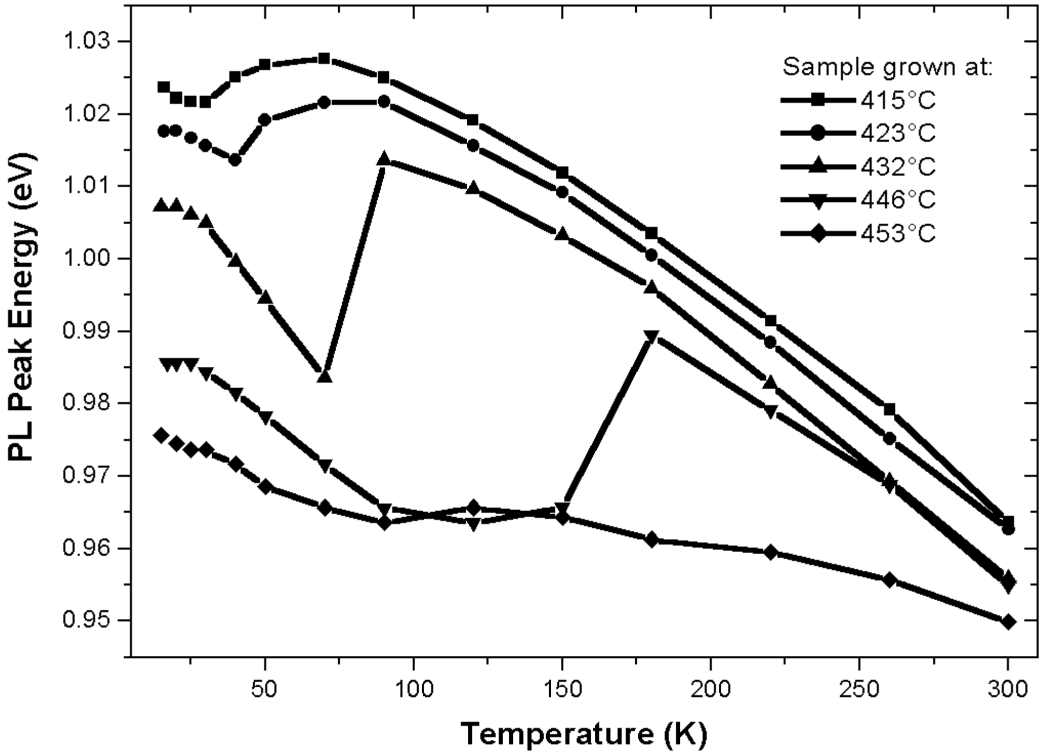

Fig. 3.17: PL-peak energy plotted as a function of temperature for samples grown at different temperatures. The excitation density was kept constant. The plots show the inverted S-shape, more pronounced for samples grown at high temperatures. With increasing growth temperature, the PL-peak shifts also to lower energies.

Remark: This is a later optimization of the QW-parameters as compared to the samples studied in Section 3.3, for 1.3 µm emission. Goal was to use thicker quantum wells and less In-content.

To show the essential conclusions of this study and in order to make the presentation of the results as clear as possible, only three from the six samples (which are representative) are discussed further in detail: the ones grown at 415, 432 and 453°C. Whenever different samples are compared, special care was taken to measure them in as much identical conditions as possible. The PL measurements are performed between 15 and 300 K.

To see why to localization energy is larger in samples grown at higher temperature, TEM studies for three of the samples presented in Fig. 3.17 were performed. The results are presented in Fig. 3.18 for the annealed samples grown at 415, 432 and 453°C. One can see an increase in QW-inhomogeneity with increasing growth temperature. The 415°C-grown sample has a homogeneous QW. The 432°C-grown sample has fluctuations in strain and composition in the QW-plane. In the 453°C-grown sample, additional QW-thickness fluctuations are visible.

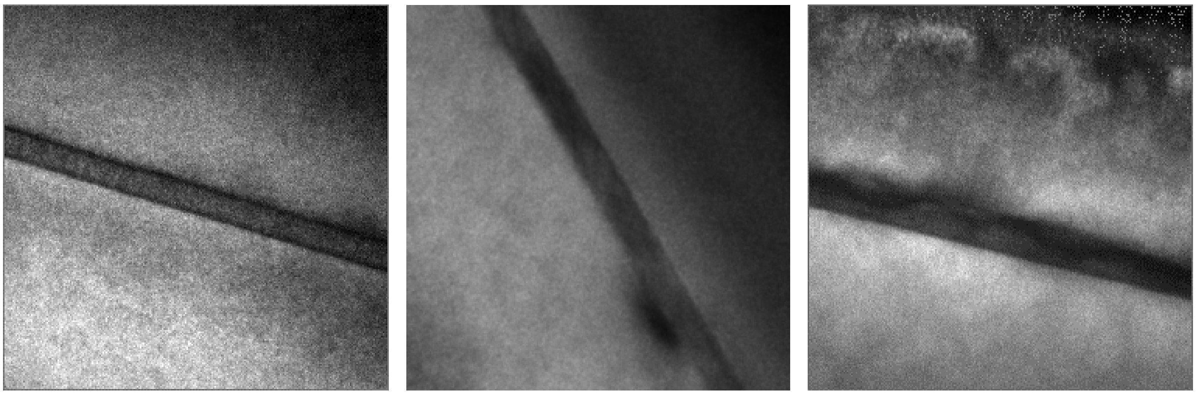

Fig. 3.18: Dark field TEM images [(002)-reflection] of the annealed samples grown at (from left to right) 415, 432, and 453°C, respectively. The 415°C-grown sample has a homogenous QW. The 432°C-grown sample shows contrast-variations inside (due to compositional variations) and near (due to strain variations) QW. The 453°C-grown sample shows strong variations of contrast inside and outside QW as well as variations in the QW-thickness (3D-growth). One can see an increasing contrast-inhomogeneity with increasing growth-temperature of the samples. The scale of these TEM images is missing, but it can be read from the QW-thickness, which is 9 nm [T. Remmele and M. Albrecht, unpublished].

Next, the manifestation of carrier localization in the PL-spectra is studied.

PL-spectra of annealed samples grown at different temperatures

Fig. 3.19 shows the PL-spectra measured at 15, 70 and 300 K of the annealed samples grown at 415, 432, and 453°C. The PL intensity is the highest for the 415°C-grown sample and decreases with increasing growth temperature. The energies of the PL-maxima are 1023, 1004 and 974 meV (red shift with increasing growth temperature), the PL full width at half maximum (FWHM) of 16, 22 and 30 meV at 15 K, respectively. The small value of the FWHM and the high PL-intensity shows that the sample grown at 415°C has a high quality compared to samples grown by other groups[32]. At 70 K, the samples grown at 415 and 453°C have a PL spectrum consisting of one peak, located at 1027 and 966 meV, respectively. The 432°C-grown sample shows two peaks in the PL spectrum located at 984 and 1015 meV.

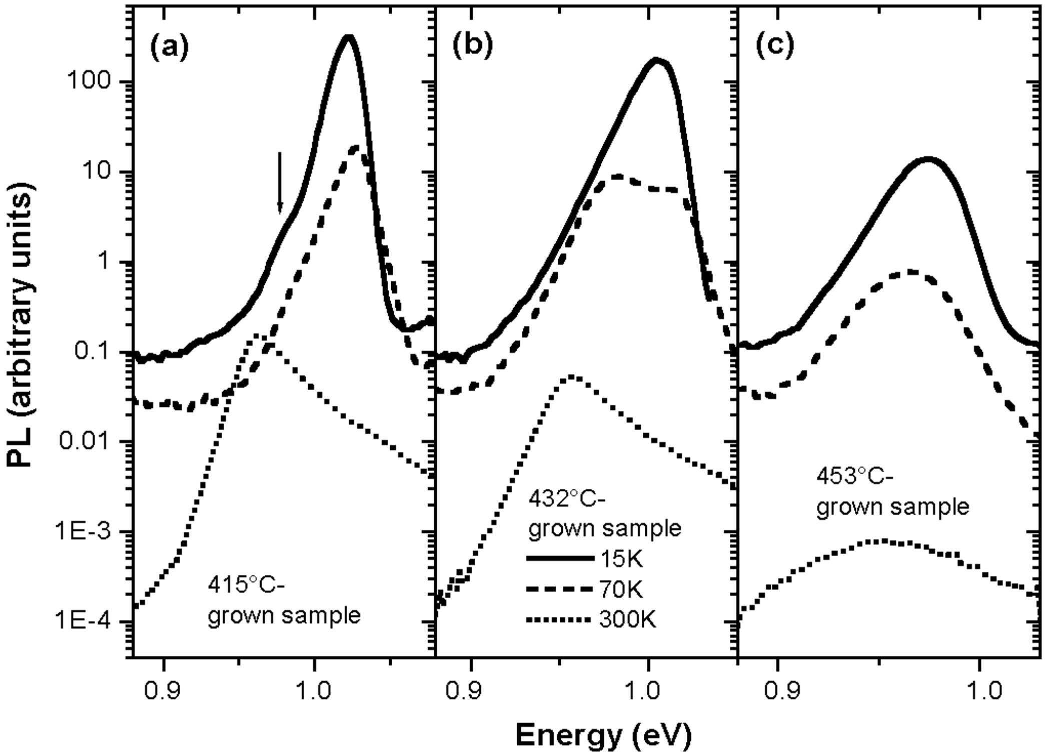

Fig. 3.19: Temperature-dependent PL spectra for annealed samples grown at **(a)** 415°C, **(b)** 432°C and **(c)** 453°C. The excitation density was 300 W/cm^2.

Some research groups[33] consider the PL spectrum of high-quality samples (which shows only one PL-peak), at low temperature, as a sum of contributions of photoluminescence from localized and free excitons. They interpret therefore the jump in energy associated with the S-shape as a transition from the PL due to localized excitons to a PL from free excitons. To talk about localized excitons in the 415°C-grown sample might be justified, but in the other two samples, which show two PL-peaks and emission at much lower energy, it is not clear if one can talk about localized excitons. The low-energy PL-peak in the 432°C-grown sample and the strong red-shift of the PL-peak in the 453°C-grown sample *are certainly due to carrier localization*, because all three samples studied in Fig. 3.19 have the same nominal composition of the QW; weather the localized carriers form excitons or not, depends on the particular potential landscape.

If the potential fluctuations are due exclusively to fluctuations of the In-composition along the QW or to variations in the QW-thickness, this leads to potential minima in the conduction band and potential maxima in the valence band spatially located in the same place: in this case one can speak about localized excitons. On the contrary, if potential fluctuations are due to fluctuations of the N-composition along the QW, potential minima in the conduction band can be associated with potential minima in the valence band (see Chapter 4); in this case the electron and holes are localized in different places. Therefore, as the existence of excitons is not clear in samples grown at high temperature, the low-energy PL (which is different from the low-energy PL-tail discussed in §3.2.4 and §3.3.1: it has a higher intensity and appears at higher energy) will be called further “localized photoluminescence”.

However, a difference will be made in the following between localized PL from localized excitons in homogeneous samples (like the 415°C-grown one), and *strongly* localized PL (SLPL) present in samples grown at high temperature, where additional potential fluctuations exist due to QW-inhomogeneity. Such a difference is necessary because calculations show that even homogeneous N-containing alloys may show localization effects due to diverse bond configurations (see the discussion in Introduction). For high quality samples, Shirakata et al.[32] measure an energy difference of 10 meV between localized and free excitons in as-grown samples and less in annealed samples. In our case the energy difference between the two peaks for the annealed 432°C-grown sample is 31 meV (equal with the “localization energy” read from the S-shape in Fig. 3.16), justifying the name “SLPL” for the low-energy photoluminescence; for the annealed, 415°C-grown sample (see Fig. 3.17), the localization energy is of only 6 meV.

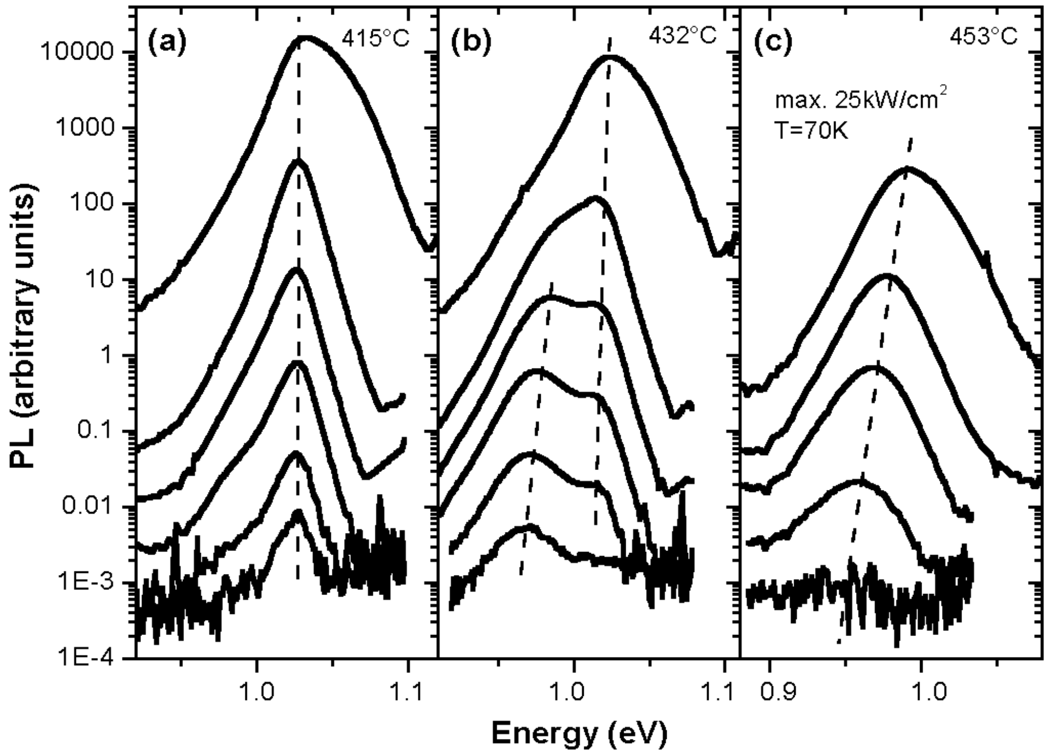

Fig. 3.20: Excitation-dependent PL spectra measured at 70 K for annealed samples grown at **(a)** 415°C, **(b)** 432°C, and **(c)** 453°C. The maximum excitation density was 25 kW/cm^2 and this corresponds to the PL spectrum with the highest intensity. The other spectra were taken by reducing successively the excitation power by a factor of 10. The dashed lines are guide to the eyes.

The strong red shift of PL in samples grown at higher temperatures indicates a larger contribution of SLPL to the whole PL, that is, stronger carrier localization in these samples (i.e. a higher density localized states). As can be seen in Fig. 3.19, the

432°C-grown sample contains PL from both strongly localized and free carriers (excitons). The potential fluctuations are minimal in the 415°C-grown sample and so large in the 453°C-grown sample, that here only the SLPL can be seen (note the strong red-shift of the PL in this sample as compared to the 415°C-grown sample). Increased potential fluctuations are also associated with increased FWHM. This indicates *an increased degree of inhomogenity in samples grown at higher temperature* and a consequent inhomogeneous broadening.

Excitation-dependence of the PL-spectra

To further study the properties of carrier localization, in Fig. 3.20 the excitation intensity dependence of PL spectra taken at 70 K for the three samples is represented. The 415°C-grown sample shows one PL-peak whose maximum moves between 1027 and 1033 meV when the excitation power is varied over 5 orders of magnitude. For the 432°C-grown sample the variation is between 970 and 1024 meV, *this sample shows clearly two peaks*. The 453°C-grown sample shows again only one peak, which is broad; the PL-peak maximum varies between 961 and 992 meV when the excitation power is varied on 3 orders of magnitude. This confirms the picture discussed above: the 415°C-grown sample is the most homogeneous, the 432°C-grown sample shows important potential fluctuations but the localized states can be filled under strong excitation. This is not the case for the 453°C-grown sample where even for the strongest excitation the whole PL comes from the localized states (SLPL)[34, 35].

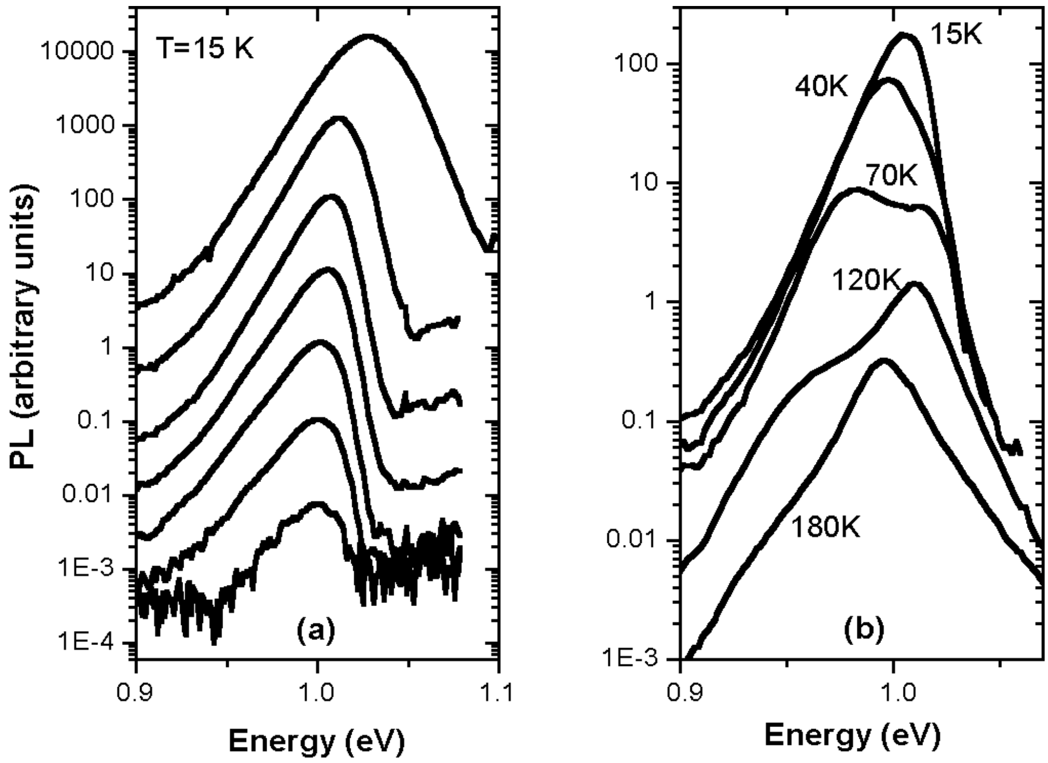

Fig. 3.21: Excitation and temperature dependent PL spectra of the 432°C-grown sample. In **(a)** the maximum excitation density is 25 kW/cm^2 and decreases for each curve by a factor of 10. In **(b)** the excitation density is kept constant and is 300 W/cm^2.

Properties of the PL-spectra in the 432°C-grown sample

To see how the double-peak structure evolves with the temperature and excitation density, in Fig. 3.21 the low temperature (15 K) excitation intensity and temperature dependence of the PL spectra for the 432°C-grown sample is shown. Comparing Fig. 3.20 (b) and Fig. 3.21, one can see that: (1) the double-peak structure is not visible at low and high temperatures, only around 70 K, and (2) at low and high temperatures, emission from localized states appear in spectra as exponential low-energy tails. At low excitation densities, the difference between the PL-peak energy at 15 and 70 K is about 32 meV. That is, at 70 K the SLPL is dominant. The localized states can be filled at 15 K, but not at 70 K, for low excitation densities.

Looking at Fig. 3.21(b), it is clear why the 432°C-grown sample shows the S-shape: due to strong localization the spectrum shows two peaks. As the temperature is increased, the higher-energy PL-peak overtakes the low-energy one and so the sudden change in the PL-peak energy takes place. For low temperature-grown samples, with a smaller degree of carrier localization, the S-shape is present at lower temperatures. In this case, the double peak structure in the PL spectrum is not clearly seen[32, 33]. With increasing localization, a higher energy is necessary to delocalize the carriers and the S-shape moves to higher temperatures.

3.5.2. Influence of the thermal annealing on the degree of carrier localization

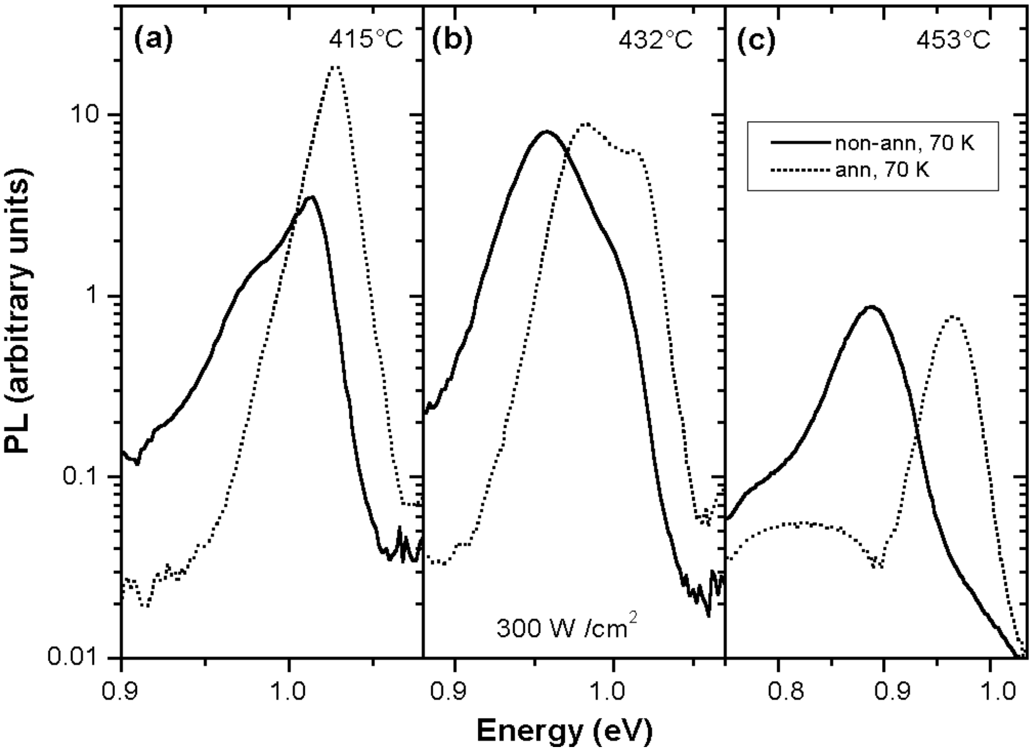

Fig. 3.22: The spectra of the samples grown at 415, 432, and 453°C, before and after annealing, measured at 70 K.

The spectra of the samples grown at 415, 432, and 453°C, before and after thermal annealing, at 70 K, are shown in Fig. 3.22. Only the low-temperature spectra are shown because the localization is not seen at 300 K. As discussed in Section 3.4, the thermal annealing reduces the potential fluctuations from the QWs and thereby also the localization of carriers; this conclusion was drawn from the parameters of the PL-emission like blue shift after annealing and PL-peak shift with excitation and temperature. The same can be seen directly in Fig. 3.22: besides the usual blue shift after thermal annealing, the low-energy shoulder present in the spectra of the first sample reduces after thermal annealing. For the 432°C-grown sample, the intensity of the high-energy PL-peak increases after thermal annealing. In the case of the third sample, all the PL emission comes from localized carriers; the blue shift after thermal annealing is the largest for this sample. Note that the PL spectra are drawn in log scale; plotted in linear scale, some spectral features could not be seen.

3.5.3. The temperature dependence of photoluminescence intensity

In this subsection, the temperature-dependence of the integrated-PL is investigated, in order to obtain information about the exciton binding energy and the non-radiative recombination.

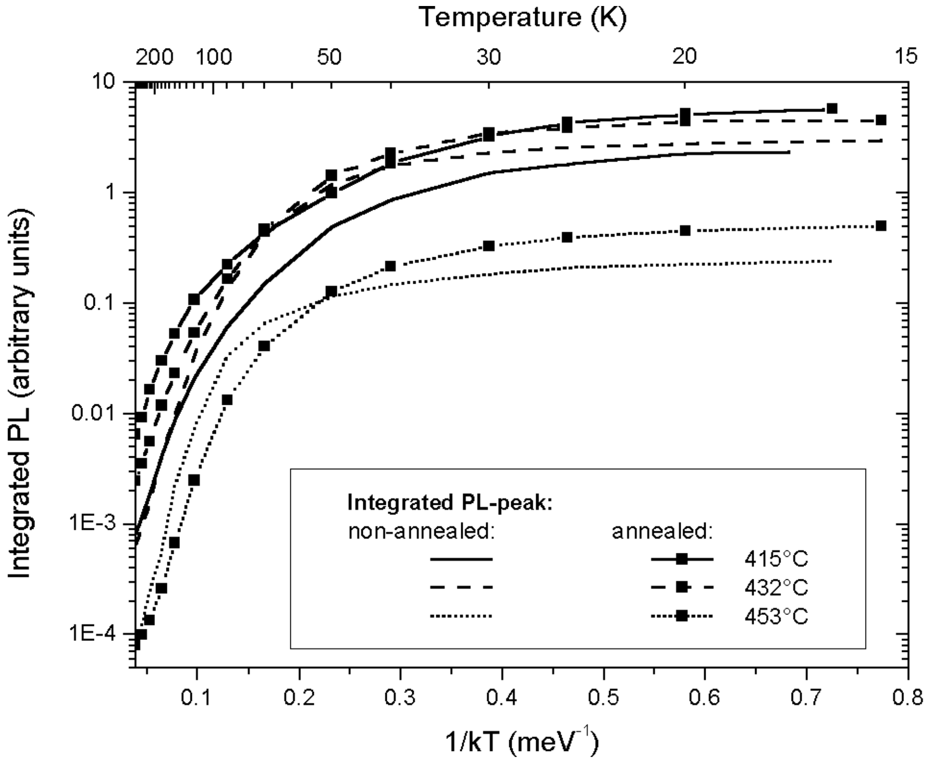

Fig. 3.23: The temperature-dependence of the integrated PL for the three samples grown at 415, 432, and 453°C, before and after annealing.

The integrated PL curves (as a function of 1/kT) in Fig. 3.23 can be fitted by an equation which expresses *the temperature-dependence of excitonic PL* in quantum wells[36], in order to obtain the exciton binding energy and information about the activation-energy of non-radiative recombination. The fitting equation is:

$$I\left(x=\frac{1}{kT}\right)=\frac{A}{\left(1+\frac{a}{x}e^{-bx}\right)\left(1+\frac{c}{x}e^{-dx}\right)} \tag{3.2}$$

where b and d are the free exciton binding energy and the activation energy of non-radiative recombination, respectively. a and c are weight coefficients.

A fitting with Eq. (3.2) is not possible for all the samples. Only for five samples, the ones grown at low temperature, the temperature-dependence of the integrated-PL can be fitted with Eq. (3.2). The results are given in Table 3.2.

Table. 3.2. The parameters obtained as a result of fitting the integrated-PL temperature-dependence using Eq. (3.2).

	a	b	c	d
415n	2.6	5.9	3.1	15.5
415a	5.9	7.6	0.44	15.5
423n	2.8	6. 7	6.8	23.3
423a	4.5	7.8	0.56	11.5
432a	2.3	7.4	4.6	20.7

Results

- the binding energy of the excitons is 6 - 8 meV (coefficient b). This value is typical for quantum wells;

- the activation-energy of the non-radiative recombination is small, between 15 and 23 meV (coefficient d). In reference [36], a much higher value of 106 meV is obtained for quaternary $In_{0.24}Ga_{0.76}As_{0.02}Sb_{0.98}/Al_{0.18}Ga_{0.82}As_{0.02}Sb_{0.98}$ quantum wells (and quaternary barriers)

- after thermal annealing, the weight-coefficient a of the excitonic photo-luminescence increases, the weight-coefficient c of the non-radiative recombination decreases. This tendency is expected, because the PL-intensity in as-grown samples is smaller than in annealed samples;

- with increasing growth temperature of the samples, the activation energy of the non-radiative recombination remains approximately constant;

Conclusions

The activation-energy of the non-radiative recombination is small, in agreement with the fact that the PL-intensity in InGaAsN QWs decreases fast with increasing temperature. *This activation-energy is similar in samples grown at high temperature.* This is somewhat expected, because the crystal quality of the samples grown at higher temperatures is better: the reason why the InGaAsN QWs are grown at low temperature is to obtain good homogeneity of the samples. *The question that arises* *is then: why the PL-intensity in samples grown at high temperature is lower than in the samples grown at lower temperature?*

3.5.4. The consequence of carrier localization on the photoluminescence intensity

As can be seen in Fig. 3.20, the samples grown at higher temperatures show less PL intensity for the same excitation density. They have, as discussed above, also a higher degree of carrier localization which is materialized in the double-peak structure and a red shift of the PL-spectra. A decrease in the PL intensity in the samples can be caused in two ways: (1) increased non-radiative recombination (decrease of the non-radiative lifetime) or (2) increase of the radiative lifetime. In both cases the PL quantum efficiency[36] is reduced.

Mair[37] *et al.* have measured in InGaAsN thick layers increasing PL decay times with decreasing photon-energy in PL-spectra. The same fact has recently been seen in InGaAsN-QWs emitting around 1.3 µm by Markus[38] *et al.*

On the other hand, as seen in §3.5.3, for samples grown at higher temperature the non-radiative recombination does not seem to become more important. The only way out, which could explain the decrease of the PL-intensity in the (inhomogeneous) samples grown at high temperature, is the increase in the radiative life time due to carrier localization: due to the high radiative lifetime of localized carriers, the quantum efficiency and PL intensity decrease in samples grown at higher temperatures. This hypothesis is verified in the next section.

3.6. Time-resolved photoluminescence studies

The motivation of the time-resolved PL-studies performed in this section is to find out why the PL-intensity decreases in inhomogeneous samples, grown at high temperature. As discussed in §3.5.3 and 3.5.4, the non-radiative recombination does not appear to be more important in samples grown at high temperature. The only explanation for the low PL-intensity in such samples is then an increase in the radiative recombination time due to carrier localization, and consequently low PL-efficiency. This hypothesis is verified in this section.

The time-resolved PL-study is also important by itself, in order to find out the values of the radiative and non-radiative decay-times, and how they depend on temperature.

First, a few basic information about time-resolved PL in QWs are discussed.

3.6.1. Theory, Basics

By a time-resolved PL experiment, the dynamics of the photo-excited carriers is measured: light pulses are used to excite electron-hole pairs and their further recombination is monitored. The excitation pulses are usually short (compared with the time scale on which the PL-decay time is measured) and intense. The dynamics of carriers generally depends on the way the excitation takes place: direct excitation of QW (with photon energies under the band gap of the barriers), or excitation of the barriers.

The PL-decay time includes both the radiative and non-radiative processes; it is given by the relation:

$$\frac{1}{\tau_{PL}} = \frac{1}{\tau_r} + \frac{1}{\tau_{nr}} \tag{3.3}$$

where τ_r and τ_{nr} are the radiative and non-radiative lifetimes, respectively.

The case of an ideal QW

In an ideal QW the interfaces are perfect; there are no potential fluctuations and no carrier localization effects. The non-radiative recombination is neglected ($\tau_{nr} = \infty$).

The PL (radiative) lifetime depends on:

- the electronic band structure of the QW- and barrier-material (weather the semiconductor materials are optically direct or indirect, weather the QW is of type I or II);
- the degree and kind of QW- and barrier-doping;
- weather the PL is excitonic, or comes from free carriers. At low temperatures, the excited carriers exist as excitons. At high temperatures, excitons and free carriers coexist;
- temperature and excitation density. At high temperatures, the carriers can escape out of the QW. The carrier-escape rate depends on the QW band offsets;
- the type of excitation, QW- or barrier-excitation. When carriers are excited in barriers they have first to be captured in the QWs: the PL signal is delayed correspondingly (by tens of ps);

The effect of temperature on the PL rise and decay times in the case of an ideal QW was calculated by some authors[39]. The results are different for resonant and non-resonant excitation (i.e. excitation of the lowest electron and hole energy levels in QW, or excitation of states of higher energy). The difference between the two cases comes from the loss of exciton coherence (through phonon-scattering) during the relaxation of the non-resonantly excited excitons. The loss of coherence increases the recombination (decay) time. Other theoretical predictions are summarized next:

- in the case of non-resonant excitation, the PL rise time decreases with increasing temperature due to faster relaxation processes at high temperatures;
- the PL-decay time increases with increasing temperature, due to thermal dissociation of excitons;
- the rise and decay times increase with increasing QW-width: the decay time increases due to reduction of oscillator strength (confinement reduction), the rise time increases due to less exciton-phonon interaction;

Finally, note that electric and magnetic fields (internal or external) influence additionally the PL rise and decay time.

The case of a real QW

A real QW has potential fluctuations (due to composition- and QW-thickness inhomogeneity) and non-radiative recombination channels, which influence the carrier dynamics. The result is a dependence of the PL-decay time, at low temperatures, on photon energy.

Depending on temperature and the magnitude of potential fluctuations and temperature, the excited carriers can be thermalized (the quasi-Fermi levels for the photo-excited carriers do not depend on spatial coordinates) or only partially thermalized (the quasi-Fermi levels depend on spatial coordinates). When the carriers are thermalized, the PL-decay time does not depend on photon energy.

Besides the factors mentioned in the case of an ideal QW, for the real-QW case the dynamics of the excited carriers depends additionally on:

- the non-radiative recombination channels (in QW and barriers);
- potential fluctuations in barriers and QW;

By combining a temperature-dependent PL time-resolved and time-integrated analysis, under certain hypotheses[40], the temperature dependence of the radiative and non-radiative decay times, τ_r and τ_{nr}, can be determined as described in §3.6.5.

Results for different QWs

1) For SiGe QWs grown on Si, decay times of the order of 100 ns have been measured[41] (optically-indirect semiconductor).

2) For GaAs/AlGaAs QWs, a minimum decay time of 10 ps was measured[42] under resonant excitation, at 1.7 K in high-quality, non-doped samples (short decay times due to the resonant excitation). However, much longer times have been measured for free (400 ps)[43, 44] and bound (1 ns) excitons at 20 K[44], for non-resonant excitation. Other authors[45] have measured a bi-exponential decay in GaAs QWs with interface roughness and decay times of 1 - 5 ns.

3) For InGaAs/GaAs QWs: experiments have revealed the importance of carrier escape out of the QW and consequently, the quality of the neighboring regions (barriers, confinement layers)[46]. PL-decay time between 500 ps (at 10 K) and 40 ns (at 300 K) were obtained in high-quality QW-structures, for non-resonant excitation. On the contrary, if non-radiative channels are present in the barriers, the PL-decay time is only 100 ps already at 120 K (and decreases strongly further at 300 K). In samples of high-quality, radiative decay times between 500 ps (at 10 K) and 2 µs (at 300 K) were reported. Concerning the non-radiative decay times: in high-quality samples time constants between 500 ns (at 70 K) and 50 ns (at 300 K) were reported; in lower quality samples the variation is between 5 ns (70

K) and 100 ps already at 120 K[46]. Responsible for these small decay times in the lower quality samples at high temperatures is the thermal escape of carriers out of QWs and further non-radiative recombination in the barriers.

Other authors[47] measure decreasing PL-decay times for increasing QW-thickness. This is explained by increase non-radiative recombination in thick QW.

4) Other results reported in the literature include:

   - large (100 ns) decay times in InAlAs/AlAsSb QWs, due to type-II band alignment[48];
   - interesting results reported in InGaN/GaN QWs, which show important carrier localization and non-homogeneity. Some authors have reported PL-decay times of tens of ns[49]; other authors[50] report multi-component decays of PL at 12 K, containing short times at early stage (200 ps) and long extended decay times (10 ns). The temperature-dependence of the PL-decay times is influenced by carrier localization.

5) Kaschner[51] *et al.* were the first to report time-resolved PL in InGaAsN samples. They report PL-decay times of 1 - 4 ns at 4 K, and 500 ps at 300 K.

The measurements performed on InGaAsN samples

Time-resolved PL-measurements were done on the samples discussed in the previous section. The detailed results for the 415, 432 and 453°C-grown samples are shown in Appendix C. The decay times are always evaluated for the time-range between 100 and 1000 ps.

The measurements were performed at different temperatures - between 10 and 290 K - and at different excitation powers, for each temperature. Both annealed and non-annealed samples were measured, and both QW- and barrier-excitation was used. The given excitation power means the time-averaged excitation power of the light pulses.

3.6.2. Study of high-quality samples. Influence of thermal annealing

Time-resolved spectra for the 415°C-grown sample, annealed and non-annealed, are given in Fig. 3. 24. The measurements were performed at 10 K, for barrier-excitation, and for an average excitation power of 2.5 mW. Some parameters of the time-resolved PL-spectra are summarized in Appendix C, Tables 2 and 3.

Discussion of results

By examining Fig. 3.24 and Tables 2 and 3 in Appendix C, one can see that:

♦ *the PL-decay time decreases with increasing temperature,* both for annealed and non-annealed samples, from around 1 ns at 10 K to around 100 ps at 170 K (see Fig. 3.28). The non-radiative recombination channels are activated at high temperature, for both annealed and non-annealed samples, either in the QW itself or in the barriers, where carriers can escape at high temperatures;

- *under 100 K, the PL-decay time increases with decreasing photon energies.* Over 100 K, the PL-decay time tends to be the same, independent of the photon energy. By looking at Fig. 3.24, one can see that the high-energy PL time-evolution curves intersect the low-energy ones; that is, the PL from the lower states live even after the depletion of the higher energy states, and the long life times of the low photon energy PL is not due to carrier relaxation from the higher-energy states;

- *the PL-spectra shift in time to lower photon energy,* due to different decay times of the localized and non-localized states and to carrier relaxation to lower energy states. The shift depends on temperature. At 10 K, the shift is of 12 meV, both for annealed and non-annealed samples. At high temperatures the shift tends to zero: due to the high thermal energy of the carriers ($\approx kT$), they can move in the potential landscape, and the PL decreases in the same manner for all photon energies;

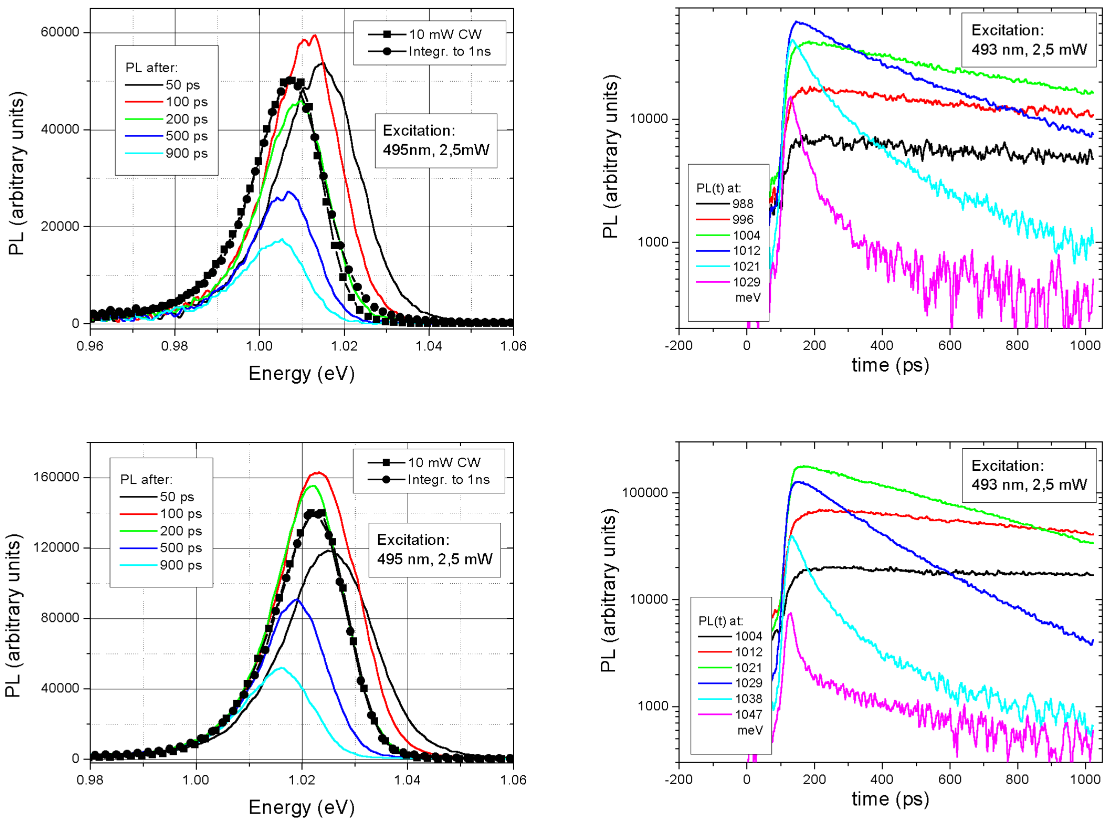

Fig. 3.24: The time-resolved PL measurements for the 415°C-grown sample, at 10 K (barrier excitation). On the upper half the non-annealed sample is shown, on the lower half the thermally annealed sample.

- *the PL-decay time decreases with increasing excitation intensity* at low temperatures. This means that the (integrated) PL-decay time constant becomes longer with increasing delay after the excitation pulse. This is due to the QW-inhomogeneity. The time evolution of the PL-decay cannot be described by a simple exponential law for wide time-windows;

- *at low temperatures, the PL-decay time is smaller after annealing.* This indicates a better QW-quality (less potential fluctuations) after annealing. At high temperatures this relation is reversed (longer times for the annealed sample), which shows that the thermal annealing reduces the non-radiative recombination rate at high temperatures.

Conclusions

The PL-decay in time is generally non-exponential. The given values of the decay times are valid between 100 and 1000 ps. The PL-decay time has a strong dependence on photon energy, at low temperatures: they increase with decreasing photon energy. It also has a strong dependence on temperature: from ≈1 ns at 10 K to 100 ps at 170 K. The time-integrated PL-spectrum between 0 and 1 ns compares well with the CW-PL spectrum

3.6.3. Difference between the QW- and barrier-excitation

In Fig. 3.25, the low-temperature results for the 415°C-grown sample are shown. Again, all relevant data extracted from the measurements are given in Appendix C, Table 4. In the case of QW-excitation, because the laser line is close to the spectral region where the spectra are measured, the laser interferes with the measurement for short times after the laser pulse: under 50 ps the results are not reliable.

Discussion of results

By comparing the results for QW- and barrier-excitation, one can see that:

- the dependence of the time-resolved PL-parameters on temperature, photon energy, time, excitation intensity and annealing is in principle the same in the case of QW-excitation as in the case of barrier-excitation;

- in the case of QW-excitation, the decay times are generally smaller than in the case of barrier-excitation (compare Figs. 3.24 and 3.25). For example, the PL-decay times for the annealed sample at the lowest temperature are ≈600 ps for barrier-excitation and ≈100 ps for QW-excitation. This suggests that there is carrier trapping in the barriers, so that the carrier dynamics in the case of barrier-excitation is influenced (or even determined) by carrier trapping and de-trapping rates in the barriers. The trapping in the barriers is also suggested by examining the evolution in time of the PL spectra: in the case of barrier-excitation, the maximum of the PL appears 100 ps delayed after the excitation pulse. In the case of QW-excitation, the maximum of the PL intensity appears immediately (50 ps) after the excitation;

- by measuring the rise time of the PL signal in the case of the barrier-excitation, an estimation of the carrier-capture time in the QW is obtained: this is around[70] 30 ps, independent of temperature, for both annealed and non-annealed samples.

This time is too small to account for the difference between the PL-decay times of the barrier- and QW-excitation;

- there is a red shift of the PL-spectra for QW-excitation compared with barrier-excitation (of about 10 meV). This is probably due to the loss of carrier correlation for the case of barrier-excitation.

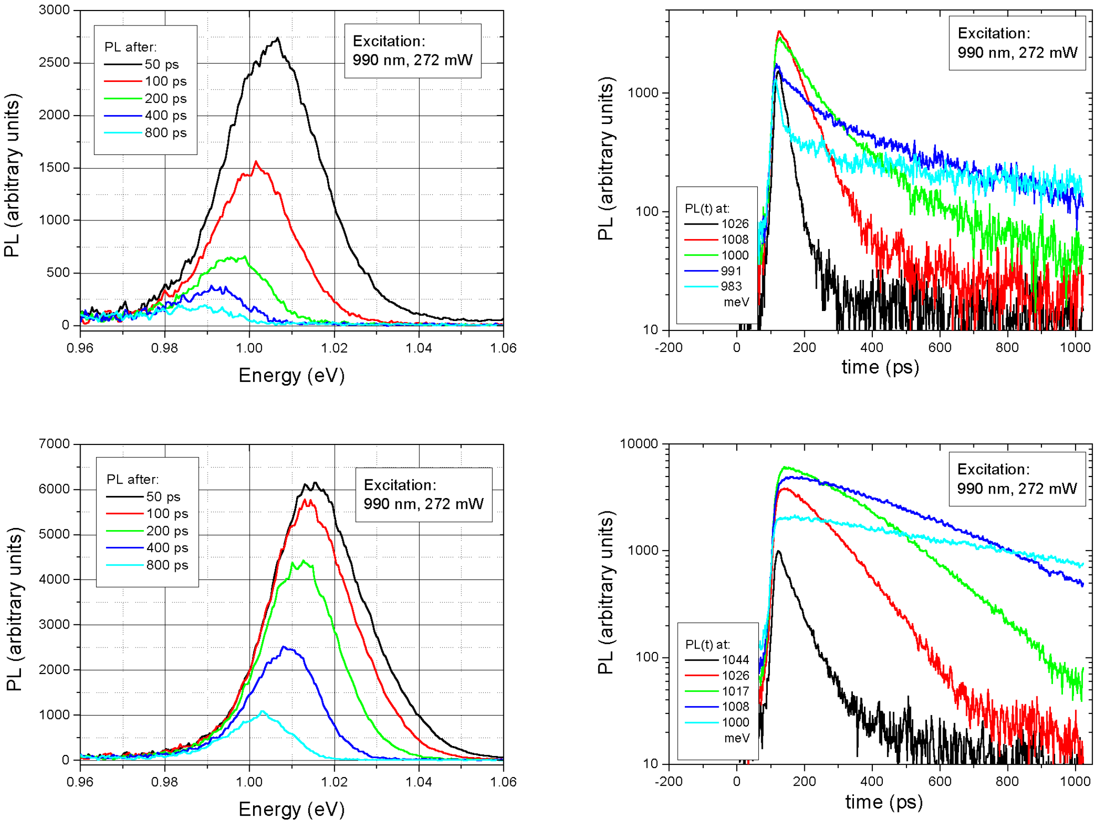

Fig. 3.25: The time-resolved PL measurements for the 415°C-grown sample, at 15 K and for QW-excitation. On the upper half the non-annealed sample is shown, on the lower half the thermally annealed sample.

Conclusions

Shorter decay times in the case of QW-excitation as compared to barrier-excitation *indicate* carrier trapping in the barriers, followed by slow carrier detrapping. The capture-time of the barrier-photo-excited carriers in the quantum well is estimated at 30 ps.

3.6.4. Study of inhomogeneous samples. The effect of strong carrier localization effects on the photoluminescence properties

In Fig. 3.26 and 3.27 and in Appendix C (Table 5) the results for the 432°C- and 453°C-grown samples are shown (barrier-excitation).

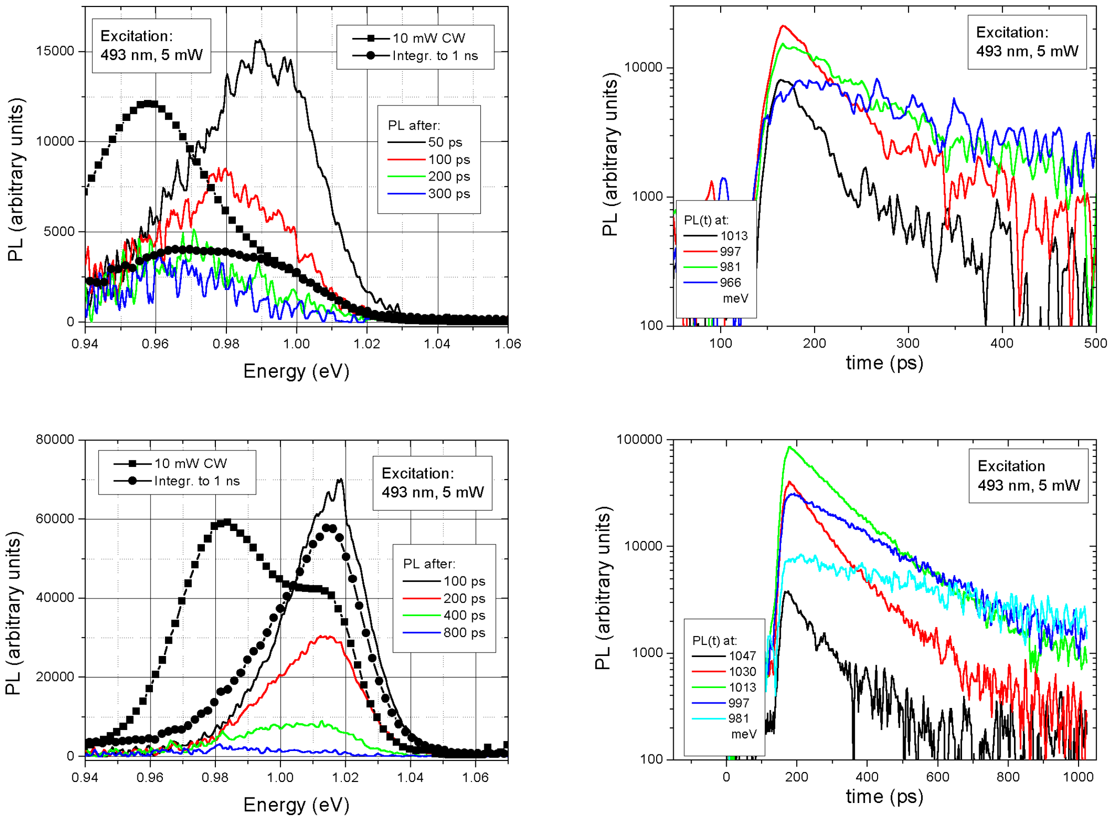

Fig. 3.26: The time-resolved PL measurements for the 432°C-grown sample, at 70 K (barrier-excitation). On the upper half the non-annealed sample is shown, on the lower half the thermally annealed sample.

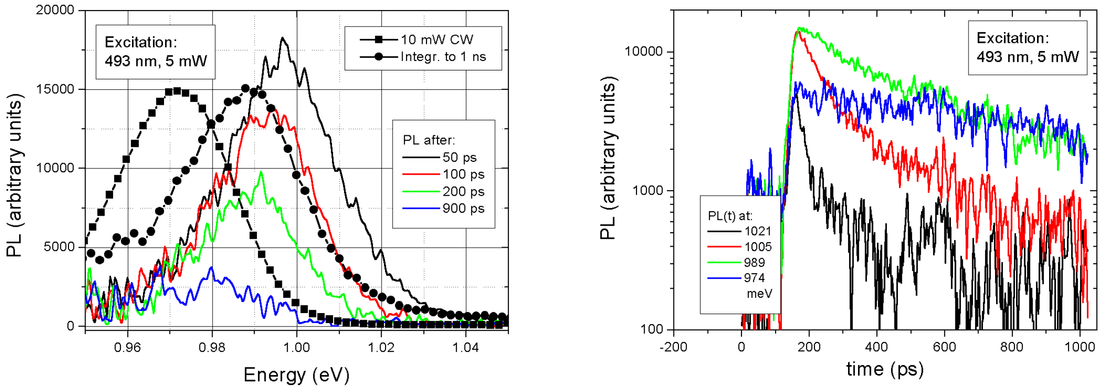

Fig. 3.27: The time-resolved PL measurements for the thermally annealed, 453°C-grown sample (barrier-excitation, 35 K).

Discussion of results

As it can be seen in Appendix C (Table 5) *the dependence of the PL-decay times on temperature* is in principle the same for the 432°C and 453°C-grown samples as for the 415°C-grown sample. The PL-decay time-constant decreases with increasing temperature and after annealing becomes longer.

At low temperatures the non-annealed 432°C-grown sample shows a clear non-exponential PL-decay. After thermal annealing, the PL-decay becomes almost exponential. It is concluded that, at least in this case, the non-exponential PL-decay is due to strong in-plane QW-potential fluctuations (see Fig. 3.18).

The dependence of the PL-decay time-constant on photon energy is the already known one: it increases with decreasing photon energy. Over 100 K, the decay time is almost independent of photon energy.

The larger inhomogeneity of the 432°C and 453°C-grown samples can be seen also from the larger PL-spectra shifts in time. These shifts are now up to 30 meV.

After annealing the PL-decay time becomes larger (at low temperatures, there are two decay constants for non-annealed samples). This is probably due to the reduction of the non-radiative recombination rate after thermal annealing. The PL-intensity is much improved after thermal annealing and the PL-peak is blue-shifted, like in the case of normal PL.

The effect of strong carrier localization effects on the photoluminescence properties

Comparing the 432°C and 453°C-grown samples with the 415°C-grown sample, one can generally see that the PL-intensity decreases with increasing growth-temperature and sample non-homogeneity. *Quite unexpectedly,* the PL-decay times also decrease with increasing sample growth-temperature. This needs further explanation, because in fact the opposite is expected: in samples with strong carrier localization, longer PL-decay times are expected. The PL shifts to lower energies with increasing growth temperature. The FWHM and the shift in time (ΔE_C in Table 5, Appendix C) of the PL spectra increase with increasing growth temperature.

Now the very short PL-decay time constants for the high-temperature grown sample is clarified. These short times express the decay of a small part of the whole PL, namely the one of high photon-energy. Most of the PL is very slow and not seen in these measurements, performed in the time interval 0 - 1 ns, due to its low intensity. Comparison of the CW (continuous excitation) PL with the integrated-PL on the interval 0 - 1 ns makes this clear - see Figs. 3.24, 3.26, and 3.27. In these figures the CW-PL and the time-integrated (between 0 and 1 ns) PL are represented. One can than clearly see (Fig. 3.24) that for the 415°C-grown sample, the integrated PL resembles well the CW-PL. This is not the case for the 432°C-grown sample at 70 K (Fig. 3.26) and for the 453°C-grown sample at 35 K (Fig. 3.27). For the last two samples, the low-energy PL from the CW-PL is not included in the integrated-PL. This means that the low-energy PL has a small intensity and that it lives much longer than 1 ns. This fact can be clearly seen on the right-hand side of Figs. 3.24, 3.26, and 3.27, where PL as a function of time is represented: while for the 415°C-grown sample the low-energy PL is still small 1 ns after the excitation pulse, for the other two samples *the low-energy PL-curve has the highest level among all the other energies after 1 ns and it has a slow decay*. This means that the missing low-energy PL occurs after 1 ns.

This experimental observation gives an explanation for the low PL-intensity in inhomogeneous samples. The PL-efficiency, defined by:

$$\eta_{PL} = \frac{\tau_{nr}}{\tau_{nr} + \tau_r} \tag{3.4}$$

becomes smaller in the inhomogeneous samples due to the large radiative lifetime τ_r (τ_{nr} is the non-radiative life-time).

The same picture is preserved at high temperatures: the excitation-dependent CW-experiments shows supra-linear behavior of the PL-intensity at temperatures above 70 K. Strong Auger recombination would rather lead to a saturation of the PL-intensity. Auger recombination does not seem to play an important role at excitation densities up to 50 kW/cm^2 (the maximum power used in these experiments).

Conclusions

For inhomogeneous samples, the PL-decay has a strongly non-exponential behavior, reduced after thermal annealing. The 1 ns-integrated PL does not compare well with the CW-PL: localized states have life times much longer than 1 ns. This explains the low PL-intensity (efficiency) in inhomogeneous samples.

3.6.5. Radiative and non-radiative decay times in InGaAsN quantum wells

Due to the basic non-exponential decay of the PL, radiative and non-radiative time constants cannot be strictly defined. In general, τ_r and τ_{nr} are functions of temperature and excitation power. However, such a study makes sense for the high-quality, 415°C-grown sample, which shows almost exponential PL-decay time.

To determine τ_r and τ_{nr} as a function of temperature[40], three things must be known: (1) the PL-efficiency, $\eta_{PL}(T)$, as a function of temperature, (2) the PL-decay time, $\tau_{PL}(T)$, as a function of temperature, and (3) the initial value of the PL efficiency, $\eta_{PL}(T_0)$, at low temperature. For $\eta_{PL}(T)$, the temperature dependence of the integrated CW-PL is taken. $\tau_{PL}(T)$ was determined by performing time-resolved measurements. The problem is with the initial value of the PL efficiency, $\eta_{PL}(T_0)$, which is not exactly known. By knowing $\eta_{PL}(T)$ and $\tau_{PL}(T)$, the values of τ_r and τ_{nr} can be determined from Eq. (3.3) and (3.4).

In Appendix C, Tables 6 and 7 the values of η_{PL}, τ_r and τ_{nr} for the annealed and non-annealed 415°C-grown sample are given. The initial value of the PL-efficiency is assumed to be 1 (this is an approximation!) at 4 K ($\eta_{PL}(4\,K)=1$) for the thermally annealed sample. For the as-grown sample, the value of the quantum efficiency at 4 K was taken smaller than 1, equal to the ratio of the integrated CW-PL measured at 15 K for the non-annealed and annealed samples. The results for τ_{PL}, τ_r, and τ_{nr} are plotted in Fig. 3.28.

One can see that the value of τ_r for the as-grown and annealed sample is approximately the same, and increases with the temperature. The big difference between the two samples concerns the τ_{nr}, which is much smaller in the as-grown sample in the whole temperature range between 10 and 100 K.

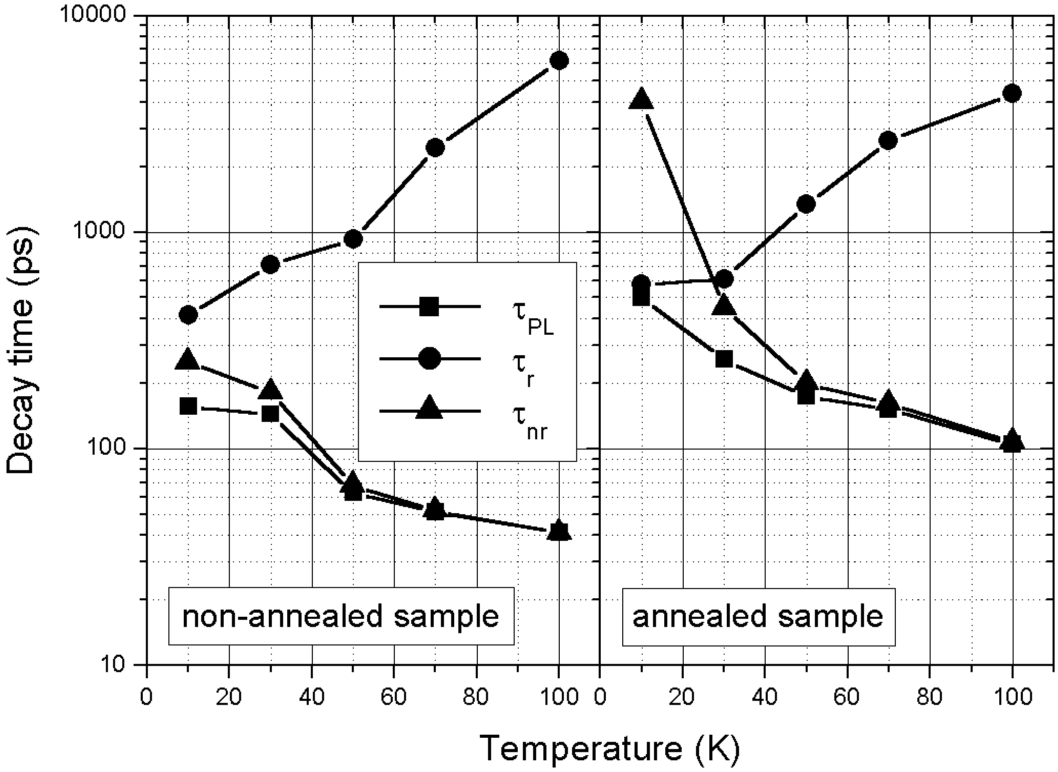

Fig. 3.28: The PL, radiative and non-radiative decay times as a function of temperature, for the 415°C-grown sample and for barrier-excitation (495 nm).

Conclusion

There is a high rate of non-radiative recombination, due to the presence of nitrogen, in as-grown InGaAsN QW-samples, which increases strongly with increasing temperature. The rate of non-radiative recombination is reduced substantially after thermal annealing. The high rates of non-radiative recombination, combined with carrier-localization effects present in inhomogeneous samples, explain the low PL-intensity of InGaAsN quantum wells at temperatures above 50 K.

Chapter 4
Band-offsets Determination in Quantum Wells using Surface Photovoltage

In this chapter a novel method of band offset determination is presented. The method is based on surface photovoltage and is used to determine the band offsets of InGaAsN QWs emitting around 1.3 µm. For comparison and in order to test the method, the band offsets of the well-known InGaAs QWs are also measured. InGaAsN and InGaAs QWs grown on GaAs have band offsets of type I. The method allows also the measurement of band offsets in type II QW-systems. A known type II QW-structure is examined in detail: GaAsSb QWs grown on GaAs substrate. Measurements performed on GaAsN QWs indicate a type II band alignment.

4.1. Introduction

The band offsets of semiconductor QW-structures are among the most important parameters one needs to know, in order to predict the properties of electronic or optoelectronic devices based on such structures. For example, as mentioned in Introduction, the conduction/valence band offsets determine in QW semiconductor lasers their temperature behavior, which is a crucial quality of a QW-based laser.

As discussed in the Introduction, the N-containing III-V ternary or quaternary semiconductor alloys have recently emerged as new interesting materials for (opto-) electronics and photonics[3, 52, 53]. Experimental information about band offsets of GaAs/InGaAsN/GaAs QW-structures are rare in the literature[54]; for the GaAs/GaAsN/GaAs quantum wells it is still debated, weather the band alignment is of type I or II[58]. The motivation of the work done in this chapter is to determine the band offsets/alignment of InGaAsN and GaAsN quantum wells.

The band alignments and band offsets are not simple to measure. Until now, mostly indirect - electronic or optical methods[55, 56, 57, 58] - have been used. The general problem with these methods is that, in order to apply them successfully, other parameters of the structures have to be known accurately. For example, when the optical absorption is used to determine the band offsets, the energies of optical transitions between the discrete levels in the QW are first experimentally determined. Then, using a fitting procedure, the band offsets are calculated under the assumption that the other parameters of the structure are known: the effective masses of electrons and holes, the geometry of the structure and the QW-potential. If one of these parameters is not known accurately, the results of the fitting procedure are not precise. Additionally, a series of samples is needed in order to identify the different optical transition between quantized electron/hole levels in the quantum well.

The method proposed in this chapter is based on surface photovoltage (SPV)[59, 60, 61]. The band offsets of a QW-structure are directly determined, if the energy of the first quantized electron/hole states are known. It has the further advantage that only one sample is necessary, in order to measure the band offsets. The band alignment results straightforwardly by examining the surface photovoltage spectrum. The sample structure is simple and no ohmic contact is needed.

4.2. Description of the method

4.2.1. Sample structure

The structure of the samples studied in this chapter differs from the one presented in Chapter 2 and is shown in Fig. 4.1. All the samples are grown on n-doped substrate and contain one QW embedded in the middle of a MBE-grown GaAs layer of 300 - 400 nm thickness. The QW and the grown GaAs layer are not intentionally doped.

The GaAsSb QW-sample was grown by molecular beam epitaxy (MBE). The Sb content is 30%. The InGaAs and InGaAsN QW samples were prepared from MBE-grown laser structures. The In content is 20% in the InGaAs sample and 35% in the InGaAsN sample; the N content is 1,7%. The preparation of the samples from laser structures consisted in the removal of the upper confinement layer using chemical etching. Special care was taken to stop etching as soon as the confinement layer was etched, so that the QW inside the GaAs undoped region remains intact. The other confinement layer (alternating AlGaAs/GaAs layers) is n-doped, like the substrate. The QW thickness is 7, 6.5 and 8 nm, for GaAsSb, InGaAs, and InGaAsN QW sample, respectively

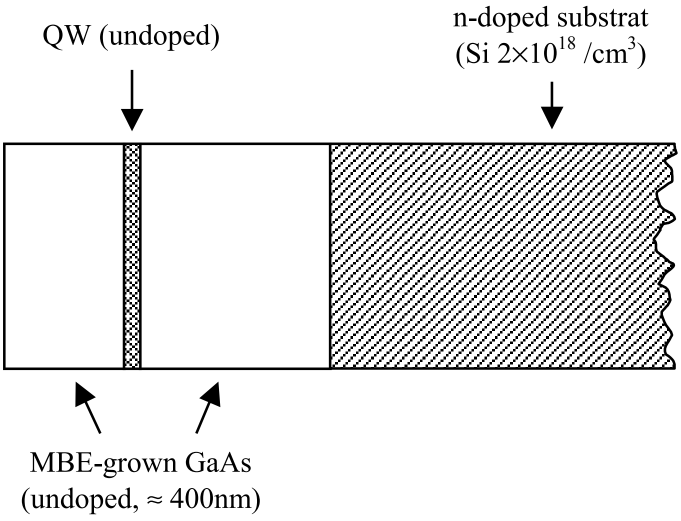

Fig. 4.1: The structure of the samples used in band offsets measurements.

4.2.2. Measurement setup

The measurement setup[62] is presented in Fig. 4.2. The sample is sandwiched between the massive copper plate of the cryostat (ground contact) and a transparent (ITO) contact. No dc contact is needed between the sample and the electrodes; the distance between the sample and the electrodes is a few μm thus making a capacitive (soft) contact. Chopped monochromatic light illuminates the sample on an area of about 5×5 mm through the transparent electrode. The photovoltage signal taken from the transparent electrode is applied to a high impedance buffer (a few GΩ) and measured by standard lock-in technique.

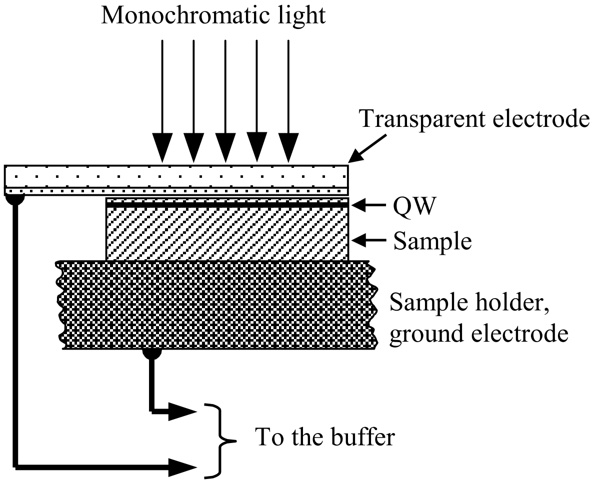

Fig. 4.2: Experimental setup. The sample is sandwiched between the ground electrode (sample holder) and the transparent ITO electrode. The signal, collected from the transparent electrode, is applied to a high impedance buffer.

4.2.3. The equivalent circuit

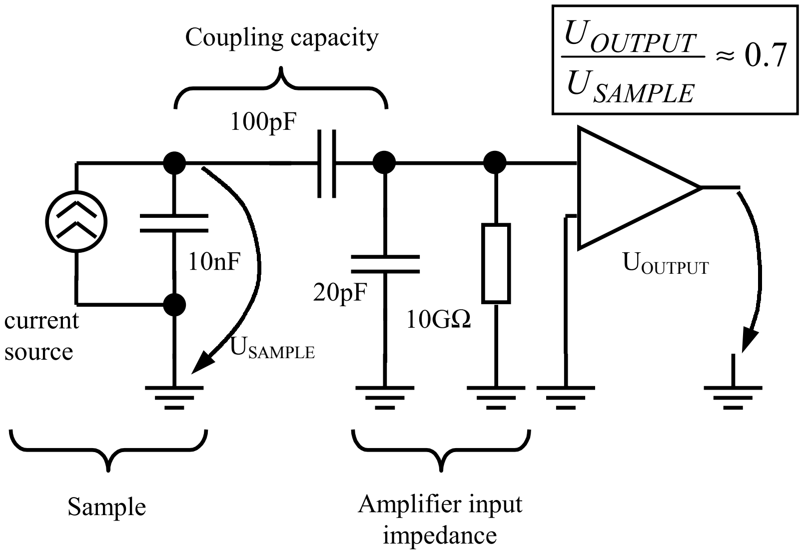

Fig. 4.3: The equivalent electrical circuit.

When light falls on the sample, electron-hole pairs are generated near the surface. As shown in the next section, in this region a built-in electrical field is present which causes the separation of electrons and holes; the result is a net current flowing toward the surface. This situation is represented in Fig. 4.3 as a capacitor charged by this current: the photovoltage is then defined as the voltage drop on this capacitor. The plates of the capacitor are the surface and the n-type substrate, were the holes respectively the electrons accumulate. Because chopped light is used, the photovoltage (PV) varies periodically with the frequency of chopped light.

The coupling between the sample and the amplifier (buffer) is made through the capacity that exists between the surface of the sample and the transparent electrode (ac coupling), and only *variations* of the PV across the sample are measured. Because the substrate is doped (no electric field present), the PV-variations come only from the (intentionally) undoped region near the surface, which contains the QW.

Fig. 4.3 also gives the typical values of the circuit elements. The electrical circuit is a high-pass filter having a time constant of approximately 0.1 s. Because the light chopping frequency is a few tens of Hz, the signal appears undistorted at the output of the buffer, but it is reduced by about 30% due to losses in the capacity cascade and buffer.

4.2.4. Model of the photovoltage generation

QW not present

Next, the mechanism of PV generation is explained. As it is well known[63], the Fermi level is pinned at the GaAs surface approximately in the middle of the band gap (0.7 eV under the conduction band). In the strongly doped substrate (2×10^{18} cm^{-3}), the Fermi level has a position close to the conduction band. Consequently, there is a built-in electric field ($E \approx 10^4$ V/cm) in the undoped region between the surface and doped substrate. The following hypotheses are used: (a) the energy of the photons is only slightly above the GaAs band gap, and (b) the surface Fermi level is pinned at 0.7 eV under the conduction band.

The generation of the PV can be explained using a simple model explained in the following (see Fig. 4.4). When light is applied, the built-in electrical field separates the photo-generated electron-hole pairs giving a current charging the capacitor between the surface and substrate. The current charging the capacitor can be separated in three parts:

- I is the photocurrent given by the photo-generated electron-hole pairs in the built-in electric field;
- $(-I_r)$ is the volume recombination current;
- $(-bI_{th})$ is the surface recombination current;

a) without light

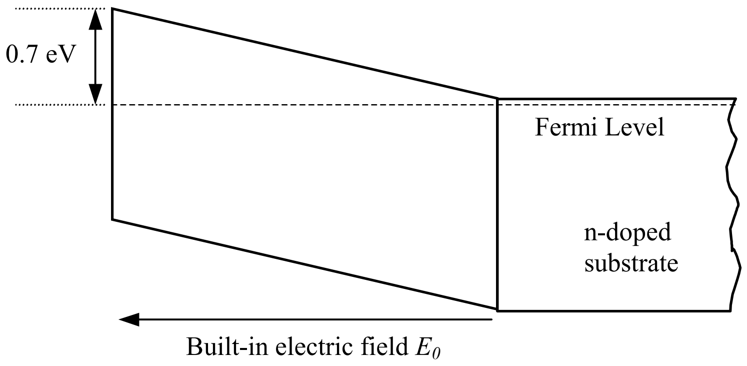

b) with light

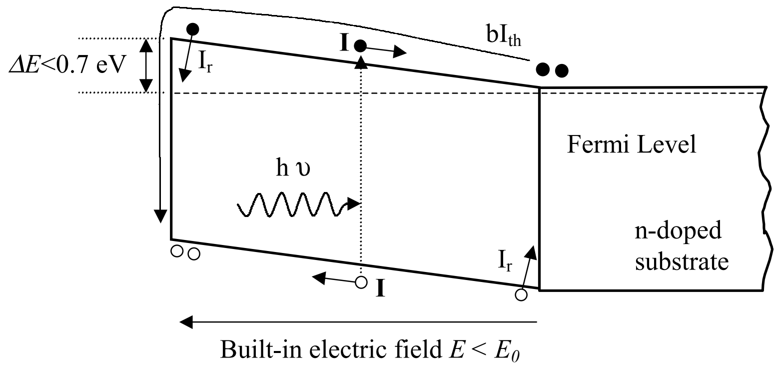

c) structure with QW

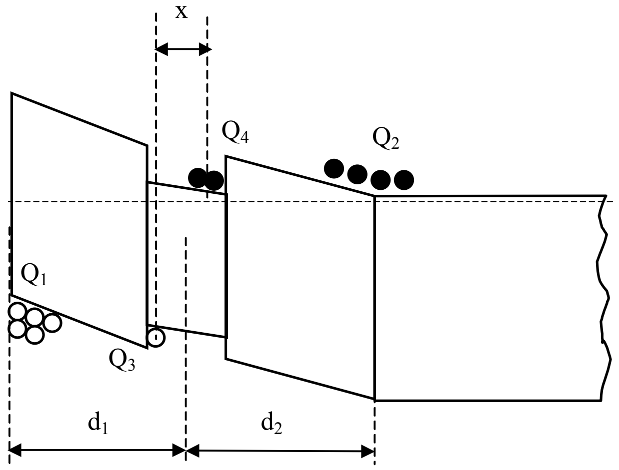

Fig. 4.4, (a) and **(b):** generation of photovoltage. Under illumination: the photons generate electrons-hole pairs giving the photocurrent *I*. Some of the generated electrons and holes recombine giving the current I_r. The electrons and holes, which do not recombine, separate in the built-in electric field. I_{th} is the thermionic current (similar to the case of unipolar device: n-doped substrate in one side, surface states on the other side). **(c)** When only the quantum well is excited, charge may accumulate in the QW. Q_1 is the positive charge accumulated at the surface, Q_2 the negative charge accumulated in the substrate; Q_3 (Q_4) is the positive (negative) charge accumulated in the QW at low temperatures.

Knowing the absorption coefficient of the light in the material, the current (density) I can be written as:

$$I = eN_0S(1-e^{-\alpha d}) \tag{4.1}$$

where N_0 represents the number of incident photons per second and cm^2, S is the surface of the sample and $N_0\left(1-e^{\alpha d}\right)$ the number of electron-holes pairs generated per second in the non-doped region of thickness d.

The two recombination currents are not known exactly. To take them into consideration, two fitting parameters are introduced:

- the volume recombination current is written as a fraction $(1-a)$ from the photocurrent I ($0<a<1$);
- the surface recombination current is written as the fraction b from the thermionic current I_{th} that would pass over a Schottky barrier having the same height[64]. From the electrons in I_{th} only a fraction b recombine at the surface (this fraction is however expected to be important because for GaAs the surface recombination rate is high $S>10^6$ cm/s);

In quasi-equilibrium conditions under illumination, the photocurrent I is compensated by the sum of the recombination current I_r and the current bI_{th}. Under non-equilibrium conditions, the sum of these currents charges/discharges the capacity that exists between surface and substrate:

$$\frac{dQ}{dt} = I - I_r - bI_{th} = aI - bI_{th}, \quad Q = C \cdot U \tag{4.2}$$

Replacing the general expression for the thermionic current[64], the following equation is obtained:

$$\begin{aligned} -\frac{\varepsilon}{d}U'(t) = aeN_0(1-e^{-\alpha d}) - \\ bA^*T^2e^{-\frac{U_0}{U_T}}\left(e^{-\frac{U_0-U(t)}{U_T}}-1\right) \end{aligned} \tag{4.3}$$

where:

- e is the electron charge;
- ε is the dielectric constant;
- α is the absorption coefficient;
- A^* is the effective Richardson constant for thermionic emission;
- T is the temperature, $U_T = kT/e$, $U_0 = U(0) = 0.7$ V;

Here U is the potential difference between the surface and substrate. U_0 is the initial condition of the equation, the value of U before illumination. The photovoltage is then the difference $(U_0 - U)$. The first term on the right side of the equation gives the photocurrent, the second term the thermionic current. Their difference is equal to the current that charges the capacitor as expressed by Eq. (4.2).

As shown in the Appendix A, the dependence of the SPV signal on the temperature and light intensity is:

$$S_{PP} \propto \begin{cases} \dfrac{N_0 T_P}{4} & \textit{for small } (S_{PP} << U_T) \textit{ signal amplitude} \\ T \ln\left(\dfrac{N_0 T_P}{4U_T}\right) & \textit{for high } (S_{PP} > 3U_T) \textit{ signal amplitude} \end{cases} \tag{4.4}$$

Here S_{PP} is the photovoltage peak-to-peak signal and T_P is the period of the chopped light. The value of U_T is 6 mV at 70 K and 26 mV at 300 K. In the small signal limit, ($S_{PP} << U_T$) the signal is independent of temperature and proportional to the light intensity N_0. With an increasing signal, the dependence on temperature increases, and the dependence on light intensity decreases. For large signal ($S_{PP} > 3U_T$) the dependence on the light intensity is logarithmic and the dependence on the temperature is almost linear. The medium ($S_{PP} \approx U_T$) SPV signal has both the dependence on temperature and light intensity weaker than linear.

In Section 4.3 the SPV spectra will be discussed. They are recorded using chopped light at densities µW - tens of mW/cm^2. The SPV signal lies in the range of tens of µV - tens of mV. That represents, after the definition given by Eq. (4.4), a small to a large signal.

QW present

The case is discussed when the photon energy is less than the bandgap of the barrier (and substrate) material, so that the light is absorbed only in the quantum well. Under light absorption, carriers are generated in the QW. Carriers are present also outside QW: either by direct photo-excitation in the barriers[65] or by thermal escape and tunneling (or a combination of the last two)[66]. For the case presented in Fig. 4.4, the voltage across the structure is given by the following relation:

$$\begin{aligned} &U = Q_1 \frac{d_1}{\varepsilon_S} + Q_2 \frac{d_2}{\varepsilon_S} + \frac{Q_3 + Q_4}{2} \frac{x}{\varepsilon_{QW}}, \\ &Q_1 + Q_3 = Q_2 + Q_4, \quad Q_1, Q_2, Q_3, Q_4 > 0 \end{aligned} \tag{4.5}$$

Here d_1 is the distance between the surface and QW, d_2 the distance between the QW and the substrate, ε_S and ε_{QW} are the dielectric constants of the substrate and

QW materials, respectively. Because there is an electric field in the QW, the electrons and holes wave functions are not centered in the same place; x is this effective distance of separation of electrons and holes in QW. $Q_1 - Q_4$ are *excess* charges that appear under illuminations, compared to the equilibrium situation. Q_1 and Q_3 are excess hole-charges; Q_2 and Q_4 are excess electron-charges. All electrical charges are considered positive. $Q_1 + Q_3$ must be equal to $Q_2 + Q_4$ because the total charge is conserved.

The main contribution to the PV signal comes from the carriers outside QW, because they can separate in the built in electrical field over longer distances. Let's estimate the PV signal, if $Q_1 = Q_2 = 0$ is assumed. Considering a light intensity of 10 μW/cm^2, which corresponds to ≈10^{14} photons/cm^2×s, and a QW-absorption of $\alpha d \approx 0.01$, the generation rate G is 10^{12} electron-hole pairs/cm^2×s. Taking a typical recombination time $\tau = 1$ ns, the number of electron-hole pairs under illumination is $N = G\tau = 10^3$ /cm^2, which gives $Q_3 = Q_4 \approx 10^{16}$ C/cm^2. Taking the separation $x \approx 1$ nm, a photo-voltage $Q_3(x/\varepsilon)$ of the order of magnitude of fV results, too small to be measured.

As a conclusion the PV spectrum of a QW structure in the energy region under the band gap of the substrate is a product of two functions: (1) the absorption in the QW as a function of energy and (2) a function describing the escape of carriers from the quantum well and separation in the electric field. The second function is strongly dependent on temperature. Then based on Eq. (4.5), the PV signal can be written as:

$$PV \approx \alpha_{QW}(E) \times \left[f_e(E,T) d_2 + f_h(E,T) d_1 \right] \tag{4.6}$$

where $f_e(E,T)$ and $f_h(E,T)$ are the escape efficiency of the generated electrons respective holes from the QW followed by further separation in the electric field over the distances d_2 respective d_1 and $\alpha_{QW}(E)$ is the QW absorption coefficient.

4.2.5. Photovoltage time-transients

In order to compare the model presented above with the experiment, measured and calculated PV transients are plotted in Fig. 4.5. The transients were measured at three light intensities: I_0, $I_0/10^2$, and $I_0/10^5$. Here I_0 was chosen 20 mW/cm^2, T=77 K. The photon energies are above the band gap of the barrier, and in this case the presence of the QW does not influence the results. The calculated transients were obtained by replacing the values of the constants (ε_r for GaAs is 13.1, α is 4×10^4/cm at $\lambda = 632.8$ nm, $d \approx 300$ nm so that $\left(1 - e^{-\alpha d}\right)$ is taken 0.7 and $A^* \approx A/2$ for n-doped GaAs, $A = 120$ A·cm^{-2}·K^{-2}) in Eq. (4.3) and by varying the parameters a and b in order to obtain a higher amplitude (30% more) than the calculated transients (because only about 70% of the photovoltage generated in the sample is measured).

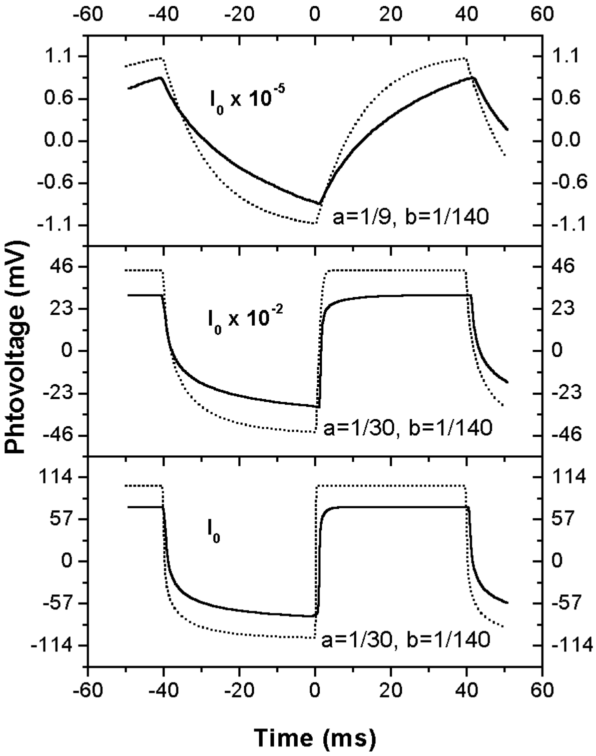

Fig. 4.5: Experimental (continuous line) and calculated (dashed line) photovoltage transients. A He-Ne laser (633 nm) was used as light source. I_0=20 mW/cm^2, T=77 K.

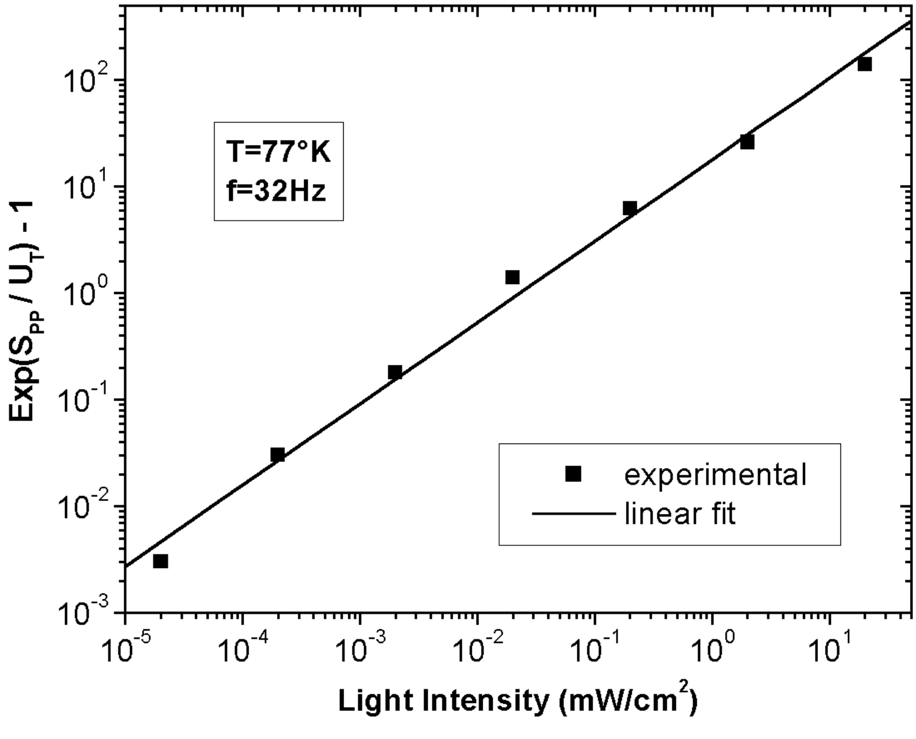

Fig. 4.6: The dependence of the SPV signal on the light intensity, at 32 Hz and 77 K.

The estimated a and b for the samples are mentioned in each case. As expected, the estimated a is smaller for larger light intensities, probably because now the volume recombination is more important (large carrier densities). The calculated waveforms are similar to the experimental ones: the falling front shows a slow tail. This confirms the validity of the model represented by Eq. (4.3). The PV transients measured for these samples show similarities compared to surface PV transients measured for other semiconductor structures[67].

In Fig. 4.6, the dependence of the peak-to-peak SPV signal on light intensity is plotted. As can be seen, the light-intensity dependence (Eq. (4.4)) is confirmed. Also the dependence with the temperature is confirmed: a signal of medium amplitude ($S_{PP} \approx U_T$) increases from 77 K to 300 K about 2 times. This confirms the validity of the model introduced in §4.2.4.

4.3. Experimental results

To record the spectra, a 100 W halogen lamp was used as light source followed by a Jobin-Yvon monochromator. The monochromatic light was mechanically chopped (80 Hz) and then projected uniformly on the sample (see Fig. 4.2). The area of the sample was about 1 cm^2.

4.3.1. Surface photovoltage spectra

In Fig. 4.7 the PV-spectra of the two type I QW-samples are represented, taken at three different temperatures. It is known from the literature[57, 54] that GaAs/InGaAs/GaAs and GaAs/InGaAsN/GaAs quantum wells are both of type I. Both samples show clearly 4 steps, enumerated from left (1) to right (4). The first step has the same position in energy like the photoluminescence (PL) and is identified as $e_1 - hh_1$ transition (Fig. 4.8). The last step is clearly due (note its energy-position) to photo-excitation of the GaAs barriers. The steps 2 - 4 are attenuated with increasing temperature in both samples.

The second and third steps have very different strengths in the two samples. While in the InGaAsN sample these are very clear (an increase in the SPV of about ten times at 70 K), for the InGaAs sample they are not so significant. There are two more obvious differences between the two samples: (a) the first step is sharper in the InGaAs sample and (b) the InGaAs sample shows exciton-like enhancements associated with steps 1 - 3. This can be correlated with the PL measurements (Fig. 4.8).

The PL-peak full width at half maximum (FWHM) for the InGaAsN sample is three times larger than for the InGaAs sample (see Table 3.1). The difference in step sharpness and exciton enhancements in the two samples can be explained by the difference in QW-homogeneity (see the discussion in §3.2.3). The fact that the first step is associated with an excitonic peak in the InGaAs sample confirms the validity of Eq. (4.6), as seen next.

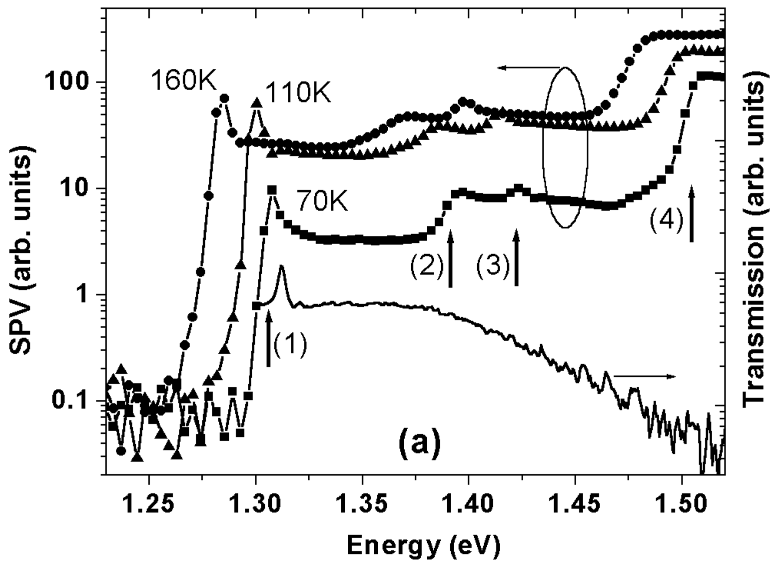

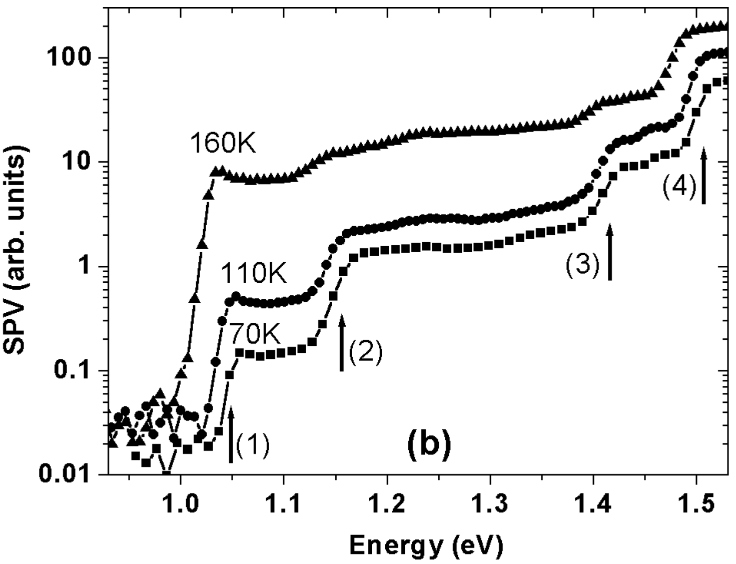

Fig. 4.7 (a) and **(b)**: Photovoltage spectra of the InGaAs and InGaAsN samples taken at three temperatures. For the InGaAs QW, the transmission spectrum for QW in-plane light propagation and perpendicular *E*-polarization is also shown.

4.3.2. Surface photovoltage generation mechanism

As explained above (see Eq. (4.6)), to account for the magnitude of the PV signal under illumination, it is necessary that excited carriers come through some mechanism out of the QW. As the photon energy is varied the SPV signal also varies, producing the steps seen in the spectra. Three such possible excitation-escape mechanisms have been identified:

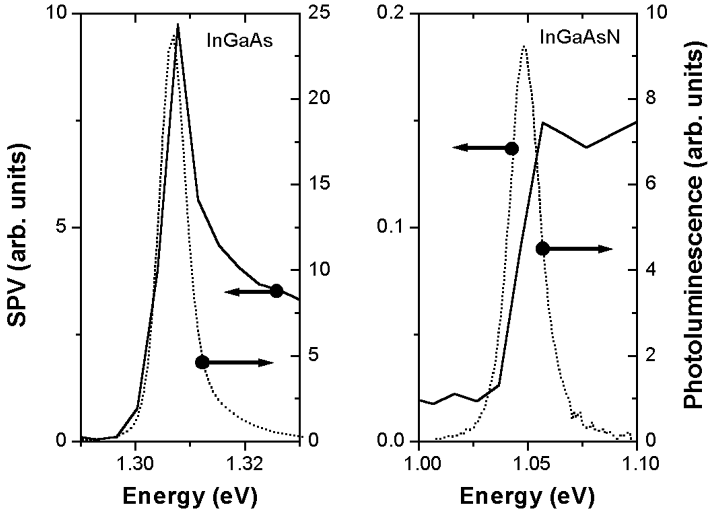

Fig. 4.8: Comparison between the photovoltage and photoluminescence spectra of the InGaAs and InGaAsN samples at 70 K.

(1) *transitions between confined states inside the QW (for example $e_2 - hh_2$), for* $k_{\|} = 0$. The carriers escape in this case from the QW because of the sufficient high temperature (thermal escape) or through tunneling. Contributions to the PV in this case are expected to come mainly from α_{QW} - term in Eq. (4.6). The terms f_e and f_h are expected to be independent of photon energy when only transitions between confined states are possible. The lifetime of the carriers in QW-confined, others than ground state, is far too small (≈10 ps) compared with that of the ground state (≈1 ns). So, the carriers relax firstly in the ground state and then escape from QW. Features in the SPV spectrum could be identified in this case with features in the absorption spectrum. The first step in the SPV spectra is associated with this type of transitions ($e_1 - hh_1$), as was discussed above;

(2) *transitions between confined states inside the QW (for example $e_1 - hh_1$) for* $k_{\|} \neq 0$. For sufficient high $k_{\|}$ and exciton life times, the electron and holes in confined states can have sufficient energy that, through elastic scattering processes, they escape out of QW (see Fig. 4.10);

(3) *transitions between confined and extended states (for example between hh_1 and extended electron states).* In this case carriers are directly excited in extended states out of QW (but there is the possibility that they are captured again in the QW). The terms $f_e(\hbar\omega, T)$ and $f_h(\hbar\omega, T)$ increase strongly (step-like) as a function of photon energy for sufficiently low temperatures, with the onset of confined-to-extended optical transitions. In this case it is expected a strong

increase in the SPV signal as a function of photon energy without a significant increase in the QW absorption;

Datta[68] *et al.* have identified the features in the SPV spectrum measured at room temperature with transitions between confined states in InGaAs single QW. The features present at low temperatures are not commented upon, except the ones related to the $e_1 - hh_1$ transition. On the other hand, Ksendzov[65] *et al.* have shown that transitions between confined states in InGaAs single QW and unconfined (continuum) states have comparable strength with transitions between confined states in QW. Calculations (using the multiband k·p method, see Fig. 4.9) of the confined electron and hole states for the InGaAs sample show that there are: (a) two confined electron levels e_1 and e_2, (b) three heavy-hole levels $hh_1 - hh_3$ and (c) no confined light hole state. For the InGaAsN sample no precise calculations can be performed because the material parameters are not well known, but there are expected more confined electron levels than in the InGaAs case, because with addition of nitrogen (1) the electron effective mass increases and (2) the conduction band offset strongly increases[54] (double as compared to InGaAs case).

Next, the three excitation-escape mechanisms mentioned above, and how they can explain the SPV spectra, are discussed.

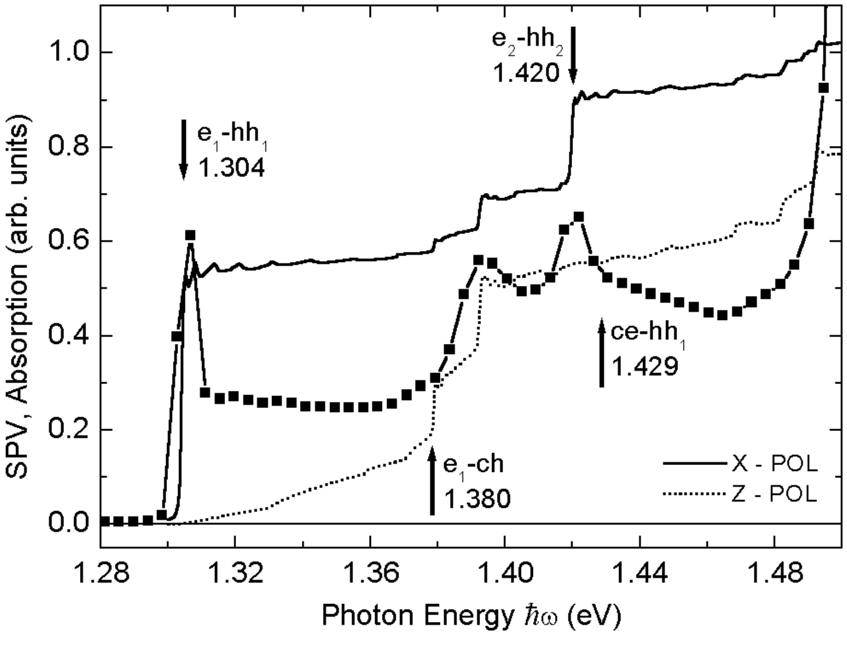

Fig. 4.9: Comparison of experimental and calculated (using multiband k·p method) InGaAs QW-absorption spectra for light propagation perpendicular (continuous line) and in the QW-plane with perpendicular *E*-field polarization (dotted line). The calculations were made for 22% In and 8.5 nm QW thickness. e_1-*ch* (*ce*-hh_1) arrows indicate the energy difference between the e_1 (hh_1) and the top (bottom) of the barrier valence (conduction) band.

Transitions between QW-confined states, $k_{\|} = 0$

To identify the role played by the confined states in the SPV generation, the absorption spectrum was theoretically calculated (using the multiband k·p method, without taking into consideration excitonic effects) in Fig. 4.9. Except $e_1 - hh_1$, there is only one allowed optical transition between confined states for the QW nominal parameters (20% In and 8 nm thickness), namely $e_2 - hh_2$, but this does not coincide with any of the steps 2 or 3 in the experimental spectrum. On the other hand, there is a very strong excitonic-like enhancement associated with the third step in the InGaAs sample, which *could* be associated with the $e_2 - hh_2$ exciton. To account for the possible dispersion in the QW parameters, these were slightly varied for the calculated absorption spectrum in Fig. 4.9 in order to make the calculated $e_2 - hh_2$ transition coincide in position with the third step in SPV spectrum. The parameters used in Fig. 4.9 are 8.5 nm (which corresponds to one monolayer change in thickness) and 22% In (a variation of 10% in the In composition). Only transitions between confined states in the QW cannot account for both the steps 2 and 3 seen in the spectra (see Fig. 4.9) because:

- for the InGaAs QW there is only one such allowed transition close to step 2 or 3, namely $e_2 - hh_2$;
- although the InGaAsN QW has very different parameters as compared to the InGaAs QW (and expected to have more confined electron levels than the InGaAs QW), both samples show 4 steps as main features in the spectra;
- the steps 2 and 3 in the InGaAsN spectrum (SPV increase: 10 times) are too large to come alone from the increase in α_{QW} due to optical transitions between confined states (see Eq. (4.6)). There must be an important contribution from the f_e and f_h terms. But, as discussed before, this is unlikely if only transitions between confined states are considered;

Comparing the calculated absorption and measured InGaAs SPV spectra, one can conclude that (Fig. 4.9):

- the second step in the SPV spectrum coincides with calculated step in absorption coming from optical transitions between extended hole states and confined e_1 states. This fact is further confirmed experimentally by transmission measurements, done in attenuated total reflection (ATR) geometry. In Fig. 4.7 the transmission of the QW for the in-plane light propagation and perpendicular E-polarization is shown. In this case only optical transitions involving light holes are allowed[69]. One can see indeed that the transmission of the sample decreases, when the electron-light holes optical transitions become possible (photon energies larger than $e_1 - ch$);
- the interpretation of the third step in the InGaAs SPV spectrum is more difficult and cannot be made unambiguous. Indeed, it is possible that the third step comes entirely from the $e_2 - hh_2$ transition. But on the other hand, it can also

come from transitions between hh_1 confined states and extended electron states ($ce-hh_1$ transitions). The calculated absorption spectrum shows that the last transitions are not strong, however they can account for an increase in SPV signal due to terms f_e and f_h in Eq. (4.6);

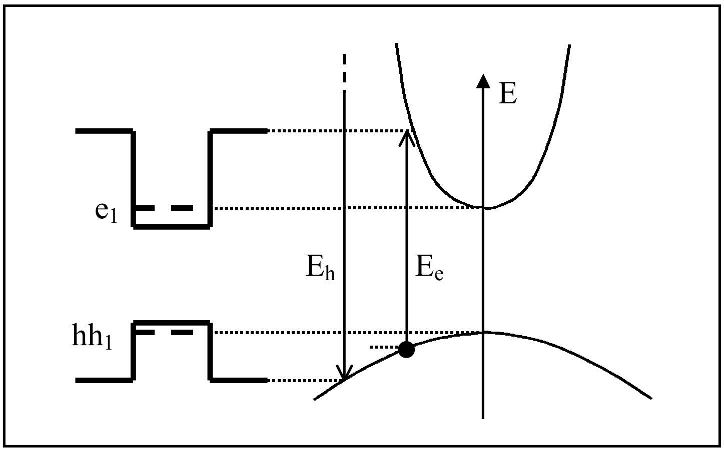

Fig. 4.10: Escape of carriers out of InGaAs QW through elastic scattering, after e_1-hh_1 optical excitation with $k_{\|} \neq 0$.

Transitions between QW-confined states, $k_{\|} \neq 0$

The absorption in QW contains at all energies above the e_1-hh_1 with $k_{\|}=0$ contributions from the e_1-hh_1 with $k_{\|} \neq 0$ (see Fig. 4.10). Through elastic scattering events, which are very frequent (the mean time between two such successive events is comparable with that of thermal relaxation), it is possible in principle that carriers come out of QW if they have sufficient kinetic energy. For the InGaAs QW sample, because the electron effective mass is much smaller than the heavy-hole mass, $E_h >> E_e$ (see Fig. 4.10). For reasonably small energies, only electrons can escape through elastic scattering out of QW. Then steps 2 and 3 in the spectrum might be in principle clarified by e_1-hh_1 and e_2-hh_2 transitions for $k_{\|} \neq 0$. However, this is not the case here because:

- according to calculations, the second step for InGaAs QW sample cannot be explained by any of e_1-hh_1 or e_2-hh_2 transitions for $k_{\|} \neq 0$ (see Fig. 4.9). Also, the third step should be higher in energy in order to be possible to assign it to the e_2-hh_2 transition (for $k_{\|} \neq 0$);
- the PV spectrum of the InGaAsN sample should show more step-like features, because there are more confined electron states as compared to the InGaAs QW sample;

Transitions between QW-confined and extended states

The third mechanism - transitions between confined and continuum states - can explain successfully the steps present in the SPV spectra. In the case of type I QWs there is a high probability of QW-(re)capture of the carriers in extended states[70] (times of capture of the order of tens of ps), so that actually not all the carriers excited in extended states become free by separation in the electric field. The following arguments show that the 4 steps seen in the InGaAsN sample can be explained by this excitation-escape mechanism:

- if the position of the steps 2 and 3 is identified with the energies $e_1 - ch$ and $ce - hh_1$ (see Fig. 4.9), then the distance between steps 1 and 2 should be equal with the distance between steps 3 and 4. This is indeed the case for both the InGaAsN and InGaAs QW samples. If the energy difference between e_1 (hh_1) and the bottom of the QW are known, the calculation of the band offsets is possible. These quantization energies are known for the InGaAs QW from the calculations. Taking the same values for the InGaAsN QW, the value of 79/21 results for the conduction/valence band ratio, in good agreement with other results from literature[54] (see also the Section 4.4);

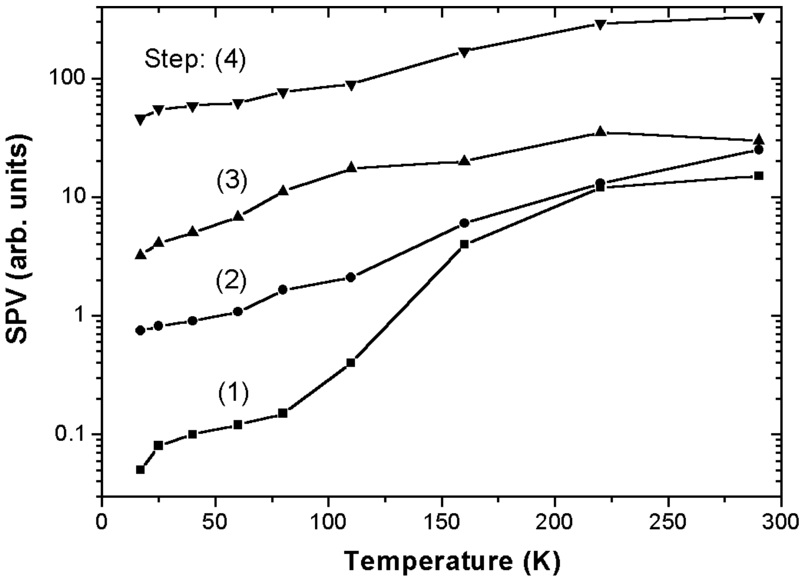

Fig. 4.11: Variation of the step 1 - 4 for the InGaAsN sample with temperature. The 4 steps are enumerated from left to right.

- to further clarify if this is indeed the main mechanism of carrier escape from the quantum well, in Fig. 4.11, the height of steps as a function of temperature for the InGaAsN sample are plotted. For step 4, the model presented in before predicts an almost linear dependence on temperature. The same must be essentially valid for the steps 2 and 3 because for both of them there is charge separation following direct excitation out of QW (transitions to extended states). On the other hand the first step must have a stronger dependence with the temperature, coming from two processes: (1) thermal activation of the carrier escape (exponential dependence with the temperature) and (2) the temperature dependence of steps 2 - 4. As can be seen in Fig. 4.11, steps 2 - 4 have similar temperature dependence. Step 1 has a much stronger temperature dependence especially for low temperatures;

- the calculations made for the InGaAs sample (Fig. 4.9) show that the positions of the steps 2 and 3 agree well with the $e_1 - ch$ and $ce - hh_1$ energies. But as discussed above, the third step cannot be assigned non-ambiguously. If the main contribution in the step 3 comes from $e_2 - hh_2$ transitions, this would explain why the (smaller in this case) contribution from the $ce - hh_1$ transitions is not clearly visible.

Influence of nitrogen on the conduction/valence bands in the InGaAsN material

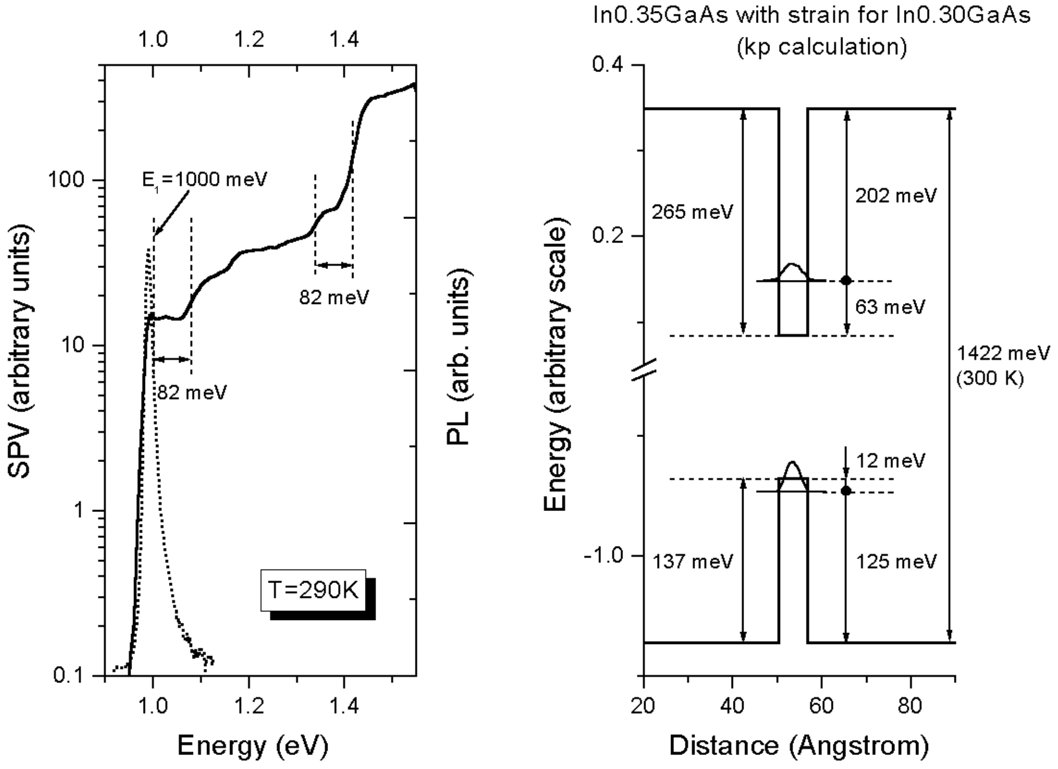

Fig. 4.12: The influence of the nitrogen on valence band maximum and conduction band minimum in strained $In_{0.35}Ga_{0.65}As_{0.983}N_{0.017}$ quantum wells. These are lowered by 138 and 43 meV, respectively.

Above, the conduction/valence band ratio of the InGaAsN QW-sample from the SPV spectrum was obtained. By comparing these results with calculation done for an appropriate InGaAs QW, the influence of nitrogen on the conduction and valence bands in strained InGaAs material can be determined. This comparison is shown in

Fig. 4.12. Incorporation of 1.7% N in strained $In_{0.35}Ga_{0.65}As$ QW influences the conduction and valence bands twofold by: (1) reducing the strain and (2) changing the intrinsic electronic properties of InGaAs material. To isolate the second contribution, the ground levels of a $GaAs/In_{0.35}Ga_{0.65}As/GaAs$ QW were calculated, by including the reduced strain present in the $GaAs/In_{0.35}Ga_{0.65}As_{0.983}N_{0.017}/GaAs$ QW. The calculations were done using the multiband k·p approximation. *By comparing the two results it is found that by adding 1.7% N in strained* $In_{0.35}Ga_{0.65}As$ *QW: (1) the energy of the valence band maximum is pushed down by approximately 125 - 82 = 43 meV and (2) the energy of the conduction band minimum is lowered as well by about [1422 - 82 - 1000] - 202 = 138 meV (see Fig. 4.12).* These calculations were done at room temperature.

4.4. Band offsets determination in type I quantum well structures. Band offsets determination in InGaAsN quantum wells

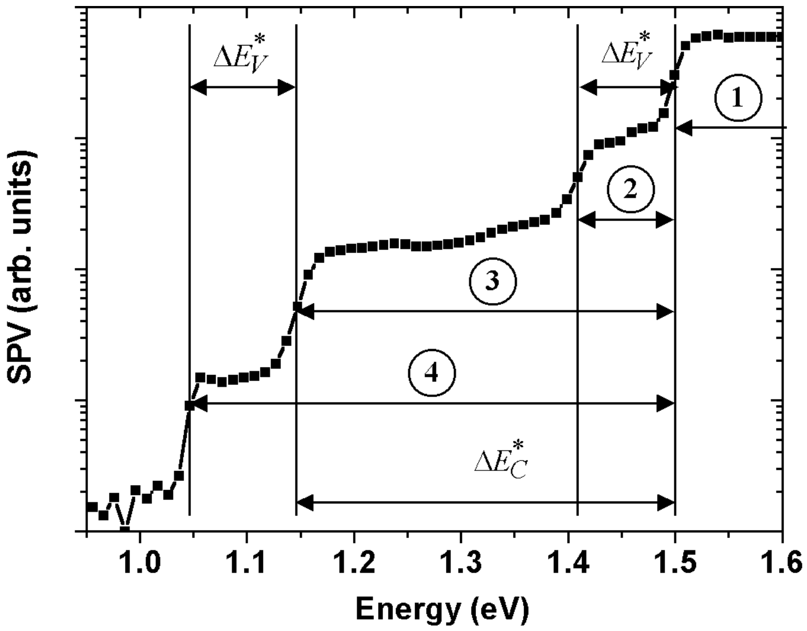

Fig. 4.13: SPV spectrum of the InGaAsN QW (type I) sample, taken at 77 K. On the figure the possible optical transitions (see Fig. 4.14) in every spectral region are indicated. The spectrum shows four steps as main features, enumerated in the text from left (1) to right (4) (and not marked on the figure for reasons of clarity).

In the previous discussion it was argued that the optical transitions between bound and continuum states in QW type I structures give the main features of the SPV spectrum: four steps (each corresponding to a tenfold increase in signal) at low temperatures (around 70 K) - see Fig. 4.13. These four steps correspond to the onset of one of the four possible optical transitions in the quantum well. These four types of optical transitions, represented schematically in Fig. 4.14, are: (1) transitions between extended (continuum) states, (2) transitions from QW-localized to extended states, (3) transitions from extended to QW-localized states and (4) transitions between the QW-localized states (the “extended” states are not localized in the quantum well but extended over the QW and barriers). For photon energies under 1 eV, none of these transitions are possible. By increasing the photon energy, the transitions (4), (3), (2), and (1) become successively possible and lead to an increase in the SPV signal. The spectral regions, where these four transitions are possible, are marked on Fig. 4.13.

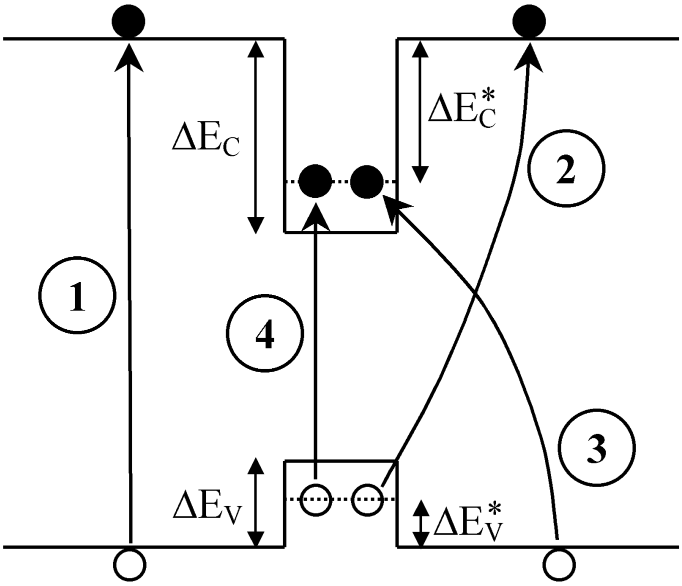

Fig. 4.14: Possible optical transitions in a QW of type I. Transitions of type (1) are between extended states; those of type (4) are between QW-localized states. The transitions of type (2) and (3) are between QW-localized and extended states.

Due to the role played by transitions between localized and extended states in SPV spectra, this method can be applied to determine the band-offsets of type I quantum wells. The distance in energy between steps 1 and 2 (1 and 3) is directly related to the valence (conduction) band-offset of the QW structure (see Fig. 4.13 and 4.14):

$$\Delta E_V^* = E_2 - E_1 = E_4 - E_3 = \Delta E_V - h_1$$
$$\Delta E_C^* = E_3 - E_1 = E_4 - E_2 = \Delta E_C - e_1$$

where h_1 (e_1) is the distance in energy between the first quantized hole (electron) level and the bottom of the quantum well. Here E_n is the position in energy of the n-th step. There is an information redundancy in the SPV spectra (which confirms the given interpretation): the energy distance between steps 2 and 1 (3 and 1) is equal to the energy distance between steps 4 and 3 (4 and 2) and equal to the $\min(\Delta E_V^*, \Delta E_C^*)$ ($\max(\Delta E_V^*, \Delta E_C^*)$). In our case, $\min(\Delta E_V^*, \Delta E_C^*) = \Delta E_V^*$, because $\Delta E_V^* < \Delta E_C^*$. To obtain the real value of the valence (conduction) band-offset, the energy of the first hole (electron) quantized level h_1 (e_1) must be known. h_1 and e_1 can be calculated if the effective masses of electrons and holes in QW as well as the form of the quantum well potential are known. However, the real band-offset values ΔE_V and ΔE_C are of interest only from a theoretical point of view. For the operation of a real device only ΔE_V^* and ΔE_C^* are of interest, because there are no other electron and hole energy levels lower than the ground state e_1 and h_1 levels, respectively.

For the InGaAsN QW-structure (Fig. 4.13), the values 100 and 353 meV are obtained for ΔE_V^* and ΔE_C^*, respectively. The effective masses are not exactly known for the InGaAsN material and no exact values for h_1 and e_1 can be calculated. If the values of a similar (see the previous paragraph) InGaAs-QW are taken (12 and 60 meV, respectively), the values 112 and 413 meV are obtained for ΔE_V and ΔE_C, respectively. This corresponds to a conduction/valence band ratio of 79/21. Note that in these calculations no excitonic effects are considered.

4.5. Band offsets determination in type II quantum well structures

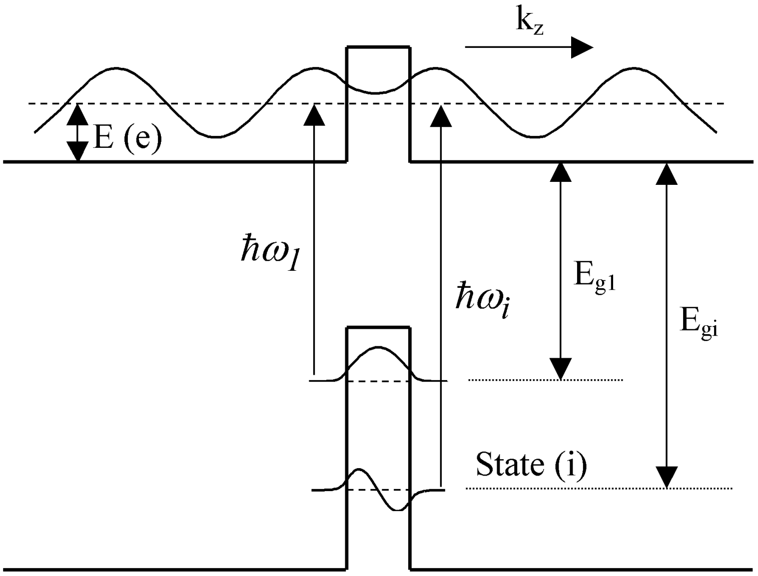

Fig. 4.15: In the case of a QW of type II, the transitions responsible for the SPV signal take place between QW-localized (state (*i*)) and extended states (with energy *E* above the barrier conduction-band minimum).

The SPV spectrum for a known type II[71] QW structure (GaAs/$GaAs_{0.7}Sb_{0.3}$/GaAs) is shown in Fig. 4.17. The spectrum looks completely different compared to that of a type I structure. There is only one clear step in the spectrum, corresponding to the barrier (GaAs) band gap. Even the first (left) step from Fig. 4.13, related to the band gap of the QW-material is not present: instead, there is a much slower exponential increase of the SPV signal (note that Fig. 4.17 is plotted in logarithmic scale). Such a slow exponential increase can be explained as follows, see Fig. 4.15: (1) all the optical transitions induced by photons with energies smaller than the barrier (GaAs) band gap are from bound to extended states and contribute similarly (compare with the type I case, where more types of optical transitions are possible) to the SPV signal, (2) the wave function penetration of the extended, conduction band states in the QW-region (which acts like a potential barrier) decreases exponentially with decreasing energy of the extended states (see also Appendix B). Consequently the overlap between a given QW-localized valence-band state and extended, conduction band states, depends exponentially on the energy of the extended states (for extended state energies lower than the barrier height represented by the QW potential). The energy interval of this exponential increase after the onset of the SPV signal must be directly linked to the conduction band offset.

As discussed before, at energies smaller than the band gap of the barriers, the SPV spectrum consists of a sum of contributions from optical transitions between quantized, QW-localized states and extended states (Fig. 4.15). The optical transition is of interband type (between valence and conduction band states):

$$SPV \propto \sum_i k_i(T)\,\alpha_i(\hbar\omega) \tag{4.7}$$

The coefficients $k_i(T)$ account for the separation of electrons and holes [see the discussion related to Eq. (4.6)]. The sum is over all the quantized, localized states (i) in the QW; $\alpha_i(\hbar\omega)$ is the absorption coefficient related to transitions taking place from the state (i) and for photon energy $\hbar\omega$. The k_i's are functions of temperature and give the contribution to the SPV signal from optical transitions involving the i-th state.

As shown in Appendix B, the derivative of the SPV signal with respect to energy, as obtained from the equation (4.7), is given by the following expression:

$$\frac{d(SPV)}{d(\hbar\omega)} \propto \sum_i k_i(T)\,E_{gi}\,m_r\sqrt{2m_e}\left|(\xi\vec{D})_i\right|^2 f_i^*(\hbar\omega - E_{gi}) \tag{4.8}$$

The value E_{gi} is defined in Fig. 4.15. The functions $f_i^*(E)$, depicted in Fig. 4.16 for a rectangular potential barrier of 50 meV depth, are peak-shaped. Eq. (4.8) shows that the derivative with respect to photon energy of the SPV spectrum should show a series of peaks (however, as seen from Fig. 4.16, the first is the most prominent). Each peak is amplified by the pre-factor $k_i(T)\,E_{gi}\,m_r\sqrt{2m_e}\,\left|(\xi\vec{D})_i\right|^2$, which depends on the reduced mass $m_r = \dfrac{m_e m_h}{m_e + m_h}$ (larger for heavy holes) and the interband dipole matrix element $\left|(\xi\vec{D})_i\right|^2$ (different for heavy and light holes).

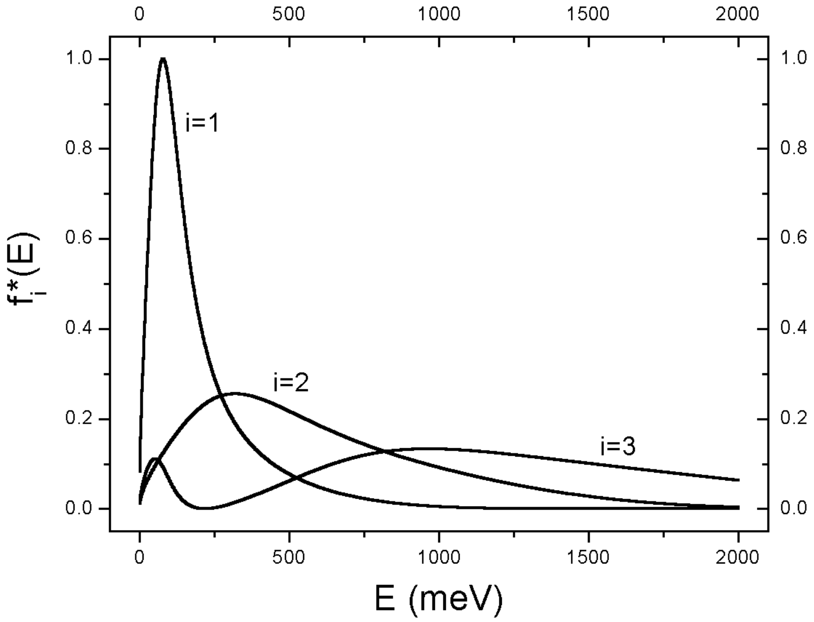

Fig. 4.16: Numerical calculations of the functions $f_i^*(E)$ (see Appendix B) for $\Delta E_C=50$ meV and for i=1, 2 and 3 (for negative values of the argument, the functions are identically zero).

In Fig. 4.17, the SPV spectrum taken at 77 K for the GaAsSb QW-structure is shown. The derivative of the spectrum is also represented in Fig. 4.17. A clear peak can be seen at low photon energies. This peak is identified as related to transitions between the QW-localized hole state $i=1$ and extended electron states, because it is the peak with the lowest energy. To calculate the conduction band offset, the value E_{g1} is needed. Unfortunately, E_{g1} cannot be assigned to the energy position of the PL-peak. As is well known for type II QW-structures, the PL-peak is strongly blue shifted by increasing the excitation intensity. The blue shift is caused by the band bending that appears as a result of the spatial separation of photo-excited electrons and holes[71, 72]. For photon energies below E_{g1}, a much faster increase of the SPV signal is expected, comparable to that of a type-I structure (see the left step in Fig. 4.13). This is actually not seen in Fig. 4.17, probably due to the very small SPV signal in this spectral region. E_{g1} must be smaller than E_{on} - the onset energy of the exponential part of the SPV spectrum in Fig. 4.17, that is, 926 meV. However, due to the very low excitation density used in taking the SPV spectrum (only a few µW/cm^2, which is at least 10^6 times less than typical densities used for PL) and taking into account the large energy difference (PL blue shift)[73] $E_{PL}-E_{on}=26$ meV, E_{g1} is approximated with E_{on} (≈926 meV). This approximation gives in the present case a PL blue shift of $E_{PL}-E_{g1}=26$ meV, which is consistent with similar results from the literature[73].

With E_{g1} known, the band offset can then be determined by finding the curve $i=1$ (fitting parameter is the band offset) in Fig. 4.16, which has a maximum at the energy

$\Delta E = E_{\max} - E_{g1}$. Here $E_{\max}$ (see Fig. 4.17) is the energy position of the first low-energy peak in the derivative of the SPV spectrum. $\Delta E = E_{\max} - E_{g1}$ can also be estimated directly from the SPV spectrum: it is roughly equal to the energy interval of exponential increase of the SPV signal (see Fig. 4.17). By fitting the maximum of the $i = 1$ transition (see Fig. 4.16) at the value $\Delta E = E_{\max} - E_{g1}$ = (1030 - 926) meV = 104 meV determined from experiment, a value of 81 meV results for the band offset of the conduction band. This value agrees well with values available in the literature[71, 73] for GaAsSb QWs with similar composition. By taking a heavy-hole effective mass[74] of $\approx 0.4 \times m_0$, the energy of the quantized heavy-hole ground level in the QW is $hh_1 \approx 20$ meV. This gives a valence band offset of $\Delta E_V = E_{g-GaAs} - E_{g1} + hh_1$, that is, (1500 – 926 + 20) = 594 meV and a conduction/valence band offset ratio of 12/88. For these calculations, a rectangular form of the QW-potential was assumed. The effective masses used in this calculation were obtained from those of GaAs and GaSb[74] by linear interpolation (the bowing parameter was assumed to be zero). If the exact form of the QW-potential is not exactly known, the procedure described in this paragraph can still give an estimation of the band offsets.

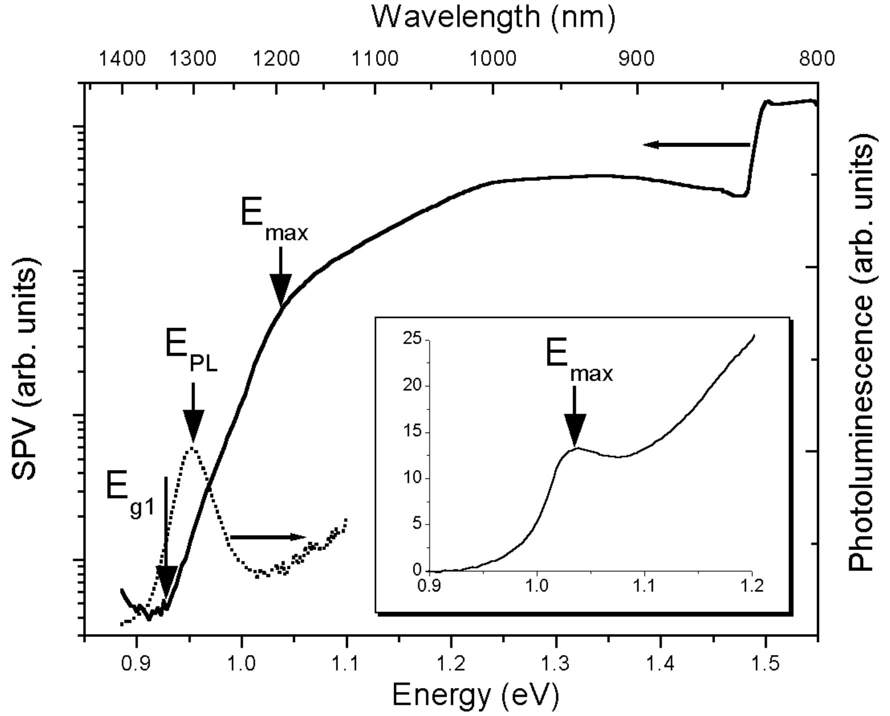

Fig. 4.17: SPV and PL spectra of the GaAs$_{0.7}$Sb$_{0.3}$ QW (type II) sample, taken at 77 K. In the inset, the derivative of the PV spectrum is shown. The energy values are E_{g1}=926 meV, E_{PL}=952 meV and E_{max}=1030 meV.

SPV measurements were done also on GaAsN QW-samples grown on GaAs substrates. The shape of the spectrum resembles the one in Fig. 4.17 (and not the one in 4.13), which indicates a type II band alignment (in the valence band) for the

GaAsN quantum wells grown on GaAs. $\Delta E_V \approx 40$ meV for GaAsN QW-samples containing ≈1% of nitrogen are obtained. This is consistent with the results obtained in Section 4.3, concerning the influence of nitrogen on the band offsets of InGaAsN quantum wells (the presence of nitrogen in InGaAs quantum wells pushes down the energies of both the conduction and valence bands). The absorption measurements performed in Chapter 3 also indicate a type II band alignment for GaAs/GaAsN/GaAs quantum wells (see Fig. 3.3 (b) and the discussion related to it).

Chapter 5
Transport properties

In this chapter, transport properties in InGaAsN QW-samples are studied by photocurrent and cyclotron resonance experiments. The possibility of charge transport along the QW-plane is explored by photocurrent experiments. By cyclotron resonance experiments, the measurement of effective electron/hole masses in InGaAsN is attempted.

5.1. Photocurrent measurements in quantum well samples

Purpose of these experiments is, to find out if in-plane transport of carriers *inside* the QW is possible. If strong potential fluctuations are present, no in-plane transport of carriers inside the quantum well should be possible. For homogeneous samples this question remains open. In this section, homogenous InGaAsN quantum wells are studied.

Description of experiment

The experimental setup was shortly explained in Section 2.5. For these experiments, contacts must be attached to the samples. The contacts were made by alloying small balls of pure indium on the sample (diffusion contacts) at a temperature of about 300 - 400°C. In this way the In diffuses and contacts the MBE-grown layer, which contains the quantum well. It is estimated that for contacts annealed at 460°C for 30 seconds, the In diffuses a few µm (≈10 µm) deep in the sample. In this case the substrate would be contacted too, fact that must be avoided in order to avoid measuring the photocurrent generated in the substrate. The contacts must be alloyed at a lower temperature, in order to contact only the MBE-grown layer. It is however impossible by this procedure to achieve exactly defined profiles of the contact.

In order to make sure that only the MBE-grown layer is contacted, the samples must have a special structure. The sample studied in this section was grown on SI-substrate and has the following structure:

- first a buffer layer (300 nm thick) was grown on the substrate;
- then a 1 µm-thick GaAs/AlAs barrier was grown as a superlattice (2.5 nm GaAs + 2.5 nm AlAs);
- three InGaAsN quantum wells, having a thickness of 5.5 nm, were grown in the middle of a 1 µm-thick GaAs layer. The barriers between the InGaAsN quantum wells are 25 nm-thick.

The thick GaAs/AlAs barrier is supposed to provide an electrical isolation between the substrate and the quantum wells. The sample is provided with contacts alloyed at low temperature, which diffuse only in the 1 µm-thick GaAs layer containing the quantum well.

In Fig. 5.1 the measured photocurrent spectra are shown. For comparison, the PL-spectrum is also plotted. The two photocurrent spectra were measured by scanning the spectral range in different directions.

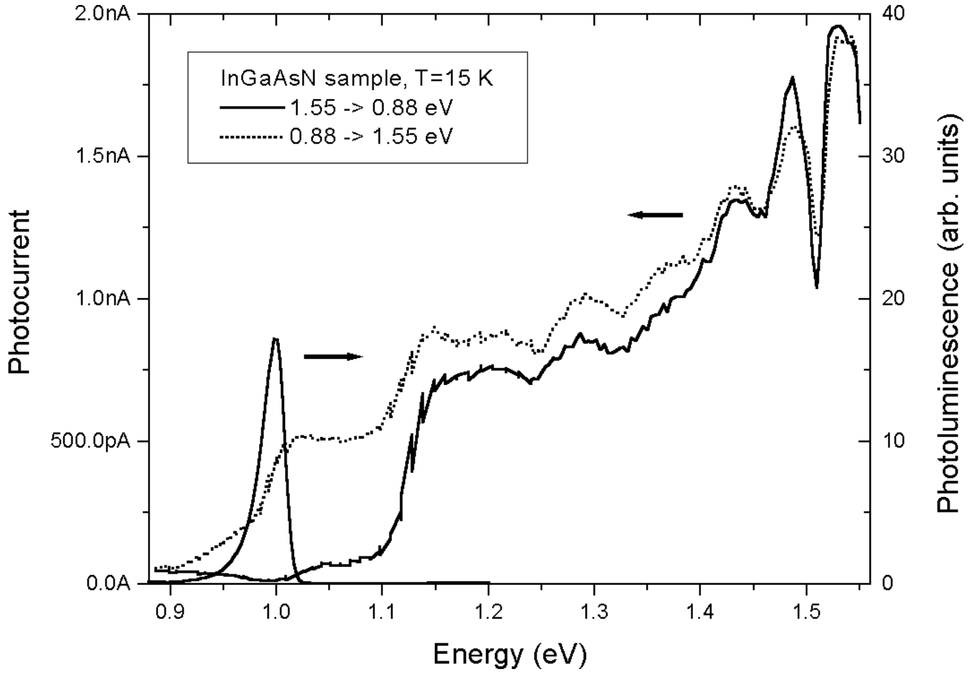

Fig. 5.1: Photocurrent spectrum measured on an InGaAsN QW-sample provided with flat contacts. One can see features similar with the surface photovoltage spectra measured in Chapter 4.

Discussion of results

As can be seen from Fig. 5.1, the AlGaAs barrier provides indeed a good electrical isolation between the contacted MBE-grown GaAs-layer and the substrate: the measured photocurrent is zero for photon energies under 0.9 eV, while for such photon energies large currents are measured in the substrate.

In photocurrent spectra one can see clear features, which come from optical transitions in quantum wells (compare with the PL-spectrum). The features seen in the PC-spectra resemble the ones seen in surface photovoltage (SPV) spectra [Fig. 4.7 (b)]. Due to the fact that the SPV and photocurrent spectra look similarly, it is sure that at least a part of the photo-generated electron-hole pairs follow paths outside the quantum well.

Additionally, the PC-spectra show a hysteresis effect: if the spectral range is crossed in different directions (1.55 → 0.88 eV and 0.88 → 1.55 eV), the spectra look differently. This effect is particularly strong in the spectral region between 1 and 1.1 eV, where only optical transitions between confined QW-states are possible. This fact again suggests that the path followed by the photo-excited carriers is not inside the quantum wells.

Conclusion

It is not sure that in-plane carrier transport *inside* the InGaAsN quantum wells is possible, even in homogenous InGaAsN quantum wells. The photocurrent experiments cannot differentiate between carrier transport inside and outside quantum wells.

5.2. Microwave absorption experiments

The experimental setup and basics about the principle of cyclotron resonance were shortly described in Section 2.5. Here, further details about the time-resolved microwave absorption experiments are discussed (see Fig. 5.2).

Microwave complex conductivity measurements of semiconductors have been done for more than three decades[75]. In 1969, Hartwig[76] *et al.* determined the change in time of the complex conductivity with a time resolution of one minute. Microwave reflection experiments[77] with a resolution of a few ns have been done in 1986. However, reflection experiments could not determine the contribution of the real and imaginary part of the conductivity. Grabtchak[78] *et al.* proposed in 1994 a method to measure the transient complex photoconductivity with a time resolution of 1 µs.

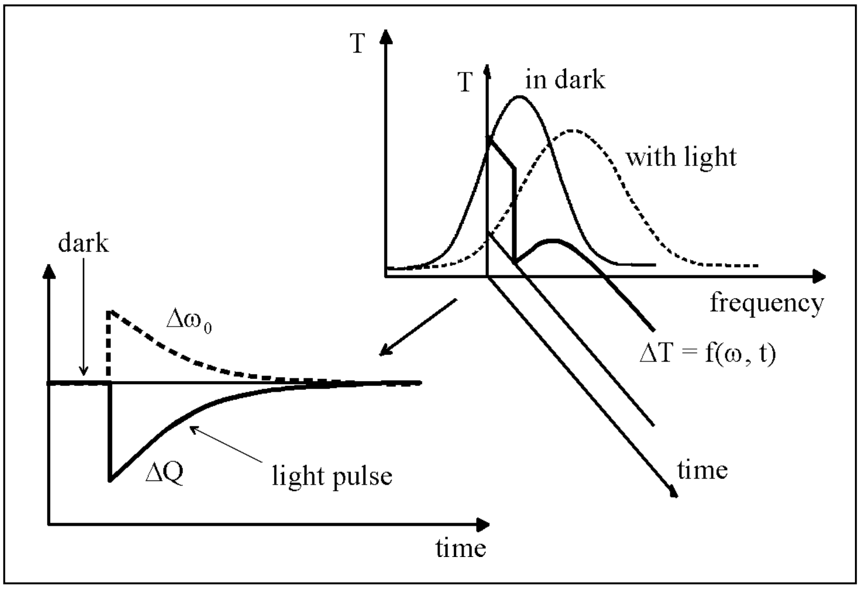

Fig. 5.2: Schematics of time-resolved microwave absorption experiments. *T* is the transmitted microwave signal through the microwave cavity (see Fig. 2.7), which contains the sample.

The signal T plotted in Fig. 5.2 is the transmitted microwave power through the cavity (which contains the sample, see Fig. 2.7) and has a resonance-like function of frequency, centered around the resonance frequency of the cavity (in TE_{011} mode). The quality (Q)-factor of the cavity is around 7000 at room temperature and 11000 at 4 K. The measurements are performed at minimum 7 K in order to avoid He-condensation in the cavity.

The measured quantities are the transients of the transmitted microwave signal through the cavity after applying a light pulse. Due to the photo-excitation of electron-hole pairs in the sample, the resonance frequency and the Q-factor of the cavity are modified. The transients are recorder for a number of circa 50 frequencies around the resonance. From these transients, the resonance curve is recovered as is represented schematically in Fig. 5.2 and, through a fitting procedure (the curve has a Lorentz shape), the Q-factor and the resonance frequency ω_0 of the cavity are determined as a function of the time delay after the light pulse. By defining $\Delta Q(t) = Q(t) - Q_{dark}$ and $\Delta\omega_0(t) = \omega_0(t) - \omega_{0-dark}$, the evolution in time of the complex dielectric function (composed from the dielectric constant and conductivity, see Eq. 5.2) is obtained:

$$\left.\begin{array}{l}\Delta\omega_0(t) = f(\Delta\sigma, \Delta\varepsilon) \\ \Delta Q(t) = g(\Delta\sigma, \Delta\varepsilon)\end{array}\right\} \Rightarrow \left\{\begin{array}{l}\Delta\sigma(t) \\ \Delta\varepsilon(t)\end{array}\right. \tag{5.1}$$

The functions f and g depend on the geometry of the sample and cavity. The calculation of the functions $\Delta\sigma(t)$ and $\Delta\varepsilon(t)$ is done in the frame of the theory of small perturbations of the cavity (the sample has a small size). In the frame of this theory, the relative change of the complex resonance frequency of the cavity and complex dielectric function is:

$$\begin{gathered}
\frac{d\omega^*}{\omega^*} \approx -\frac{d\varepsilon^*}{\varepsilon_0} \frac{\int\limits_{sample} E \cdot E^*}{\int\limits_{cavity} E \cdot E^*} = -\frac{d\varepsilon^*}{\varepsilon_0} \cdot G \\
\omega^* = \omega\left(1 + \frac{j}{2Q}\right) \Rightarrow \frac{d\omega^*}{\omega^*} = \frac{df}{f} + jd\left(\frac{1}{2Q}\right) \\
\varepsilon^* = \varepsilon_0\left(\varepsilon_r - j\frac{\sigma}{\omega\varepsilon_0}\right) = \varepsilon_0(\varepsilon_r - j\varepsilon_i) \Rightarrow \frac{d\varepsilon^*}{\varepsilon_0} = d\varepsilon_r - j\frac{\Delta\sigma}{\omega\varepsilon_0} \\
d\varepsilon_r \approx -\frac{1}{G}\frac{df}{f}, d\sigma \approx -\frac{1}{2G}\frac{dQ}{Q}\omega\varepsilon_0
\end{gathered} \tag{5.2}$$

The $\Delta\sigma(t)$ and $\Delta\varepsilon(t)$ functions are obtained with a time-resolution of about 100 ns, and are recorded as a function of the applied magnetic field (up to 1.4 T) in order to measure the cyclotron resonance in the samples.

5.3. Cyclotron resonance studies in InGaAsN samples

The cyclotron resonance (CR) is measured by using the time-resolved microwave absorption experiments described in the previous section.

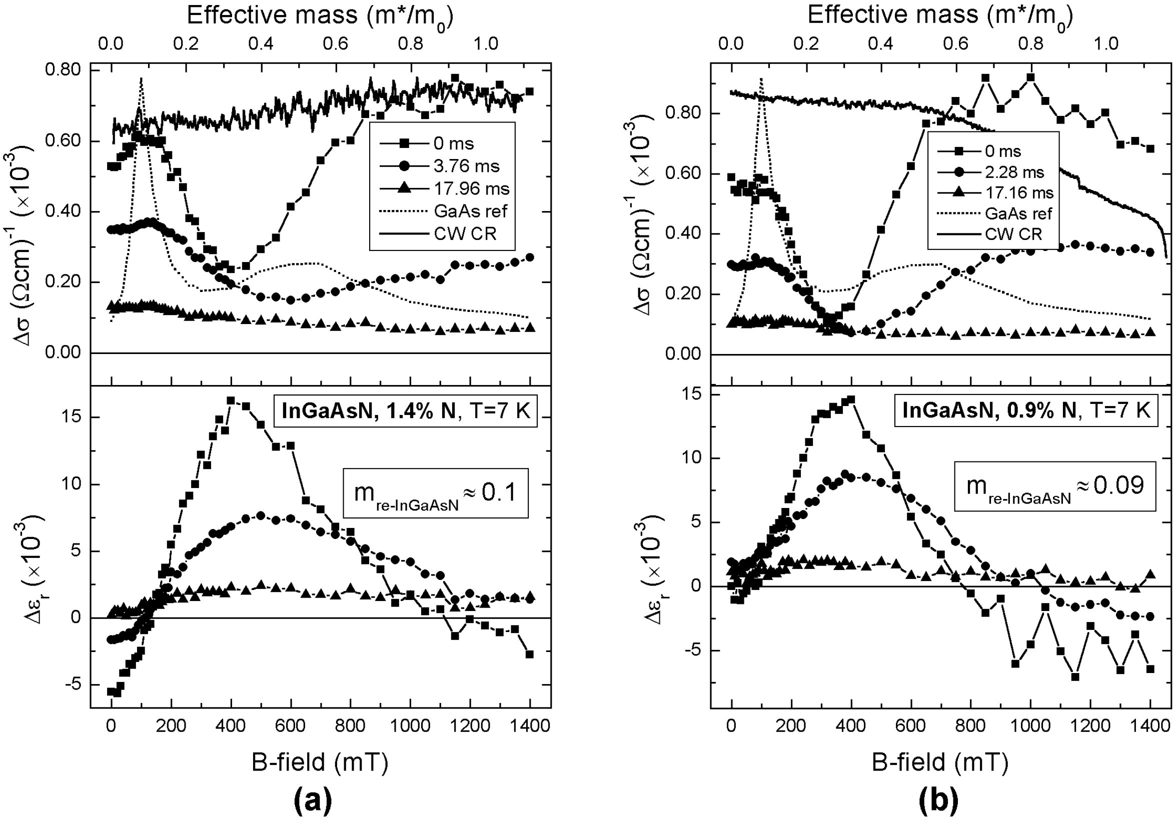

Fig. 5.3: Time-resolved microwave CR measured in InGaAsN 200 nm-thick layers. The N-composition is **(a):** 1.4%, **(b):** 0.9%. The samples were photoexcited with light pulses (905 nm, 12μJ, 150 ns). For comparison, the CR measured in a GaAs reference sample is plotted as well as the microwave continuous-wave (not time-resolved) CR. By fitting the CR-curves, the electron relative effective masses are estimated for the two samples at 0.1 and 0.09, respectively.

The samples were photoexcited with infrared light pulses (905 nm). The measurements were performed at 7 K.

The samples studied in this section have a structure similar to the one depicted in Fig. 2.2. Instead of quantum well(s), the samples contain 200 nm-thick InGaAsN-layers, lattice-matched to GaAs. In Fig. 5.3 (a) and (b) the results of cyclotron resonance measured in the two samples with a N-content of 1.4 and 0.9%, respectively, are presented.

During the carrying out of CR measurements, it was observed that also the GaAs-substrate responds to photo-excitation with photon energies under the GaAs band gap (due to ionization of band gap states). Due to this fact, in Fig. 5.4 (a) and (b) comparative measurements of the sample in Fig. 5.3 (a), which was gradually etched, are presented. In Fig. 5.4 (a), only the InGaAsN layer was etched off; the sample still contains the N-containing GaAs-barriers. In Fig. 5.4 (b), the whole MBE-grown layer was etched off; only the substrate was left.

Discussion of results

In Fig. 5.3 and 5.4 (b) (GaAs substrate), one can see two types of resonance:

- the normal cyclotron resonance, for small magnetic fields. In this case, the maximum of the $\Delta\sigma$-resonance curve is associated with an increase of the $\Delta\varepsilon_r$ (due to the Kramers-Kronig relations);
- a different type of cyclotron can be seen for higher magnetic fields. In this case, the maximum of the $\Delta\sigma$-resonance curve is associated with a decrease in $\Delta\varepsilon_r$.

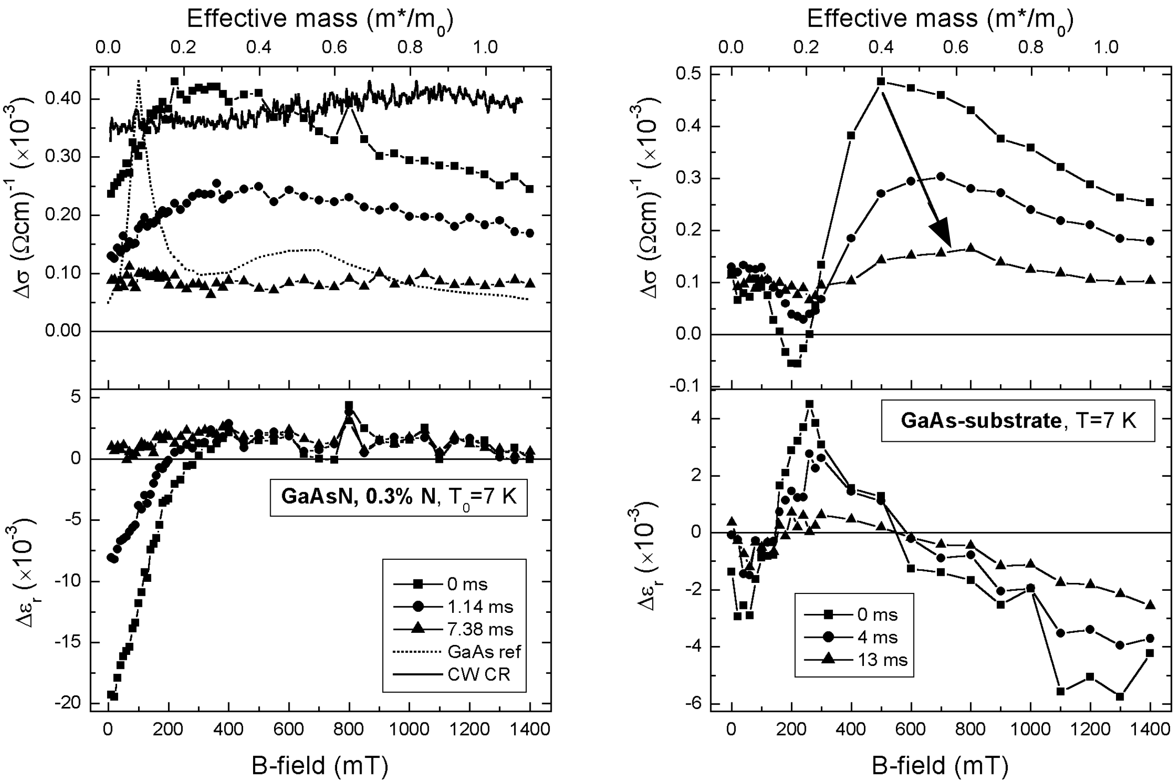

(a) (b)

Fig. 5.4: Microwave cyclotron resonance measured in the same sample from Fig. 5.3 (a), from which **(a)**: the InGaAsN was etched off, **(b)**: the whole MBE-grown layer was etched off. In case (a) the sample has still nitrogen in the GaAs-barriers. The samples were photoexcited with light pulses (905 nm, 12μJ, 150 ns). For comparison, in **(a)** the CR measured in a GaAs reference sample is plotted as well as the microwave continuous-wave (not time-resolved) CR. In **(b)**, the CR varies in time.

In Fig. 5.4 (b), the second resonance moves in time towards higher magnetic fields. The first resonance corresponds to the cyclotron resonance of the electrons in GaAs (with relative effective mass of 0.067).

In Fig. 5.4 (a), after etching off the InGaAsN-layer, none of the two resonances seen in Fig. 5.3 (a) can be seen.

Interpretation of results

The first resonance in Fig. 5.4 (b) corresponds to the electron cyclotron resonance. By fitting this curve, the effective mass in GaAs is obtained. *The second resonance* is interpreted as a charge-coupled (or Fano) cyclotron resonance[79] based on two facts: (a) strongly asymmetric curves and (b) a decrease in the $\Delta\varepsilon_r$. The shift in time observed in Fig. 5.4 (b) is associated with a coupling factor, which varies in time.

By comparing Fig. 5.4 (a) with 5.3, it is concluded that the two resonances seen in Fig. 5.3 come from the InGaAsN layer. Fig. 5.3 compares well with the substrate in Fig. 5.4 (b), consequently the first resonance in Fig. 5.3 is interpreted as the electron resonance in InGaAsN, the second resonance is interpreted as the a coupled electron-hole resonance in InGaAsN.

By fitting the first CR-curve in Fig. 5.3, an increased electron effective mass in InGaAsN is obtained as compared to GaAs. For Fig. 5.3 (a) (1.4% N) and 5.3 (b), a relative electron effective mass of 0.1 and 0.09 is obtained, respectively

The second CR-curve in Fig. 5.3 appears at higher magnetic fields than the corresponding curve in GaAs, see Fig. 5.4 (b). This indicates an increased heavy-hole mass in InGaAsN as compared to GaAs.

Conclusion

The measurements performed in this section indicate an increased electron mass in InGaAsN compared to GaAs. The obtained mass compare good with results from literature[58] and is in agreement with predictions of the theory (see for example [14] and references therein).

There is a second, coupled resonance visible in InGaAsN, which, if interpreted in the same way as the one seen in GaAs, indicates an increased heavy-hole mass in InGaAsN.

Summary

In this work the optical, electrical and transport properties of InGaAsN and GaAsN semiconductor alloys were studied. These alloys were grown on GaAs substrate by molecular beam epitaxy. The material was available either as quantum wells (layers up to about 10 nm thick) or as bulk (layers that are a few hundreds nm thick). The work is mostly experimental.

The main purpose of this work was to characterize the samples in view of the: (a) final device (vertical cavity surface emitting laser emitting at 1.3 µm), (b) improvement of the growth conditions, and (c) fundamental physical properties of N-containing materials InGaAsN and GaAsN. From the point of view of the laser, the samples must have a high optical quality, that is, good (intense and narrow) photoluminescence (PL) and low non-radiative recombination rates.

The N-content in the quantum well (or in the intentionally N-containing layers) can be precisely controlled. However, there is always some unwanted nitrogen in the adjacent regions (barriers) of the sample. The variation of the N-content in the growth direction was experimentally determined using etching techniques and confirmed by TEM images. To know the spatial distribution of the nitrogen is important for the correct interpretation of the measurements.

It is found that the InGaAsN quantum wells must be grown at low temperature (≈420°C), in order to reach a good homogeneity of thickness and composition. Due to this low growth temperature, the samples must be thermally annealed (at 720°C for about 15 minutes) in order to achieve high photoluminescence intensity and a better homogeneity of the samples.

The tuning of the quantum well parameters, in order to obtain high-quality growth of the quantum wells was done in two steps. First, *a coarse tuning* of the parameters was performed, by measuring the absorption of the quantum well samples. It was found that the quality of quantum wells decreases with increasing N- and In-content and that the barrier material has an important influence on the quality of quantum wells. The quality of the quantum wells decreases with increasing thickness. After thermal annealing the absorption of the samples decreases under the band-gap of the barrier-materials by a factor about two. *A finer tuning* of the quantum well parameters followed by performing photoluminescence experiments. The optimization was done for samples emitting around 1.3 µm. For a quantum well thickness of 6 - 7 nm was found an optimum of quantum well In- and N-composition at 35 and 1.7%, respectively.

After performing the photoluminescence experiments, a model for the photoluminescence mechanism in InGaAsN quantum wells, supported by transmission electron microscopy studies, was proposed. This model can explain important

features of the photoluminescence, like the temperature-behavior and the blue shift after thermal annealing. It cannot explain however the low photoluminescence intensity in some InGaAsN quantum wells.

The tuning of the growth temperature was studied in relation with carrier-localization effects in InGaAsN quantum wells. A simple relation was found: with increasing growth temperature, the carrier-localization effects become more important due to increasing inhomogenity of the quantum wells (thickness and probably compositions). The photoluminescence due to the recombination of localized carriers (the strongly localized photoluminescence) dominates in samples grown at high temperature.

Based on studies of the (time-resolved) photoluminescence in samples with different degrees of inhomogenity, it was found that the low photoluminescence intensity in InGaAsN samples is mainly due to two causes: (a) the carrier localization effects determine a long radiative life time of the carriers and because of that a low photoluminescence intensity, (b) low activation energy for the non-radiative recombination channels in InGaAsN, due to the presence of nitrogen. This explains the low photoluminescence intensity of InGaAsN quantum wells at room temperature, where short photoluminescence decay times of about 50 ps or less are measured.

In Chapter 4 a novel method, based on surface photovoltage, was developed, in order to measure the band offsets of quantum well (QW) structures (both for type I and II quantum well structures). This part of the work was motivated by the fact that the band alignment/offsets of InGaAsN and GaAsN quantum wells are not exactly known. A theoretical model is first presented, confirmed by experiments. The method is then applied to well known (InGaAs and GaAsSb) and new (InGaAsN, GaAsN) quantum well structures grown on GaAs substrates. The results obtained for the well-known structures compares well with results published in the literature. For InGaAsN quantum wells (emitting at 1.3 µm), a type I band alignment and band offset ratio of $\Delta E_C / \Delta E_V = 79/21$ was obtained. Measurements performed in GaAsN quantum wells containing about 1% nitrogen indicate a type II band alignment (quantum barrier in valence band), and band offsets of $\Delta E_V \approx 40$ meV. A type II band alignment in GaAsN quantum wells grown on GaAs is suggested also by absorption measurements performed in Chapter 3.

Concerning the fundamental properties of the InGaAsN, clear results were difficult to obtain, due to technological problems. However, some important results were achieved. By comparing calculated and experimentally measured band offsets of (high-quality) QW-structures with and without nitrogen, the influence of the nitrogen on the conduction band minima and valence band maxima was determined. It was found that by adding 1.7% N in $In_{0.35}Ga_{0.65}As$ quantum wells, these are lowered by 140 and 43 meV, respectively. This is a new result. Time-resolved microwave cyclotron resonance experiments indicate an increased electron effective mass in InGaAsN as compared to GaAs. For InGaAsN layers, lattice-matched to GaAs and containing 1.4% N, a relative electron effective mass of about 0.1 was obtained. The theoretical result, that by addition of nitrogen the effective mass of electrons increases, is confirmed. The cyclotron resonance experiments suggest also an increased effective heavy-hole mass in InGaAsN as compared to GaAs.

From the results obtained during this work, feedback was constantly supplied for improving the growth technology. During the period of time in which this work was going on, 1.3 µm laser emission from VCSELs was reached. Small threshold currents were obtained which promote these lasers among the best in the world.

Appendix A.
Temperature dependence of the SPV signal

To find the dependence of the solution of Eq. (4.3) on light intensity and temperature, Eq. (4.3) can be written in the form:

$$y'(t)=N(t)-c(T)\left(e^{\frac{y(t)}{U_T}}-1\right) \tag{A.1}$$

Here $y=U_0-U$ is the photovoltage, $U_T=kT/e$, and the coefficient $c(T)=\left(\frac{d}{\varepsilon}\right)bA^*T^2\left(e^{\frac{y(t)}{U_T}}-1\right)$. $N(t)$ is proportional to the light excitation (rectangular variation with period T_p):

$$N(t)=\begin{cases} N_0, & 0<t<\frac{T_p}{2} \\ 0, & \frac{T_p}{2}<t<T_p \end{cases}$$

The solution of Eq. (A.1) can be written as a sum between a transitory and a steady state, oscillatory solution: $y=y_{tr}+y_{ss}$. After long times, the transitory component becomes constant, $y_{tr}(t)=y_0$. We make the substitution $y\rightarrow y_0+y$ in Eq. (A.1) (now y is the steady-state solution) and we write the excitation $N(t)$ as a sum between an average and an alternative component: $N(t)=N_0\left(\frac{1}{2}+\xi(t)\right)$, with $\xi(t)$ varying between -1/2 and 1/2. We work in a temperature range where $c(T)$ ($c(T)$ decreases very fast with decreasing temperature) and consequently $e^{\frac{y_0}{U_T}}>>1$, so that:

$$\exp\left(\frac{y_0+y(t)}{U_T}\right)-1\approx\exp\left(\frac{y_0+y(t)}{U_T}\right)$$

Then the Eq. (A.1) becomes:

$$y'(t) \approx N(t) - c(T) e^{\frac{y_0 + y(t)}{U_T}} \tag{A.2}$$

For $\xi(t) = 0$ the steady-state component $y(t) = 0$ and the y_0 component is obtained:

$$0 = \frac{N_0}{2} - c(T) e^{\frac{y_0}{U_T}} \Rightarrow c(T) e^{\frac{y_0}{U_T}} = \frac{N_0}{2} \tag{A.3}$$

For constant light intensity N_0, because $c(T)$ decreases very fast with decreasing temperature, $e^{\frac{y_0}{U_T}}$ must increase very fast with decreasing temperature and the condition $e^{\frac{y_0}{U_T}} >> 1$ is satisfied for temperatures smaller than the room temperature. By replacing Eq. (A.3) in Eq. (A.2), an equation for the steady-state component is finally obtained:

$$y'(t) = N(t) - \frac{N_0}{2} e^{\frac{y(t)}{U_T}} = N_0 \left[\xi(t) - \frac{1}{2} \left(e^{\frac{y(t)}{U_T}} - 1 \right) \right] \tag{A.4}$$

Eq. (A.4) has an analytical solution. From this solution the peak-to-peak amplitude of the solution can be calculated. The result is:

$$S_{PP} = U_T \ln \left(\frac{1 + \frac{e^x}{e^x - 1}}{1 + \frac{x}{e^x - 1}} \right) \quad with \quad x = \frac{N_0 T_P}{2 U_T} \tag{A.5}$$

a) **for small signal**, $\frac{S_{PP}}{U_T} << 1$, $x << 1$ the Eq. (A.5) can be written in the form ($e^x - 1 \approx x$, $\ln(1 + x) \approx x$):

$$S_{PP} \approx U_T \ln \left(1 + \frac{x}{2} \right) \approx \frac{N_0 T_P}{4} \tag{A.6}$$

In this limit the photovoltage is independent of temperature and proportional to the light intensity.

b) **for large signal**, $\frac{S_{PP}}{U_T} > 3$, $x >> 1$, the Eq. (A.5) can be written in the form:

$$S_{PP} \approx U_T \ln\left(\frac{N_0 T_P}{2U_T}\right) \tag{A.7}$$

The dependence on temperature is (almost) linear, the dependence on light intensity logarithmic.

c) **for medium signal**, $\frac{S_{PP}}{U_T} \approx 1$, both the dependence on temperature and light intensity is weaker than linear [transition between the cases (a) and (b)].

Note that from Eq. (A.3) the y_0 component of the photovoltage has the following expression:

$$y_0 = U_0 - U_T \ln\left(2\frac{d}{\varepsilon} bA^* \frac{T^2}{N_0}\right) \tag{A.8}$$

and decreases with increasing temperature.

The lock-in does not measure the peak-to-peak photovoltage signal but the first harmonic of the photovoltage. A numerical calculation of the first-order Fourier coefficients confirms the results obtained above: in the range between T_1=50 K and T_2=300 K (T_2/T_1=6) the small signal ($\frac{S_{PP}}{U_T} << 1$) increases 1.016 times, the medium signal ($\frac{S_{PP}}{U_T} \approx 1$) increases two times, and the large signal ($\frac{S_{PP}}{U_T} \approx 6$) increases five times.

Appendix B.
Absorption coefficient for optical transitions in type II QW structures

The absorption coefficient due to phototransitions from the initial state $\langle j|$ can be written in the general form[80]:

$$\frac{\alpha_{\langle j|}(\hbar\omega)}{\omega} = const \times \int_f \left|\langle j \,|\, \vec{\xi}\,\vec{r} \,|\, f\rangle\right|^2 \delta(E_f - E_j - \hbar\omega)\left[G(E_f) - G(E_j)\right] \tag{B.1}$$

where $|f\rangle$ is the final state, $\left|\langle j \,|\, \vec{\xi}\,\vec{r} \,|\, f\rangle\right|^2$ is the optical transition matrix element and $G(E_j)$, $G(E_f)$ are the probabilities that the states $\langle j|$ and $|f\rangle$ are occupied by electrons. For the case of low temperatures (the initial state $\langle j|$ is in the valence band, while the final state $|f\rangle$ is in the conduction band), the functions $G(E_j)$ and $G(E_f)$ can be approximated by 1 and 0, respectively. In the following, it is supposed that the transitions take place from a QW-localized state in the valence band to a delocalized state in the conduction band, like in the case of a GaAsSb QW structure. It is assumed, for simplicity, that the conduction and valence bands are parabolic. The electron (hole) k-vector can be decomposed into two components: one perpendicular and one parallel to the QW-plane. As is well known, the in-plane component is conserved in optical transitions. To use this fact further, the following complete set of vectors is chosen for the initial and final states: $\langle j| = \langle k_{i,\|}, i|$ and $|f\rangle = |k_{f,\|}, k_z\rangle$, respectively. Here $k_{f,\|}$ and $k_{i,\|}$ are the electron and hole in-plane components of the k-vector, i represents the i-th quantized hole level, and k_z is the perpendicular component of the electron k-vector outside of QW (in the barriers). The matrix element for optical transitions between the initial and final states can then be written as:

$$\left|\langle k_{i,\|}, i \,|\, \vec{\xi}\,\vec{r} \,|\, k_{f,\|}, k_z\rangle\right|^2 \propto \delta_{k_{i,\|},k_{f,\|}} \left|\left(\vec{\xi}\vec{D}\right)_{j,f}\right|^2 F_i(k_z) \tag{B.2}$$

where $\left|\left(\vec{\xi}\vec{D}\right)_{j,f}\right|^2$ is the interband dipole matrix element, depending only on the bands to which the initial and final states belong (it is different for heavy as compared to light holes) and $F_i(k_z)=|\langle i,k_z\rangle|^2$ is the overlap of the z-axis components of the initial and final states. The delta function expresses the conservation of the in-plane k-component. In the following it is assumed that the final states belong to the same (conduction) band, so that $\left|(\xi\vec{D})_{j,f}\right|^2=\left|(\xi\vec{D})_i\right|^2$ (here i identifies different valence (sub-)bands, for example heavy and light holes). Under the assumption of parabolicity, Eq. (B.1) can then be written (the integration over the k_x and k_y disappears due to the δ-function in Eq. (B.2)):

$$\frac{\alpha_{\langle j|}(\hbar\omega)}{\omega}\propto\left|(\xi\vec{D})_i\right|^2\int dk_z\,\delta\left(E_{gi}+\frac{\hbar^2k_\|^2}{2m_h}+\frac{\hbar^2k_\|^2}{2m_e}+\frac{\hbar^2k_z^2}{2m_e}-\hbar\omega\right)F_i(k_z)$$

Here the $k_\|$ is the conserved in-plane component of the k-vector, E_{gi} is defined in Fig. 4.15, and m_e and m_h are the effective electron and hole masses. To obtain the absorption for the transitions from the quantized i-level, one must integrate over the k_x and k_y of the initial state:

$$\begin{aligned}\frac{\alpha_i(\hbar\omega)}{\omega}&\propto\left|(\xi\vec{D})_i\right|^2\int d^3k\,\delta(E_{gi}+\frac{\hbar^2k_\|^2}{2m_r}+\frac{\hbar^2k_z^2}{2m_e}-\hbar\omega)F_i(k_z)=\\&\left|(\xi\vec{D})_i\right|^2\int dk_xdk_ydk_z\,\delta(E_{gi}+\frac{\hbar^2k_x^2}{2m_r}+\frac{\hbar^2k_y^2}{2m_r}+\frac{\hbar^2k_z^2}{2m_e}-\hbar\omega)F_i(k_z)\end{aligned}\tag{B.3}$$

Here $m_r=\dfrac{m_em_h}{m_e+m_h}$ is the reduced electron-hole mass.

The last integral in Eq. (B.3) can be calculated by converting to cylindrical coordinates $(k_x=r\cos\varphi,k_y=r\sin\varphi,k_z)\to(r,\varphi,k_z)$, $dk_x\,dk_y\,dk_z=r\,dr\,d\varphi\,dk_z$:

$$\begin{aligned}&\int_{-\infty}^{\infty}dk_z\int_0^{2\pi}d\varphi\int_0^{\infty}dr\cdot r\cdot\delta(E_{gi}+\frac{\hbar^2r^2}{2m_r}+\frac{\hbar^2k_z^2}{2m_e}-\hbar\omega)\cdot F_i(k_z)=\\&2\pi\int_{-\infty}^{\infty}dk_z\cdot F_i(k_z)\cdot\int_0^{\infty}dr\cdot r\cdot\delta(\frac{\hbar^2r^2}{2m_r}-(\hbar\omega-E_{gi}-\frac{\hbar^2k_z^2}{2m_e}))=\\&2\pi(\frac{\sqrt{2m_r}}{\hbar})^2\frac{\sqrt{2m_e}}{\hbar}\int_{-\infty}^{\infty}dk_z\cdot F_i(\frac{\sqrt{2m_e}}{\hbar}k_z)\cdot\int_0^{\infty}dr\cdot r\cdot\delta(r^2-(\hbar\omega-E_{gi}-k_z^2))=\\&\frac{2\pi}{\hbar^3}\left(m_r\sqrt{2m_e}\right)\int_{-\infty}^{\infty}dk_z\cdot F_i(\frac{\sqrt{2m_e}}{\hbar}k_z)\cdot\sigma\left(\hbar\omega-E_{gi}-k_z^2\right)\propto\end{aligned}$$

$$\left(m_r\sqrt{2m_e}\right)\int_{-\sqrt{E}}^{\sqrt{E}} dk_z \cdot F_i\left(\frac{\sqrt{2m_e}}{\hbar}k_z\right) = \left(m_r\sqrt{2m_e}\right)\int_0^E \frac{de}{\sqrt{e}} \cdot F_i\left(\frac{\sqrt{2m_e e}}{\hbar}\right)$$

In passing from second to third integral the change of variables $(\frac{\hbar^2 r^2}{2m_r} \to r^2, \frac{\hbar^2 k_z^2}{2m_e} \to k_z^2)$ were made. In the third integral, the $\int_0^\infty dr \cdot r \cdot \delta(r^2 - a) = \frac{1}{2}\sigma(a)$ and $\delta(r^2 - a) = \delta(a - r^2) = \frac{1}{2\sqrt{a}}\delta(\sqrt{a} - r) + + \frac{1}{2\sqrt{a}}\delta(\sqrt{a} + r)$ relations were used (σ is the unit step function). In the fifth integral, $E = \hbar\omega - E_{gi}$ was defined and the fact that $F_i(x) = F_i(-x)$ was used. Finally, in passing from the fifth to the last integral, the change of variable $k_z \to \sqrt{e}$ was made.

By defining $F_i^*(e) = F_i(\frac{\sqrt{2m_e e}}{\hbar})$, Eq. (B.3) can be finally written in the form:

$$\frac{\alpha_i(E_{gi} + E)}{E_{gi} + E} \propto m_r\sqrt{2m_e}\left|(\vec{\xi}\vec{D})_i\right|^2 \int_0^E de \frac{F_i^*(e)}{\sqrt{e}} \tag{B.4}$$

$F_i^*(e)$ is the matrix element for optical transitions to final states with energy e above the bottom of the conduction band, see Fig. 4.15. By deriving the Eq. (4.7) with respect to photon energy, and using Eq. (B.4), the complete Eq. (4.8) is obtained:

$$\frac{d(SPV)}{d(\hbar\omega)} \propto \sum_i k_i(T)\frac{d\alpha_i(\hbar\omega)}{d(\hbar\omega)} = \sum_i k_i(T)\frac{d\alpha_i(E + E_{gi})}{d(E)} =$$

$$\sum_i k_i(T)\, E_{gi}\frac{d}{dE}\left(\frac{\alpha_i(E + E_{gi})}{E_{gi}}\right) \approx \sum_i k_i(T)\, E_{gi}\frac{d}{dE}\left(\frac{\alpha_i(E + E_{gi})}{E + E_{gi}}\right) \propto$$

$$\sum_i k_i(T)\, E_{gi}\, m_r\sqrt{2m_e}\left|(\vec{\xi}\vec{D})_i\right|^2 f_i^*(\hbar\omega - E_{gi})$$

Here the approximation $E + E_{gi} \approx E_{gi}$ was used, because $E << E_{gi}$. The functions $f_i^*(e)$ are defined by:

$$f_i^*(e) = \begin{cases} \frac{F_i^*(e)}{\sqrt{e}}, \; for\; e \geq 0 \\ 0, \; for\; e < 0 \end{cases} \tag{B.5}$$

expressing the fact that in Eq. (4.8) for $\hbar\omega < E_{gi}$ the optical transitions cannot take place.

To proceed further, we calculate the functions $F_i^*(e)$, making use of the effective mass approximation. For this case, because the optical transitions are between the valence and conduction bands, $F_i^*(e)$ is given by the following expression[80]:

$$F_i^*(e) = \left| \int dz \, \chi_{hole,\,i}(z) \, \chi_{electron,\,e}(z) \right|^2 \tag{B.6}$$

where $\chi_{hole,i}(z)$ and $\chi_{electron,e}(z)$ are the envelope functions of the localized hole state (i) and the extended electron state with energy e, respectively.

The functions $\frac{F_i^*(e)}{\sqrt{e}}$ were calculated numerically from Eq. (B.6) for the situation represented in Fig. 4.15. The result is shown in Fig. 4.16 for the first three localized hole states ($i = 1, 2, 3$) ($i = 1$ corresponds to the state closer in energy to the bottom of the quantum well). Fig. 4.16 refers to the same hole type - heavy or light. The calculations were done for a QW of 6 nm thickness, and for electron effective masses corresponding to the GaAs/GaAs$_{0.7}$Sb$_{0.3}$/GaAs material system (0.068×m_0 for GaAs, 0.045×m_0 for GaSb and 0.061×m_0 for the GaAs$_{0.7}$Sb$_{0.3}$)[74]. The effect of the built-in electrical field was neglected, because it is relatively small (≈1 V/µm, which corresponds to only 6 mV per 6 nm, the QW-width). The valence band offset used in calculations was $\Delta E_C = 50$ meV. As can be seen, the functions $\frac{F_i^*(e)}{\sqrt{e}}$ show a maximum, most pronounced for $i = 1$. The maximum becomes less pronounced and appears at higher energy as i increases. The maximum of the function $\frac{F_i^*(e)}{\sqrt{e}}$ for $i = 1$ was used in the text to determine the band offset of the type II QW structure.

Appendix C. Tables

1. *PL-parameters of samples with different N- and In-content*

Table 1. Different PL-parameters of the two series of QW-samples with different N- and In-content and different QW thickness, studied in Section 3.3. In each cell, two values of the specified parameter are given, as indicated in the brackets (and separated by slash). The units are also indicated (arbitrary units or meV). For example, in the first two lines the values of the parameter "maximum value of the PL-peak" are given at 77 and 300 K, in arbitrary units. The values in the fifth line are given for non-annealed/annealed (n/a) samples. The PL-shift with excitation power (lines 11 and 12) is measured between low (100 W/cm^2) and high (50 kW/cm^2) excitation densities.

		N-series (35% In) (3x6 nm)			In-series (1.7% N) (5x7 nm)			5x10nm 1.7 / 35
		1.1%	1.7%	2.3%	30%	35%	40%	
PL max. / exc. (77 / 300 K) (arbitrary units)	non-ann	1379 / 15.7	1187 / 15.7	719 / 3.06	578 / 1.14	566 / 7.76	526 / 1.53	184 / 2.42
	ann	2857 / 31.6	2785 / 34.9	1008 / 5.81	1836 / 6.42	9685 / 74.6	1290 / 8.02	2266 / 21
PL int. / exc. (77 / 300 K) (arbitrary units)	non-ann	40.4 / 0.78	84.8 / 0.904	73 / 0.36	41 / 0.11	24.8 / 0.393	28.4 / 0.12	7.14 / 0.14
	ann	57.5 / 1.18	115 / 1.74	62 / 0.74	82.7 / 0.42	194 / 2.72	54.7 / 0.46	49.7 / 0.88
PL max. 77 / 300 K (n / a) (arbitrary units)		87.8 / 90.4	75.6 / 79.8	235 / 173	507 / 286	72.9 / 130	344 / 161	76 / 108
PL int. 77 / 300 K (n / a) (arbitrary units)		51.8 / 48.7	93.8 / 66.1	203 / 83.8	373 / 197	63.1 / 71.3	237 / 119	51 / 56
PL-peak FWHM (meV)	77 K (n / a)	17.84 / 15.25	58.9 / 36.43	66.6 / 44.2	54.3 / 38.8	35.7 / 15.9	43.9 / 36.3	24.6 / 18.2
	300 K (n / a)	20.4 / 25.7	34 / 35.7	84 / 59.2	80.9 / 52.5	37.3 / 25.9	62.4 / 44.4	36.3 / 29.9
blue shift after annealing (77 / 300 K) (meV)		4.5 / 2.8	15.8 / 3.3	53.4 / 40.5	60.7 / 32.7	32.3 / 27.6	54.4 / 18.8	18.2 / 14.2
PL shift 77 - 300 K (n / a) (meV)		64.4 / 66.1	44.8 / 57.3	21 / 33.9	5.9 / 33.9	58.4 / 63.1	10.8 / 46.4	57.9 / 61.9
PL-shift with exc. (meV)	77 K (n / a)	-4.6 / -3.9	188.6 / 1.7	34.3 / 32.3	49.2 / 42.9	3.3 / 0.0	71 / 16.2	174.1 / 189.9
	300 K (n / a)	-14.4 / -15.3	-12.2 / -11.8	-10.4 / -0.8	-4.4 / -4.3	-16.2 / -11.4	-12.1 / -12.1	-12.1 / -13.4
PL-peak position (meV)	77 K (n / a)	1083.5 / 1088	1024.6 / 1040.4	912.1 / 965.5	983.6 / 1044.3	1031.7 / 1064	929.7 / 984.1	1009.7 / 1027.9
	300 K (n / a)	1019.1 / 1021.9	979.8 / 983.1	891.1 / 931.6	977.7 / 1010.4	973.3 / 1000.9	918.9 / 937.7	951.8 / 966

2. *PL-parameters of time-resolved measurements*

The first 7 entries in the tables refer to the time-evolution of the photoluminescence; the last 11 entries refer to the photon energy-evolution of the PL. The meaning of the notations is:

- $E_{\min}$, $E_{\max}$ (meV) are the minimum and maximum photon-energies for which the PL is monitored as a function of time;
- $\tau(E_{\min})$, $\tau(E_{\max})$ (ps) are the decay times of the PL at the photon energies $E_{\min}$ and $E_{\max}$, respectively. Fitting was made with one exponential decay whenever possible (one value of the decay time was given), otherwise fitting was made with two exponential decays (two values of the decay time were given);
- the next three entries give the maximum value of the PL as a function of time ($PL_{\max}$, in arbitrary units), the photon energy at which the maximum PL occurs ($E(PL_{\max})$, in meV), and the PL decay time ($\tau(PL_{\max})$, in ps) at this photon energy. Fitting was made with one exponential decay whenever possible (one value of the decay time was used), otherwise fitting was made with two exponential decays (two values of the decay time were used). This value of the decay time is taken as the PL decay time on the whole, because the maximum of the PL occurs at this photon energy;
- t_0 and $t_{\max}$ (ps) refer to the minimum and maximum times after the excitation pulse at which spectra were recorded, respectively;
- the values $Int(PL(t_0))$ [$Int(PL(t_{\max}))$], $E_c(t_0)$ [$E_c(t_{\max})$], $FWHM(t_0)$ [$FWHM(t_{\max})$], and $PL_{\max}(t_0)$ [$PL_{\max}(t_{\max})$] give the integrated PL (in arbitrary units), the energy position of the PL-peak (in meV), the full width at half maximum (in meV), and the absolute value of the PL-peak (in arbitrary units) at the time t_0 ($t_{\max}$), respectively;
- the ΔE_c value gives the shift of the PL-peak between t_0 and $t_{\max}$, in meV;

The parameters for the samples grown at 415, 432, and 453°C are given in Tables 2 to 5.

Table. 2. The parameters of the time-resolved PL-measurements for the 415°C-grown sample, non-annealed, barrier-excitation (495 nm)

T (K) →	10		30		50		70		100		170
P (mW) →	0.5	2.5	1	2.5	2.5	5	2.5	10	2.5	10	10
E_{min} (meV)	996	988	988	988	988	988	996	980	988	988	988
$\tau(E_{min})$ (ps)	4474	2289	5783	2888	387	454	118	225	110	80	57
E_{max}	1021	1038	1029	1029	1029	1038	1029	1047	1021	1056	1056
$\tau(E_{max})$	68, 651	32, 1129	40, 3035	48, 992	30, 155	33, 200	24, 123	26, 132	35, 233	33, 160	93
PL_{max} (a.u.)	4550	61700	12420	30005	48934	144E3	31227	207E3	13500	110E3	35700
$E(PL_{max})$	1008	1012	1012	1012	1012	1012	1012	1012	1010	1012	995
$\tau(PL_{max})$	975	157, 547	177, 1148	145, 665	67, 358	63, 289	45, 133	51, 227	47, 211	41, 175	57
t_0 (ps)	50	50	50	50	50	50	50	50	50	50	50
$Int(PL(t_0))$	99	1381	340	768	1197	3487	746	5311	388	3489	1108
$E_c(t_0)$	1010	1015	1012	1014	1013	1015	1012	1014	1010	1012	995
$FWHM(t_0)$	25	23	23	22	22	23	24	24	24	26	28
$PL_{max}(t_0)$	4000	53974	12067	29075	44036	128E3	25800	190E3	13230	115E3	32309
t_{max}	900	900	700	500	300	300	200	200	100	200	150
$Int(PL(t_{max}))$	59	390	127	249	189	370	138	499	152	242	197
$E_c(t_{max})$	1001	1005	1002	1002	1005	1005	1009	1010	1009	1009	992
$FWHM(t_{max})$	25	18	24	22	30	28	40	27	25	35	37
$PL_{max}(t_{max})$	2400	17513	5000	9392	6205	11000	3500	16493	5636	6500	5500
ΔE_c	9	10	10	12	8	10	3	4	1	3	3

Table. 3. The parameters of the time-resolved PL-measurements for the 415°C-grown sample, annealed, barrier-excitation (495 nm)

T (K) →	10		30		50		70		100		170	290
P (mW) →	0.5	2.5	0.5	2.5	0.5	2.5	1	5	1	2.5	10	10
E_{min} (meV)	1012	996	1012	1004	1004	996	996	988	1004	996	972	950
$\tau(E_{min})$ (ps)	2617	4664	1476	3052	520	711	1014	528	143	172	161	355
E_{max}	1038	1047	1038	1047	1038	1056	1038	1065	1047	1056	1093	1065
$\tau(E_{max})$	19, 181	19, 474	28, 537	20, 454	31, 399	9, 377	29, 213	201	162	125	112	214
PL_{max} (a.u.)	14303	180E3	8000	76500	13588	144E3	36E3	210E3	17200	62357	97100	12E3
$E(PL_{max})$	1021	1021	1021	1024	1024	1025	1023	1024	1018	1019	1004	965
$\tau(PL_{max})$	620	501	166, 1157	258, 764	71, 382	175, 562	143, 446	153, 600	117	105	101	207
t_0 (ps)	50	50	50	50	50	50	50	50	50	50	50	50
$Int(PL(t_0))$	311	2609	204	1570	284	3448	631	5234	431	1557	3379	960
$E_c(t_0)$	1023	1025	1024	1025	1022	1024	1023	1024	1020	1020	1002	962
$FWHM(t_0)$	21	21	20	19	21	20	21	22	21	21	29	48
$PL_{max}(t_0)$	12761	110E3	8340	71540	12E3	157E3	25424	210E3	16151	61071	93042	12790
t_{max}	900	900	900	900	300	700	300	500	200	300	200	100
$Int(PL(t_{max}))$	168	941	94	392	101	282	136	348	120	183	746	720
$E_c(t_{max})$	1013	1016	1012	1015	1019	1018	1020	1021	1018	1018	1001	961
$FWHM(t_{max})$	19	16	25	21	33	27	23	22	24	24	29	48
$PL_{max}(t_{max})$	7855	52E3	3415	16561	3750	10E3	5000	14E3	4215	5881	22047	9258
ΔE_c	10	9	12	10	3	6	3	3	2	2	1	1

Table. 4. The parameters of the time-resolved PL-measurements for the 415°C-grown sample, annealed and non-annealed, QW-excitation (990 nm)

T (K) P (mW) Sample	15 K, non-annealed		15 K, annealed		36 K, 272 mW		70 K, 272 mW		120 K, 272 mW		180 K, 520 mW	
	53 mW	272 mW	53 mW	272 mW	non-ann	ann	non-ann	ann	non-ann	ann	non-ann	ann
E_{min} (meV)	991	983	1000	983	991	991	983	991	975	983	967	975
$\tau(E_{min})$ (ps)	1346	977	15000	1313	673	728	267	291	100	212	100	185
E_{max}	1035	1026	1044	1044	1063	1063	1054	1063	1063	1044	1017	1082
$\tau(E_{max})$	51	28	58	59	52	66	59	79	89	107	40	90
PL_{max} (a.u.)	850	3614	3700	6074	9667	15200	8643	13487	6758	8483	2030	4900
$E(PL_{max})$	1012	1008	1020	1014	1020	1030	1017	1026	1008	1013	983	1000
$\tau(PL_{max})$	395	58	245	168	38, 181	242	47	200	45	165	47	171
t_0 (ps)	50	50	50	50	50	50	50	50	50	50	50	50
$Int(PL(t_0))$	20	81	84	178	338	537	319	537	160	361	111	303
$E_c(t_0)$	1013	1005	1024	1015	1019	1028	1017	1025	1005	1015	989	994
$FWHM(t_0)$	26	26	19	26	26	28	31	32	40	38	39	53
$PL_{max}(t_0)$	720	2721	3734	6160	9500	16324	7605	13812	5500	7416	2376	5419
t_{max}	700	600	800	800	300	900	300	700	150	400	100	400
$Int(PL(t_{max}))$	6	5	22	20	24	33	15	20	24	28	28	28
$E_c(t_{max})$	1002	989	1015	1003	1005	1017	1010	1018	1004	1012	988	994
$FWHM(t_{max})$	20	20	18	16	27	22	30	23	30	27	39	39
$PL_{max}(t_{max})$	320	282	1074	1050	778	1333	491	795	805	919	730	794
ΔE_c	11	16	9	12	14	11	7	7	1	3	1	0

Table. 5. The parameters of the time-resolved PL-measurements for the 432, 453°C-grown samples, annealed and non-annealed, barrier-excitation (495 nm)

T (K) P (mW) Sample	432°C 15 K 2.4 mW		432°C 35 K 5 / 3 mW		432°C 70 K 5 mW		432°C 120 K 5 mW		453°C annealed 2.4 / 5 mW	
	non-ann	ann	non-ann	ann	non-ann	ann	non-ann	ann	15 K	35 K
E_{min} (meV)	959	981	959	989	951	981	966	989	974	974
$\tau(E_{min})$ (ps)	2974	5381	1969	3674	421	570	97	115	2640	1240
E_{max}	1005	1030	1021	1038	1013	1047	1013	1056	1013	1021
$\tau(E_{max})$	43, 336	37, 267	29, 240	20, 276	42	96	39	106	62	21, 205
PL_{max} (a.u.)	20E3	74E3	38E3	62643	21E3	87E3	7100	32E3	3744	15E3
$E(PL_{max})$	989	1013	995	1013	990	1015	990	1010	997	997
$\tau(PL_{max})$	296, 1378	488	99, 473	327	55	137	40	92	304	78, 485
t_0 (ps)	100	100	50	50	50	100	50	50	50	50
$Int(PL(t_0))$	620	1782	1422	1729	676	2180	286	1069	138	627
$E_c(t_0)$	988	1012	995	1016	992	1016	993	1010	990	997
$FWHM(t_0)$	30	21	32	25	38	27	40	27	30	29
$PL_{max}(t_0)$	19655	74E3	40E3	57E3	15E3	70E3	6600	32E3	4200	18E3
t_{max}	900	900	900	900	200	700	100	300	300	900
$Int(PL(t_{max}))$	289	683	314	504	167	144	106	98	98	95
$E_c(t_{max})$	979	1005	977	999	965	982	980	1006	984	968
$FWHM(t_{max})$	36	20	39	24	43	39	45	43	30	30
$PL_{max}(t_{max})$	9012	29E3	9400	18349	4484	3000	2800	3365	3200	3800
ΔE_c	9	7	18	17	27	34	13	4	6	29

3. *Calculated PL-efficiency and radiative, non-radiative life times for the 415°C-grown sample (barrier excitation)*

Table 6. Thermally annealed sample

Temperature T (K)	**PL efficiency η_{PL}**	**PL decay time τ_{PL} (ps)**	**radiative life time τ_r (ps)**	**non-radiative life time, τ_{nr} (ps)**
10	0.87528	501	572	4017
30	0.42363	258	609	448
50	0.13005	175	1346	201
70	0.05782	153	2646	162
100	0.024	105	4375	108

Table 7. As-grown (non-annealed) sample

Temperature T (K)	**PL efficiency η_{PL}**	**PL decay time τ_{PL} (ps)**	**radiative life time τ_r (ps)**	**non-radiative life time, τ_{nr} (ps)**
10	0,3776	157	416	252
30	0,20598	145	704	183
50	0,06753	63	933	68
70	0,02079	51	2453	52
100	0,00662	41	6193	41

References

---

[1] H. Riechert, A. Ramakrishnan, and G. Steinle, Semicond. Sci. Technol. **17**, 892 (2002).

[2] M. Weyers, M. Sato, and H. Ando, Jpn. J. Appl. Phys., Part I **31**, 853 (1992).

[3] M. Kondow, T. Kitatani, S. Nakatsuka, M. C. Larson, K. Nakahara, Y. Yazawa, M. Okai, and K. Uomi, IEEE J. Select. Topics Quantum Electron., Vol. 3, No. 3, p. 719 (1997).

[4] S. Sakai, Y. Ueta, and Y. Terauchi, Jpn. J. Appl. Phys. **32**, 4413 (1993).

[5] L. Bellaiche, S.-H. Wei, and A. Zunger, Phys. Rev. B **54**, 17568 (1996).

[6] J. I. Pankove, IEEE J. Quantum Electron. **4**, 119 (1968).

[7] P. Y. Yu and M. Cardona, *Fundamentals of Semiconductors*, (Springer, Berlin, 1996), p. 7.

[8] R. Asomoza, V. A. Elyukhin, and R. Pena-Sierra, Appl. Phys. Lett. **81**, 1785 (2002).

[9] A. Zunger and S. Mahajan, in *Handbook on Semiconductors* (Elsevier, Amsterdam, 1994), Vol. 3, p. 1309.

[10] A.Yu. Egorov, D. Bernklau, B. Borchert, S. Illek, D. Livshits, A. Rucki, M. Schuster, A. Kaschner, A. Hoffmann, Gh. Dumitras, M.C. Amann, and H. Riechert, Journal of Crystal Growth 227-228, 545 (2001).

[11] H. P. Hjalmarson, P. Vogl, D. J. Wolford, and J. D. Dow, Phys. Rev. Lett. **44**, 810 (1980).

[12] X. Liu, M.-E. Pistol, L. Samuelson, S. Schwetlick, and W. Seifert., Appl. Phys. Lett. **56**, 1451 (1990).

[13] W. Shan, W. Walukiewicz, J. W. Ager III, E. E. Haler, J. F. Geisz, D. J. Friedman, J. M. Olson, and S. R. Kurtz, Phys. Rev. Lett. **82**, 1221 (1999).

[14] T. Mattila, Su-H. Wei, and A. Zunger, Phys. Rev. B **60**, R11245 (1999).

[15] P. R. C. Kent and A. Zunger, Phys. Rev. B **64**, 115208 (2001).

[16] P. R. C. Kent, L Bellaiche, and A. Zunger, Semicond. Sci. Technol. **17**, 851 (2002).

[17] K. Kim and A. Zunger, Phys. Rev. Lett. **86**, 2609 (2001).

[18] U. Tisch, E. Finkman, and J. Salzman, Appl. Phys. Lett. **81**, 463 (2002).

[19] S.-H. Wei and A. Zunger, Phys. Rev. Lett. **76**, 664 (1996).

[20] L. Grenouillet, C. Bru-Chevallier, G. Guillot, P. Gilet, P. Ballet, P. Duvaut, G. Rolland, and A. Million, J. of Appl. Phys. 91, 5902 (2002).

[21] V. Grillo, M. Albrecht, T. Remmele, H. P. Strunk and A. Yu. Egorov and H. Riechert, J. Appl. Phys. **90**, 3792 (2001).

---

[22] M. Albrecht, V. Grillo, T. Remmele, H. P. Strunk, A. Yu. Egorov, Gh. Dumitras, H. Riechert, A. Kaschner, R. Heitz, and A. Hoffmann, Appl. Phys. Lett. **81**, 2719 (2002).

[23] P. J. Klar, H. Gruening, J. Koch, S. Schaefer, K. Volz, W. Stolz, W. Heimbrodt, A. M. Kamal Saadi, A. Lindsay, and E. P. O'Reilly, Phys. Rev. B **64**, 121203 (2001).

[24] P. J. Klar, H. Gruning, L. Chen, T. Hartmann, D. Golde, M. Gungerich, W. Heimbrodt, J. Koch, K. Volz, B. Kunert, T. Torunski, W. Stolz, A. Polimeni, M. Capizzi, Gh. Dumitras, L. Geelhaar, H. Riechert, IEE Proceedings-Optoelectronics, **150**, 28 (2003).

[25] Sylvia G. Spruytte, Christopher W. Coldren, James S. Harris, William Wampler, Peter Krispin and Klaus Ploog, and Michael C. Larson, J. Appl. Phys. **89**, 4401 (2001).

[26] W. B. Jackson, N. M. Amer, A. C. Boccara, and D. Fournier, Applied Optics **20**, 1333 (1981).

[27] See for example: F. T. Vasko and A. V. Kuznetsov, *Electronic States and Optical Transitions in Semiconductor Heterostructures,* (Springer, New York, 1999), Chapter 2.

[28] E. Tournie, M.-A. Pinault, and A. Guzman, Appl. Phys. Lett. **80**, 4148 (2002).

[29] Y. P. Varshni, Physica (Utrecht) **34**, 149 (1967).

[30] L. Grenouillet *et al.*, Appl. Phys. Lett. **76**, 2241 (2000).

[31] M. A. Pinault and E. Tournie, Appl. Phys. Lett. **78**, 1562 (2001).

[32] S. Shirakata *et al.*, Appl. Phys. Lett. **80**, 2087 (2002).

[33] A. Polimeni *et al.*, Appl. Phys. Lett. **77**, 2870 (2000).

[34] H. P. Xin et al., Appl. Phys. Lett. **74**, 2337 (1999).

[35] B.V. Volovik et al., Semicond. Sci.Technol. **16**, 186 (2001).

[36] S. R. Jin *et al.*, J. Appl. Phys. **88**, 4075 (2000).

[37] R. A. Mair *et al.*, Appl. Phys. Lett. **76**, 188 (2000).

[38] A. Markus *et al.*, Appl. Phys. Lett. **80**, 911 (2000).

[39] C. Piermarocchi, F. Tassone, V. Savona, A. Quattropani, and P. Schwendimann, Phys. Rev. B **53**, 15834 (1996).

[40] K. Nakano, Y. Kishita, S. Itoh, M. Ikeda, A. Ishibashi, and U. Strauss, Phys. Rev. B 53, 4722 (1995).

[41] A. Zrenner, B. Fröhlich, J. Brunner, and G. Abstreiter, Phys. Rev. B **52**, 16608 (1995).

[42] B. Deveaud, F. Clerot, N. Roy, K. Satzke, B. Sermage, and D. S. Katzer, Phys. Rev. Lett. **67**, 2355 (1991).

[43] J. Martinez-Pastor, A. Vinattieri, L. Carraresi, M. Colocci, Ph. Roussignol, and G. Weimann, Phys. Rev. B **47**, 10456 (1993).

[44] J. P. Bergman, P. O. Holtz, B. Monemar, M. Sundaram, J. L. Merz, and A. C. Gossard, Phys. Rev. B **43**, 4765 (1991).

[45] P. Zhou, H. X. Jiang, R. Bannwart, S. A. Solin, and G. Bai, Phys. Rev. B **40**, 11862 (1989).

---

[46] G. Bacher, C. Hartmann, H. Schweizer, T. Held, G. Mahler, and H. Nickel, Phys. Rev. B **47**, 9545 (1993).

[47] G. Bacher, H. Schweizer, J. Kovac, A. Forchel, H. Nickel, W. Schlapp, and R. Lösch, Phys. Rev. B **43**, 9312 (1991).

[48] J. Ringling, Y. Kawamura, L. Schrottke, H. T. Grahn, K. Yoshimatsu, A. Kamada, and N. Inoue, Appl. Phys. Lett. **72**, 1620 (1998).

[49] Y.-H. Cho, G. H. Gainer, A. J. Fischer, J. J. Song, S. Keller, U. K. Mishra, and S. P. DenBaars, Appl. Phys. Lett. **73**, 1370 (1998).

[50] S.-W. Feng, Y.-C. Cheng, Y.-Y. Chung, C. C. Yang, Y.-S. Lin, C. Hsu, K.-J. Ma, and J.-I. Chyi, J. Appl. Phys. **92**, 4441 (2002).

[51] A. Kaschner, T. Luettgert, H. Born, A. Hoffmann, A. Yu. Egorov, and H. Riechert, Appl. Phys. Lett. **78**, 1391 (2001).

[52] A. Zunger, Phys. Stat. Sol. (b) **216**, 117 (1999).

[53] A. Yu. Egorov, D. Berklau, D. Livshits, V. Ustinov, Zh. I. Alferov, H. Riechert, Electronics Letters, Vol. **35**, No. 19, 1643 (1999).

[54] M. Hetterich, M. D. Dawson, A. Yu. Egorov, D. Berklau, H. Riechert, Appl. Phys. Lett. **76**, 1030 (2000).

[55] H. Kroemer, W. Y. Chen, J. S. Harris, D. D. Edwall, Appl. Phys. Lett. **36**, 295 (1980).

[56] H. Henrich, J. M. Langer, Festkoerperprobleme **XXVI**, p. 251 (1986).

[57] J.-P. Reithmaier, R. Höger, H. Riechert, A. Heberle, G. Abstreiter, G. Weimann, Appl. Phys. Lett. **56**, 536 (1990).

[58] I. A. Buyanova, G. Pozina, P. N. Hai, W. M. Chen, H. P. Xin, C. W. Tu, Phys. Rev. B **63**, 033303 (2000).

[59] E. O. Johnson, Phys. Rev. **111**, 153 (1958).

[60] H. C. Gatos, J.Lagowski, J. Vac. Sci. Technol, Vol. **10**, Nr. 1, 130 (1973).

[61] L. Kronik, Y. Shapira, *Surface photovoltage phenomena: theory, experiment and applications* (Elsevier Science, Amsterdam, 1999).

[62] S. Datta, S. Ghosh, B. M. Arora, Rev. of Sci. Instr. **72**, 177 (2001).

[63] see for example S. M. Sze, *Physics of Semiconductor Devices,* (Second Edition), (Wiley, New York, 1981), p. 276.

[64] S. M. Sze, *Physics of Semiconductor Devices,* (Second Edition), (Wiley, New York, 1981), p. 255.

[65] A. Ksendzov, W. T. Pike, A. Larsson, Phys. Rev. B **47**, 2228 (1993).

[66] A. M. Fox, D. A. B. Miller, G. Livescu, J. E. Cunningham, W. Y. Jan, IEEE J. Quantum Electron. **27**, 2281 (1991).

[67] S. C. Dahlberg, J. R. Chelikowsky, W. A. Orr, Phys. Rev. B **15**, 3163 (1977).

[68] S. Datta, B. M. Arora and S. Kumar, Phys. Rev. B **62**, 13604 (2000).

---

[69] See for example, G. Bastard, *Wave mechanics applied to semiconductor heterostructures* (Ed. de Physique, Les Ulis Cedex, 1992).

[70] J. A. Brum and G. Bastard, Phys. Rev. B **33**, 1420 (1986).

[71] M. Dinu, J. E. Cunningham, F. Quochi, J. Shah, *Conference on Lasers and Electro-Optics (CLEO) 2001*, p. 35.

[72] T. Baier, U. Mantz, K. Thonke, R. Sauer, F. Schäffler, and H.–J. Herzog, Phys. Rev. B **50**, 15191 (1994).

[73] Y. S. Chiu, M. H. Ya, W. S. Su, and Y. F. Chen, J. Appl. Phys. **92**, 5810 (2002).

[74] I. Vurgaftman, J. R. Meyer, and L. R. Ram-Mohan, J. Appl. Phys. **89**, 5815 (2001).

[75] J. D. Holm and K. S. Champlin, J. Appl. Phys. **39**, 275 (1968).

[76] W. H. Hartwig and J. J. Hinds, J. Appl. Phys. **40**, 2020 (1969).

[77] M. Kunst and G. Beck, J. Appl. Phys. **60**, 3558 (1986).

[78] S. Y. Grabtchak and M. Cocivera, Phys. Rev. B **50**, 18219 (1994).

[79] U. Fano, Phys. Rev. **124**, 1866 (1961).

[80] V. V. Mitin, V. V. Kochelap, and M. A. Stroscio, *Quantum Heterostructures for Microelectronics and Optoelectronics* (Cambridge University Press, Cambridge, 1999), Chapter 10.

List of Abbreviations

ATR	– Attenuated Total Reflection
CR	– Cyclotron Resonance
CW	– Continuous Wave
FWHM	– Full Width at Half Maximum
IR	– InfraRed
ITO	– Indium Tin Oxide
MBE	– Molecular Beam Epitaxy
PC	– PhotoCurrent
PDS	– Photothermal Deflection Spectroscopy
PL	– PhotoLuminescence
PV	– PhotoVoltage
QD	– Quantum Dot
QW	– Quantum Well
QWs	– Quantum Wells
RF	– Radio Frequency
RTA	– Rapid Thermal Annealing
SI	– Semi-Insulating
SLPL	– Strongly Localized PhotoLuminescence
SPV	– Surface PhotoVoltage
TE	– Transversal Electric
TEM	– Transmission Electron Microscopy
UHV	– Ultra-High Vacuum
VCSEL	– Vertical-Cavity Surface-Emitting Laser
VCSELs	– Vertical-Cavity Surface-Emitting Lasers

Acknowledgments

Here, I would like to thank to all those who have contributed to the successful completion of this work.

First of all, I would like to thank to ***Prof. Ph.D. F. Koch*** for the offered opportunity of taking my Ph.D. degree in the Physics Department of München Technical University and to ***Dr. H. Riechert*** who has offered me the key chance to work in his group in *Infineon Technologies AG* and to complete this work.

I would like here also to thank to ***Dr. V. Petrova-Koch*** and ***Dr. H. Porteanu*** for the given chance to come at the München Technical University, for the support given at the beginning of my work, while trying to integrate myself in a new country and work atmosphere, and for the trust they have granted to me.

My special thanks to ***Dr. H. Porteanu***, ***Prof. Ph.D. F. Koch***, and ***Dr. H. Riechert*** for their support all through my work and for many useful discussions

I would like also to convey special thanks to the people who have provided me with good sample and who made my work possible: *Dr. L. Geelhaar*, *Dr. A. Yu. Egorov*, and *Dr. I. Ecker*.

Then I would like to thank to the many collaborators who have contributed, directly and indirectly, to my work:

- to *Dr. U. Beierlein* from the group of *Prof. Dr. J. P. Kotthaus* in Ludwig-Maximilians-University of Munich;
- to *S. Birner* and *M. Sabathil* from the group of *Prof. Ph.D. P. Vogl* in Schottky Institute of Munich Technical University;
- to *Dr. P. J. Klar*, *K. Hantke*, *J. Hübner* from the group of *Prof. Dr. W.W. Rühle* in Philipps University of Marburg;
- to *Dr. Martin Albrecht* and *Thilo Remmele* from the group of *Prof. Dr. Horst. P. Strunk* in Friedrich-Alexander University of Erlangen-Nuremberg.

Their support in making measurements and calculations contributed essentially to the success of my work.

My experimental work would not have been possible without the support of the technicians of E16: *H. Märcz*, *J. Seitz*, *H. Streit*, *R. Filbry*. They have offered me essential support in building experimental setups.

All through my work I received constant support from the secretary of E16: *Laura Darabas*. I would like to give her here my special thanks.

My friendly thanks to the coleagues in E16 who have contributed to my work: *Habil. Dr. D. Kovalev* for useful discussion and to *Dr. Th. Dittrich, Dr. J. Diener* and *O. Loginenko* for the good collaboration during the work.

Also my special thanks to the colleagues in Infineon: *Dr. R. Averbeck*, *G. Jaschke*, *Dr. Ch. Hanke*, *Dr. B. Stegmüller*, *H. Heddrich*, *Dr. R. März*, *Dr. A. Ramakrishnan*. They have contributed in many ways to the success of my work.

I am grateful to my parents and my friends, who have supported me in difficult moments, and from whom I had to stay far apart during my work.

This work was supported by E16 in the frame of a DFG (Deutsche Forschungsgemeinschaft) project and *Infineon Technologies AG*.

Curriculum Vitae

19.08.1971	born in Cluj-Napoca, Romania
1977-1981	Ground School, Gârdani, Romania
1981-1985	Secondary Scool, Gârdani, Romania
1985-1989	Industrial Electrotechnical and Telecommunication Lyceum, Baia Mare, Romania
1989-1990	Military Service
1990-1995	student at Electronic and Telecommunication Faculty, Technical University of Timişoara, Romania
1995-1996	Master Degree in “Digital Signal Processing for use in Telecommunications” obtained at the Electronic and Telecommunication Faculty, Technical University of Timişoara, Romania
1996-1999	Teaching Assistant at Electronic and Telecommunication Faculty, Technical University of Timişoara, Romania
1999-2003	Ph.D. student, Semiconductor Physics, Department of Physics E16, München Technical University and Infineon Technologies AG München, Germany

List of publications

(6) **Gh. Dumitras** and H. Riechert,
"Determination of band offsets in semiconductor quantum well structures using surface photovoltage",
Journal of Applied Physics **94**, 3955 (2003).

(5) P. J. Klar, H. Gruning, L. Chen, T. Hartmann, D. Golde, M. Gungerich, W. Heimbrodt, J. Koch, K. Volz, B. Kunert, T. Torunski, W. Stolz, A. Polimeni, M. Capizzi, **Gh. Dumitras**, L. Geelhaar, H. Riechert,
"Unusual properties of metastable (Ga, In)(N,As) containing semiconductor structures",
IEE Proceedings-Optoelectronics, **150**, 28 (2003).

(4) M. Albrecht, V. Grillo, T. Remmele, H. P. Strunk, A. Yu. Egorov, **Gh. Dumitras**, H. Riechert, A. Kaschner, R. Heitz, A. Hoffmann,
"Effect of annealing on the In and N distribution in InGaAsN quantum wells",
Applied Physics Letters **81**, 2719 (2002).

(3) **Gh. Dumitras**, H. Riechert, H. Porteanu, F. Koch,
"Surface photovoltage studies of $In_xGa_{1-x}As$ *and* $In_xGa_{1-x}As_{1-y}N_y$ *quantum well structures",*
Physical Review B **66**, 205324 (2002).

(2) A. Yu. Egorov, D. Bedarev, D. Bernklau, **Gh. Dumitras**, H. Riechert,
"Self-assembled InAs quantum dots in an InGaAsN matrix on GaAs",
Physica Status Solidi B, **224**, 839 (2001).

(1) A. Yu. Egorov, D. Bernklau, B. Borchert, S. Illek, D. Livshits, A. Rucki, M. Schuster, A. Kaschner, A. Hoffmann, **Gh. Dumitras**, M. C. Amann, H. Riechert,
"Growth of high quality InGaAsN heterostructures and their laser application",
Journal of Crystal Growth, **227-228**, 545 (2001).

Conference participation

(2) Poster presentation, European Molecular Beam Epitaxy Conference, Hinterzarten, February, 2001.

(1) Poster presentation, European Material Research Symposium, Strasbourg, June, 2002.